



저작자표시-비영리-변경금지 2.0 대한민국

이용자는 아래의 조건을 따르는 경우에 한하여 자유롭게

- 이 저작물을 복제, 배포, 전송, 전시, 공연 및 방송할 수 있습니다.

다음과 같은 조건을 따라야 합니다:



저작자표시. 귀하는 원저작자를 표시하여야 합니다.



비영리. 귀하는 이 저작물을 영리 목적으로 이용할 수 없습니다.



변경금지. 귀하는 이 저작물을 개작, 변형 또는 가공할 수 없습니다.

- 귀하는, 이 저작물의 재이용이나 배포의 경우, 이 저작물에 적용된 이용허락조건을 명확하게 나타내어야 합니다.
- 저작권자로부터 별도의 허가를 받으면 이러한 조건들은 적용되지 않습니다.

저작권법에 따른 이용자의 권리는 위의 내용에 의하여 영향을 받지 않습니다.

이것은 [이용허락규약\(Legal Code\)](#)을 이해하기 쉽게 요약한 것입니다.

[Disclaimer](#)

Doctoral Thesis

Multifunctional heteronanomat-mediated electrodes  
for high-performance/flexible lithium-ion batteries

Ju-Myung Kim

Department of Energy Engineering

Graduate School of UNIST

2019

Multifunctional heteronanomaterial-mediated  
electrodes for high-performance/flexible lithium-  
ion batteries

Ju-Myung Kim

Department of Energy Engineering

Graduate School of UNIST

Multifunctional heteronanomat-mediated  
electrodes for high-performance/flexible  
lithium-ion batteries

A thesis/dissertation  
submitted to the Graduate School of UNIST  
in partial fulfillment of the  
requirements for the degree of  
Doctor of Philosophy

Ju-Myung Kim

12. 6. 2018 of submission

Approved by



Advisor

Sang-Young Lee

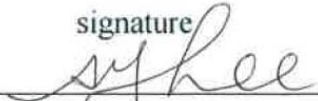
Multifunctional heteronanomaterial-mediated  
electrodes for high-performance/flexible  
lithium-ion batteries

Ju-Myung Kim

This certifies that the thesis/dissertation of Ju-Myung Kim is  
approved.

12. 6. 2018 of submission

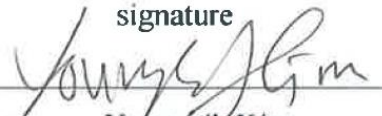
signature



---

Advisor: Sang-Young Lee

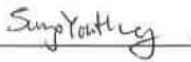
signature



---

Youngsik Kim

signature



---

Sung You Hong

signature



---

Sujin Park

signature



---

Sung Joong Kang

## Contents

<b>Abstract</b> .....	vii
<b>List of figures</b> .....	viii
<b>List of tables</b> .....	xvi
<b>Chapter 1. Introduction</b> .....	1
1.1 Overview of rechargeable power sources .....	1
1.2 Principle of lithium-ion batteries .....	2
1.3 Lithium-ion battery materials (LIBs) .....	3
1.3.1 Cathodes active materials .....	3
1.3.2 Anode active materials .....	4
1.3.3 Separators .....	5
1.3.4 Electrolytes .....	5
1.3.5 Electrode components .....	7
1.4 Research objective .....	8
1.4.1 Limitations of the conventional electrode architecture .....	9
1.4.2 Research progress in electrode architecture for LIBs .....	9
1.4.3 Strategies .....	12
1.5 References .....	12
<b>Chapter 2. Electrosprayed CNT/electrospun polymer heteronanomat-mediated LIB electrodes</b> .....	14
2.1 One-dimensional building elements-intermingled heteronanomats as a platform architecture for superior performance ultrahigh-capacity lithium-ion battery cathodes.....	14
2.1.1 Introduction .....	14
2.1.2 Experimental section .....	16
2.1.2.1 Alchitectural design and fabrication of HM cathode .....	16
2.1.2.2 Structural/physicochemical characterization of HM cathodes .....	17
2.1.2.3 Electrochemical performance of HM cathodes .....	17
2.1.3 Result and discussion .....	17
2.1.3.1 Structural and physicochemical proeprties of HM OLO cathode .....	17
2.1.3.2 Electrochemical properties of HM OLO cathodes .....	23

2.1.3.3 Ultrathick HM OLO cathodes for high capacity -----	27
2.1.3.4 Physicochemical and electrochemical properties of HM LNMO cathodes --	29
2.1.4 Conclusion -----	33
2.1.5 References -----	34
2.2 All-nanomat lithium-ion batteries: A new cell architecture platform for ultrahigh energy density and mechanical flexibility -----	37
2.2.1 Introduction -----	37
2.2.2 Experimental section -----	39
2.2.2.1 Design and fabrication of nanomat Si anodes -----	39
2.2.2.2 Fabrication of nanomat OLO cathodes incorporating rambutan-shaped OLO/MWCNT nanocomposite powders -----	39
2.2.2.3 Fabrication of nanomat $A_2O_3$ separator -----	40
2.2.2.4 Structural/physicochemical characterization of the nanomat electrodes -----	40
2.2.2.5 Electrochemical characterization of nanomat electrodes and all-nanomat full cells -----	41
2.2.3 Result and discussion -----	41
2.2.3.1 Structural uniqueness and electrochemical superiority of nanomat Si anodes	41
2.2.3.2 Nanomat OLO cathodes based on rambutan-shaped OLO/MWCNT nanocomposite powders -----	50
2.2.3.3 All-nanomat (Si anode/ $Al_2O_3$ separator/OLO cathode) full cells for ultrahigh energy density and mechanical flexibility -----	57
2.2.4 Conclusion -----	61
2.2.5 Reference -----	62
2.3 Carbon nanotube-cored cobalt porphyrin as a one-dimensional nanohybrid strategy for high-performance lithium-ion battery anodes -----	65
2.3.1 Introduction -----	65
2.3.2 Experimental section -----	66
2.3.2.1 Synthesis of CoTCPP -----	66
2.3.2.2 Dispersion of the MWCNTs in aqueous solutions with various dispersing agents-----	66
2.3.2.3 Preparation of the CC-nanohybrids -----	67
2.3.2.4 Fabrication of the slurry-cast and nanomat CC-nanohybrid anode sheets -----	67
2.3.2.5 Physicochemical and structural characterization -----	67

2.3.2.6 Electrochemical characterization .....	68
2.3.2.7 Theoretical model systems .....	69
2.3.3 Result and discussion .....	71
2.3.3.1 Preparation and structural characterization of the CC-nanohybrids .....	71
2.3.3.2 Electrochemical superiority of the CC-nanohybrids over pristine CoTCPP .....	76
2.3.3.3 Preparation and characterization of all-fibrous nanomat anode sheets based on CC-nanohybrids .....	79
2.3.4 Conclusion .....	84
2.3.5 Reference .....	85
<b>List of publications .....</b>	<b>88</b>

## Abstract

With the rapid growth of the demands for portable electronics, electric vehicles (EVs) with high-energy density and mechanical flexibility, the importance of rechargeable power sources is on the steady rise. Among a variety of rechargeable systems, lithium-ion batteries (LIBs) are the most suitable energy storage system. It is well known that the higher energy density of LIBs comes from the higher storage capacity value of electrode active materials and electrode architecture.

Unfortunately, almost all the conventional electrode architecture suffers several drawbacks. First, the random stacking of electrode components such as active materials, conductive additives, and polymeric binders causes irregular electron/ion transport pathway through-thickness direction. Second, the incomplete electron/ion transport pathway increases unnecessary electrochemical polarization. Third, the non-faradaic materials such as metallic current collector, conductive additives and polymeric binders account for a great part of the total mass of electrode, resulting in lower areal capacity and energy densities of the LIBs.

To overcome these unavoidable challenges, a new strategy to gain uniform ion/electron pathway is needed. In this dissertation, we propose a new class of three-dimensional (3D) heteronanomat electrodes (HM electrode) based on multifunctional polymer fibrils and carbon nanotube (CNT). Through this architectural design, we enable unprecedented improvements in the electrochemical performance and mechanical flexibility, which lie far beyond those achievable with conventional LIBs electrode technologies. To realize the aforementioned goal, our primary interest is focused on the design/synthesis of multifunctional polymer fibrils and also HM electrode architecture, along with a proper selection of target electrode active materials. In addition, much attention should be also devoted to manufacturing processes and optimization fabrication conditions for the HM electrodes. To explore the potential applicability of the HM electrodes for LIBs, structural/electrochemical characterizations are comprehensively conducted, with a particular focus on 3D-reticulated, bicontinuous ion/electron conduction pathways.

## List of figures

### Chapter 1

**Figure 1.1** Ragone plot of various rechargeable power sources. (D. U. Sauer et al. Proc IMechE Part D: J Automobile Engineering, 2013, 227, 761)

**Figure 1.2** Schematic of a discharge process of lithium-ion battery. (J.-M. Tarascon Science, 2011, 35, 928)

**Figure 1.3** Various structures of cathode materials. (P. M. Ajayan et al. Nature energy, 2017, 2, 17108)

**Figure 1.4** Several anode materials for lithium-ion battery. (C. Capiglia et al. Journal of Power sources, 2014, 257, 421)

**Figure 1.5** Diagram illustrating the capacities and electrochemical potentials of important cathode and anode materials. (Y. Lei et al., Advanced Energy Materials, 2016, 6, 1502514)

**Figure 1.6** Schematic illustration of the drawbacks of the conventional electrode architecture.

**Figure 1.7** Previous studies about electrode architectures for LiBs classified as fabrication methods; (a) coating or impregnation, (b) Hydrogel and aerogel, (c) vacuum filtration, (d) electrospinning.

### Chapter 2

**Figure 2.1** OLO and LNMO cathode materials respectively represent high-capacity and high-voltage cathode materials. (S. Passerini et al. Adv. Energy Mater. 2016, 6, 1600906)

**Figure 2.2** A SEM image of pristine (microsized) OLO powders, wherein an inset is a photograph showing the precipitation of OLO-dispersed solution.

**Figure 2.3** (a) SEM images of OLO nanopowders, wherein an inset is a photograph showing that the good dispersion state of OLO nanopowders in the solution after being stored at 5 h, (b) HR TEM images of OLO nanoparticles.

**Figure 2.4** Comparison in pristine (= microsized) and nanosized OLO powders: (a) XRD patterns, (b) charge/discharge profiles (current density = 0.1 C/0.1 C).

**Figure 2.5** Schematic illustration depicting the manufacturing procedure of HM cathodes through simultaneous electrospaying/electrospinning process. Structural/physicochemical characterization of HM cathodes.

**Figure 2.6** TGA profiles used for estimating composition ratio of HM OLO cathode.

**Figure 2.7** SEM image (surface view) of (a) HM OLO cathode and cross-sectional SEM images (focusing on cathode thickness) of: (b) HM OLO cathode and (c) control OLO one.

**Figure 2.8** Raman spectra of HM OLO cathode and OLO nanopowders.

**Figure 2.9** (a) Electronic conductivity of HM OLO cathode and control OLO one, (b) electrolyte wettability (determined by electrolyte-immersion height) of HM OLO cathode and control OLO one.

**Figure 2.10** (a) Mechanical flexibility and dimensional integrity of HM OLO cathode, (b) change in electronic resistance as a function of longitudinal compression cycle (bending radius = 20 mm, deformation rate = 200 mm min<sup>-1</sup>), wherein an inset is a photograph showing the mechanical rupture of control OLO cathode after 95 bending cycles, (c) SEM image (surface view) of HM OLO cathode after the bending cycle test.

**Figure 2.11** (a) Comparison in discharge capacity (normalized by OLO mass) between HM OLO cathode and control OLO one at current density of 0.1 C/0.1 C under voltage range of 2.0 - 4.7 V, (b) charge/discharge profile of a model electrode (MWCNTs/PAN nanofibers without OLO powders).

**Figure 2.12** (a) Comparison in total areal weight (mg cm<sub>cathode</sub><sup>-2</sup>) between HM OLO cathode and control OLO one, (b) charge/discharge profiles of HM OLO cathode and control OLO one, (c) GITT profiles of cells assembled with HM OLO cathode or control OLO one and variation in internal cell resistance as a function of state of charge and depth of discharge.

**Figure 2.13** (a) Schematic representation depicting a pouch cell designed for *in-situ* EIS measurement of thickness-directional overpotential distribution (i.e., voltage difference between top and bottom side) of cathodes. Overpotential distribution of the cathodes in the through-thickness direction (i.e., voltage difference between the top and bottom side of cathodes) at current density of 1.0 C/1.0 C and 5.0C/5.0C, wherein inset images illustrate electronic/ionic transport phenomena of the cathodes: (b) HM OLO cathode; (c) control OLO cathode at 1.0C/1.0C, (d) HM OLO cathode; (e) control OLO cathode at 5.0C/5.0C.

**Figure 2.14** (a) Comparison in cycling performance (at charge/discharge current density of 5.0 C/5.0 C under voltage range of 2.0 - 4.7 V) between HM OLO cathode and control OLO one, (b) charge/discharge profiles with cycling (up to 200 cycles) of half cells assembled with HM OLO cathode or control OLO one, (c) TOF-SIMS images of LiF byproduct on cathode surface after 200 cycles, (d) SEM image of HM OLO cathode after 200 cycles.

**Figure 2.15** (a) Conceptual illustration depicting facile fabrication of user-tailored, multi-stacked HM OLO cathodes in series, (b) SEM images (cross-sectional view) of multi-stacked HM OLO cathodes with various thickness (70 μm (= 1 sheet), 230 μm (= 4 sheets), 450 μm (= 8 sheets)).

**Figure 2.16** The poor structural stability of control OLO cathode (thickness ~ 400 μm).

**Figure 2.17** (a) Charge/discharge capacities per cathode area (mAh cm<sub>cathode</sub><sup>-2</sup>) of multi-stacked HM OLO cathodes, (b) cycling performance (expressed as mAh cm<sub>cathode</sub><sup>-2</sup>) of multi-stacked HM OLO cathodes as a function of cathode thickness. Charge/discharge profiles with cycling of multi-stacked HM OLO cathodes as a function of cathode thickness : (c) after 1 cycle; (d) after 30 cycles (inset : SEM image (surface view) of 8 sheets-stacked HM OLO cathode after the cycling test).

**Figure 2.18** (a) SEM image of pristine (= microsized) LNMO particles, (b) SEM image of nanosized LNMO particles, (c) comparison in XRD patterns between pristine (= microsized) LNMO particles and

nanosized LNMO ones.

**Figure 2.19** (a) SEM image (cross-sectional view) of HM LNMO cathode, (b) TGA profiles used for estimating composition ratio of HM LNMO cathode.

**Figure 2.20** Mechanical flexibility and dimensional integrity of HM LNMO cathode.

**Figure 2.21** Electronic conductivities of HM LNMO cathode and control LNMO one.

**Figure 2.22** Discharge rate capability over a wide range of discharge current densities (= 0.2 - 5.0 C) at a fixed charge current density of 0.2 C.

**Figure 2.23** (a) Charge/discharge profiles of cells assembled with HM LNMO cathode or control LNMO one, (b) charge/discharge capacities per cathode area ( $\text{mAh cm}_{\text{cathode}}^{-2}$ ) of multi-stacked HM LNMO cathodes, (c) cycling performance (expressed as  $\text{mAh cm}_{\text{cathode}}^{-2}$ ) of multi-stacked HM LNMO cathodes.

**Figure 2.24** Change in electrochemical stability window of PAN nanofibers after thermal treatment ( $120\text{ }^{\circ}\text{C}/12\text{ h} \rightarrow 150\text{ }^{\circ}\text{C}/2\text{ h}$  in a vacuum oven).

**Figure 2.25** The roadmap for Li battery technology. (D. Aurbach et al. Materials Today, 2014, 17, 110)

**Figure 2.26** Schematic representation depicting the stepwise preparation process (bottom layer  $\rightarrow$  Si active (middle) layer  $\rightarrow$  top layer) for the nanomat Si anode, along with a photograph. Each layer of the nanomat Si anode was fabricated by concurrent electrospinning and electrospaying through two different nozzles.

**Figure 2.27** (a) Cross-sectional SEM image of nanomat Si anode (Si active layer ( $\sim 10\text{ }\mu\text{m}$ ) sandwiched between thin ( $\sim 1\text{ }\mu\text{m}$ ) electroconductive top/bottom layers), (b) SEM image of Si active layer, where the Si nanoparticles were compactly embedded in close contact with the PAN nanofiber/SWCNT-interweaved heteromat, (c) SEM image of SWCNT/PAN-interweaved top and bottom layers, (d) Cross-sectional SEM image of conventional Si anode with a similar Si mass loading. The conventional Si anode consisted of an electrochemically active layer (Si nanoparticles/PAA-CMC binder/carbon black = 70/20/10 (w/w/w), thickness  $\sim 8\text{ }\mu\text{m}$ ) on top of a Cu current collector ( $\sim 20\text{ }\mu\text{m}$ ).

**Figure 2.28** TGA profiles used to estimate the composition ratio of the nanomat Si anode. The composition ratios of the Si active (middle) layer and top/bottom layers were estimated to be (Si nanoparticles/SWCNT)/PAN = (60/6)/34 (w/w/w) and SWCNT/PAN = 40/60 (w/w), respectively. The slight increase in the weight of the Si nanoparticles, Si active (middle) layer, and nanomat Si anode above  $700\text{ }^{\circ}\text{C}$  was ascribed to the formation of new silicon oxides.

**Figure 2.29** Photograph showing the poor dispersion state of (Si nanoparticle/SWCNT) suspension solution without a PEDOT:PSS additive.

**Figure 2.30** (a) Comparison of the (in-plane) electronic conductivities of the nanomat Si anode and conventional Si anode, (b) comparison of the electrolyte (1.3 M  $\text{LiPF}_6$  in EC/DEC = 3/7 (v/v) with 10 wt% FEC) wettability between the nanomat Si anode and conventional Si anode.

**Figure 2.31** (a) Change in the electronic resistance of nanomat Si and conventional Si anodes as a function of longitudinal compression cycle (bending radius = 5 mm, deformation rate = 20 mm min<sup>-1</sup>). The inset shows a photograph of the deformed nanomat Si anode. SEM images of (b) nanomat Si anode and (c) conventional Si anode after the bending cycle test (300 cycles).

**Figure 2.32** Initial charge (lithiation)/discharge (delithiation) profiles at charge/discharge current densities of 0.05 C/0.05 C, expressed as capacity per Si mass (= mAh g<sub>Si</sub><sup>-1</sup>). The coin half cell (Si anode/PE separator/Li metal) was used. (a) Nanomat Si anode vs. conventional Si anode, (b) blank electrode (SWCNT/PAN = 40 / 60 (w/w), without Si nanoparticles), (c) Si active (middle) layer.

**Figure 2.33** (a) Initial charge (lithiation)/discharge (delithiation) profiles of Si anodes at charge/discharge current densities of 0.05 C/0.05 C, expressed as capacity per mass of Si anode sheet (= mAh g<sub>anode</sub><sup>-1</sup>), (b) comparison of the areal masses (= mg cm<sub>Anode</sub><sup>-2</sup>) between the nanomat Si anode and conventional Si anode.

**Figure 2.34** (a) Delithiation rate capability (expressed as mAh g<sub>anode</sub><sup>-1</sup>) of half cells (= Si anode/PE separator/Li metal). The discharge current density was varied from 0.2 to 3.0 C at a constant charge current density of 0.2 C, (b) GITT profiles of half cells upon repeated current stimuli (at a current density of 0.2 C and an interruption time between each pulse of 60 min) and variation in the internal cell resistance as a function of SOC and DOD.

**Figure 2.35** (a) Overpotential distribution of Si anodes in the through-thickness direction as a function of SOC. The voltage gap (DV (= V<sub>top</sub> – V<sub>bottom</sub>, at 50% SOC) was measured at a discharge current density of 0.2 C. (b) schematic representation of a pouch cell designed for the in situ EIS measurement of the overpotential distribution of Si anodes in the through-thickness direction (i.e., voltage difference between the top and bottom sides).

**Figure 2.36** Cycling performance (expressed as mAh g<sub>Anode</sub><sup>-1</sup>) of half cells: nanomat Si anode vs. conventional Si anode. The half cells were cycled at charge/discharge current densities of 0.2 C/0.2 C under a voltage range of 0.01-1.2 V.

**Figure 2.37** SEM image after the cycle test (100 cycles). (a) and (b) nanomat Si anode. (c) and (d) conventional Si anode. The thickness change ( $\Delta t$  = thickness (after 100 cycles) – thickness (before cycling)) of the Si anodes was recorded.

**Figure 2.38** SEM image of rambutan-shaped OLO/MWCNT nanocomposite (referred to as “R-OM”) powders. The inset is a photograph of rambutan fruit.

**Figure 2.39** (a) SEM image of bare OLO powders (average diameter = 5 mm). (b) SEM image showing the poor mixing state of OLO nanoparticle aggregates and MWCNTs. (c) viscosity of the OLO/MWCNT suspension (with PVP vs. without PVP). (d) viscoelastic properties (G' and G'').

**Figure 2.40** (a) N<sub>2</sub> adsorption-desorption of R-OM powders. The inset shows the HR-TEM image. (b) BJH plot showing the average pore size of the R-OM powders.

**Figure 2.41** SEM images of R-OM powders with different MWCNT contents: (a) 0, (b) 3, (c) 5, (d) 15 wt%.

**Figure 2.42** (a) (In-plane) Electronic conductivities and (b) discharge rate capabilities (coin half cell (OLO cathode/PE separator/lithium metal anode, the discharge current density was varied from 0.2 to 5.0 C at a fixed charge current density of 0.2 C) of the OLO cathodes (R-OM powder/PVdF binder/carbon black additive = 80/10/10 (w/w/w), where the MWCNT contents in the R-OM powders were 0, 3, 5, 10 and 15 wt%.

**Figure 2.43** Amount of  $Mn^{2+}$  ions captured by PAN and PAN/PVP (= 50/50 (w/w)) films (measured by ICP-MS analysis).

**Figure 2.44** Conceptual representation depicting the structural uniqueness of the nanomat OLO cathode. Its photograph was inserted.

**Figure 2.45** TGA profiles used to estimate composition ratio of the nanomat OLO cathode; the weight-based ratio of OLO/MWCNT/(PAN-PVP) was 65/13/22 (w/w/w).

**Figure 2.46** Cross-sectional SEM image of OLO cathodes: (a) nanomat OLO cathode. R-OM powders were densely packed in the MWCNT/(PAN/PVP)-interweaved heteromat without an Al foil current collector. The inset shows a high-magnification view, (b) conventional OLO cathode (OLO/PVdF/carbon black = 80/10/10 on an Al foil), (c) comparison of the electronic conductivities between the nanomat OLO cathode and conventional OLO cathode (OLO/PVdF/carbon black = 80/10/10 on an Al foil, fabricated by a slurry casting method). (d) electrolyte (1 M  $LiPF_6$  in EC/DMC = 1/1 (v/v)) wettability.

**Figure 2.47** Change in the electronic resistances of the nanomat OLO and conventional OLO cathodes as a function of longitudinal compression cycle (bending radius of 5 mm, deformation rate of 200 mm  $min^{-1}$ ). The inset shows a photograph of the deformed nanomat OLO cathode.

**Figure 2.48** (a) Comparison of the areal masses (=  $mg\ cm_{Cathode}^{-2}$ ) between the nanomat OLO cathode and conventional OLO cathode, (b) discharge rate capability (expressed as  $mAh\ g_{Cathode}^{-1}$ ) of half cells (OLO cathode/PE separator/Li metal): nanomat OLO cathode vs. conventional OLO cathode. The discharge current density was varied from 0.2 to 5.0 C at a fixed charge current density of 0.2 C, (c) cycling performance (expressed as  $mAh\ g_{Cathode}^{-1}$ ) of nanomat OLO cathode (vs. conventional OLO cathode) at charge/discharge current densities of 1.0 C/1.0 C under a voltage range of 2.0-4.7 V, (d) amount of metallic Mn deposited on lithium metal anodes after the cycling test (estimated from ICP-MS analysis).

**Figure 2.49** Structure and basic membrane properties of nanomat  $Al_2O_3$  separator. (a) SEM image and photograph (inset), (b) thermal shrinkage after exposure to 150°C for 0.5 h (nanomat  $Al_2O_3$  separator vs. PE separator), (c) discharge rate capability of cells (nanomat  $Al_2O_3$  separator vs. PE separator), (d) cyclability of cells (nanomat  $Al_2O_3$  separator vs. PE separator). The cells consisted of a  $LiCoO_2$  cathode

(LiCoO<sub>2</sub>/carbon black/PVdF = 95/2.5/2.5 (w/w/w)) and graphite anode (graphite/carbon black/SBR/CMC = 96/1/2/1 (w/w/w)).

**Figure 2.50** (a) Cross-sectional SEM image of all-nanomat full cell (Si anode/Al<sub>2</sub>O<sub>3</sub> separator/OLO cathode), (b) conceptual representation of all-nanomat full cells based on 1D building elements-interweaved heteronanomat skeletons.

**Figure 2.51** (a) Initial charge/discharge profiles (at charge/discharge current densities of 0.05 C/0.05 C under a voltage range of 2.0-4.6 V) of full cells (all-nanomat vs. conventional), expressed as capacity (mAh g<sub>Cell</sub><sup>-1</sup>) per cell weight (= anode + cathode + separator), (b) comparison of the areal masses (= mg cm<sub>Cell</sub><sup>-2</sup>) of the cell components (*i.e.*, anode, cathode and separator) between the all-nanomat full cell and conventional full cell, (c) discharge rate capability (expressed as mAh g<sub>Cell</sub><sup>-1</sup>) of full cells (all-nanomat vs. conventional). The discharge current density was varied from 0.1 to 1.0 C at a fixed charge current density of 0.1 C, (d) cycling performance (expressed as mAh g<sub>Cell</sub><sup>-1</sup>) of full cells (all-nanomat vs. conventional) at a charge/discharge current density of 0.5 C/0.5 C.

**Figure 2.52** SEM and EDS images (green dots represent metallic Mn deposited on the Si anode surface) showing the structural change of the Si anodes after 100 cycles. (a) and (c) all-nanomat full cell. (b) and (d) conventional full cell.

**Figure 2.53** Amount of metallic Mn (estimated from ICP-MS analysis) deposited on Si anodes: all-nanomat full cell vs. conventional full cell.

**Figure 2.54** (a) Charge/discharge profiles (expressed as mAh g<sub>Cell</sub><sup>-1</sup>) of all-nanomat full cell before/after 100 bending cycles (bending diameter = 5 mm). The inset shows a photograph of the deformed all-nanomat full cell, (b) photographs of all-nanomat full cells showing the operation of LED lamps: after being folded 3 times (left) and after being seriously crumpled (right).

**Figure 2.55** Global minimum (left) and local minimum (right) structures of CoTCPP. The energy difference ( $\Delta E = E_X - E_{\text{local minimum}}$ , X = global minimum or local minimum) was calculated to be -7.98 eV.

**Figure 2.56** DFT-optimized staggered and eclipsed configurations of CoTCPP, along with the calculated stacking energies ( $\Delta E_{\text{stack}}$ ). The CoTCPP molecules at the bottom are green-colored.

**Figure 2.57** Schematic representation depicting the stepwise preparation of the CC-nanohybrids along with photographs of the products obtained at each step.

**Figure 2.58** (a) UV-vis-NIR absorption and (b) FT-IR spectra of CoTCPP.

**Figure 2.59** AFM image of CoTCPP/MWCNT suspension casted on a mica substrate.

**Figure 2.60** (a) UV-vis-NIR absorption spectra of CoTCPP in aqueous NaOH solution (red line) and supernatant solutions (prepared from CoTCPP/MWCNT (blue line) and SDS/MWCNT suspensions (black line)). The photographs of the corresponding solutions are also displayed, (b) fluorescence spectra of CoTCPP in aqueous NaOH solution (red line) and supernatant solution from

CoTCPP/MWCNT suspension (blue line), (c) photographs of aqueous MWCNT suspensions prepared with various dispersing agents.

**Figure 2.61** (a) DFT-optimized structures of c-ZZNR-16, c-ZZNR-20, and c-ZZNR-30, (b) stacking energies ( $\Delta E_{\text{stack}}$ ) calculated for the staggered/eclipsed configurations of CoTCPP (red columns) and the stacking configurations between CoTCPP and c-ZZNR systems (blue columns), (c) PDOS of CoTCPP (top: isolated, middle: stacked on c-ZZNR-30) and c-ZZNR-30 stacked with CoTCPP (bottom).  $E_F$  is the Fermi energy.

**Figure 2.62** (a) SEM image (inset: pristine MWCNTs) and (b) TEM image of CC-nanohybrids. The arrow indicates the CoTCPP shell layer. Raman spectra of CoTCPP (red line), CC-nanohybrids (blue line), and MWCNTs (black line).

**Figure 2.63** Photograph of slurry-cast anode containing MWCNT additives (weight-based composition ratio: CoTCPP/MWCNT/carbon black/CMC = 30/20/37.5/12.5). The resulting anode showed the structural disruption due to the poor dispersion state of the MWCNTs.

**Figure 2.64** (a) Lithiation/delithiation profiles, in which delithiation current densities varied from 0.1 to 20 C under a constant lithiation current density of 0.1 C, (b) comparison of delithiation rate capability. EIS spectra of (c) CC-nanohybrid and (d) pristine CoTCPP after the initial lithiation. Inset shows the associated equivalent circuit model.<sup>[ref]</sup>  $R_E$ : electrolyte resistance,  $R_{\text{SEI}}$ : solid electrolyte interphase (SEI) resistance,  $R_{\text{CT}}$ : charge transfer resistance,  $C_{\text{SEI}}$ : SEI capacitance,  $C_{\text{dl}}$ : double layer capacitance, and  $Z_W$ : Warburg impedance.

**Figure 2.65** SEM image of CoTCPP powders

**Figure 2.66** Cycle performance at lithiation/delithiation current densities of 0.1 C/5.0 C.

**Figure 2.67** Schematic representation depicting the preparation of the all-fibrous nanomat anode sheet along with its photographs.

**Figure 2.68** (a) SEM image (inset: high-magnification) of the nanomat anode sheet. (b) electronic conductivity. (c) photographs showing electrolyte wettability. (d) change in the electronic resistance of the nanomat (red dots) and slurry-cast (black dots) anode sheets as a function of the longitudinal compression cycle (bending radius = 5 mm, deformation rate = 200 mm min<sup>-1</sup>). Inset shows a photograph of the bent nanomat anode sheet.

**Figure 2.69** dQ/dV plot of the nanomat (a) and slurry-cast, (b) anode sheets. (c) theoretical lithiation voltage ( $V_{\text{Li}}$ ) profile and optimized structure (insets) for the stepwise lithiation of CoTCPP, in which newly inserted Li<sup>+</sup> ions at each site are encircled.

**Figure 2.70** DFT-optimized structures and theoretical lithiation voltages ( $V_{\text{Li}}$ ) for investigation of the initial Li<sup>+</sup> ion insertion at various sites of CoTCPP.

**Figure 2.71** Electrostatic potential fields of CoTCPP. The electron-rich and electron-deficient regions are colored blue and red, respectively.

**Figure 2.72** (a) SEM images (cross-sectional) of the nanomat (left) and slurry-cast (right) anode sheets, (b) comparison of the areal masses [ $\text{mg cm}_{\text{anode}}^{-2}$ ] between the nanomat and slurry-cast anode sheets, (c) comparison of the lithiation profiles (expressed as capacity per weight of anode sheet ( $\text{mAh g}_{\text{anode}}^{-1}$ )): nanomat (red line) vs. slurry-cast (black line) anode sheets at a current density of 0.05 C.

**Figure 2.73** (a) Cycling performance of the nanomat anode sheet at lithiation/delithiation current densities of 5.0 C/5.0 C, (b) cross-sectional SEM images of nanomat anodes before (left) and after 1500 cycles (right).

## List of tables

### Chapter 1

**Table 1.1** General requirements of separator membranes for LIBs. (X. Zhang et al. Energy and Environment Science, 2014, 7, 3857)

**Table 1.2** Carbonates and esters as electrolyte solvents. (K. Xu, Chemical Reviews, 2004, 104, 4303)

**Table 1.3** Lithium salts as electrolyte solutes. (K. Xu, Chemical Reviews, 2004, 104, 4303)

### Chapter 2

**Table 2.1** Comparison of the gravimetric full cell capacity between the all-nanomat (Si/OLO) full cell (expressed as  $\text{mAh g}_{\text{Cell}}^{-1}$ ) and previously reported (Si anode-incorporating) full cells (expressed as  $\text{mAh g}_{\text{Si anode}}^{-1}$ ).

**Table 2.2** Quantitative analysis (estimated from ICP-MS) of the component contents in various samples.

**Table 2.3** Spectral band assignment of key elements in CC-nanohybrids (from XPS analysis).

**Table 2.4** Comparison of delithiation capacities and areal mass loading: CC-nanohybrids vs. previously reported organic anode materials.

**Table 2.5** Comparison of electrochemical performances between all-fibrous nanomat anode sheets (this study) and previously reported metallic current collector-free anode sheets.

## Chapter I. Introduction

### 1.1 Overview of rechargeable power sources

Ever-increasing popularization of high-performance portable electronics, flexible/wearable device, electric vehicles (EVs) and grid-scale energy storage systems (ESSs) has resulted in a relentless pursuit of advanced power sources with high energy density, electrochemical sustainability, and mechanical flexibility. Rechargeable (or secondary) batteries are among the most successful power source that can repeatedly generate electricity from stored materials and convert reversely electric energy into chemical energy.<sup>[1,2]</sup> A typical rechargeable battery consists of main components such as cathode, anode, separator, electrolytes. The basic principle of the rechargeable battery is based on the redox reaction (i.e., reduction and oxidation) of the electrode. In a discharging battery, electrochemical reduction reaction ( $A^+ + e^- \rightarrow A$ ) occur at the positive electrode. Electrons transferred from the negative electrode to positive electrode through the external circuit. At the same time, ion transport through the electrolyte balance the electroneutrality. Discharging is the process of converting electric energy carried by the battery into chemical energy. In the opposite case, an oxidation reaction occurs on the positive electrode when charging. Generally, the positive electrode is called cathode and the negative electrode is called anode based on discharge process. The redox reaction of the cathode and anode is relatively performed according to the reduction potential of the electrode active materials. Among both electrodes, the oxidation reaction occurs when the reduction potential is lower. The potential difference of both electrode redox reactions decides the operating voltage of the battery, while the capacity (given in Ah  $kg^{-1}$ ) depends on the number of electrons and the molecule weight of electrode active materials. Demanding characteristics for batteries include high energy density (Wh  $kg^{-1}$  or Wh  $L^{-1}$ ), high power density (W  $kg^{-1}$  or W  $L^{-1}$ ), durability, sustainability, safety, and cost.

Figure 1.1 shows various rechargeable power sources with Ragone plot.<sup>[3]</sup> Each rechargeable battery has different properties and different tailored applications. For example, the lead-acid battery is used for electric scooters that weight is less important. Ni-Cd battery shows a higher energy density and power density than the lead-acid battery does, but the costs are much higher. It is used for starting airplanes and electric vehicles. Supercapacitors can store and deliver energy very quickly at high current rates for a short time, which are capable of rapid charge/discharge and are used to replace batteries or batteries with high charge efficiency and semi-permanent cycle life characteristics. Lithium-ion battery achieves both the highest gravimetric energy and competitive power densities of all commercially available rechargeable batteries. This is why lithium-ion batteries are especially suitable for a variety of applications such as portable device and electric vehicles.<sup>[4]</sup>

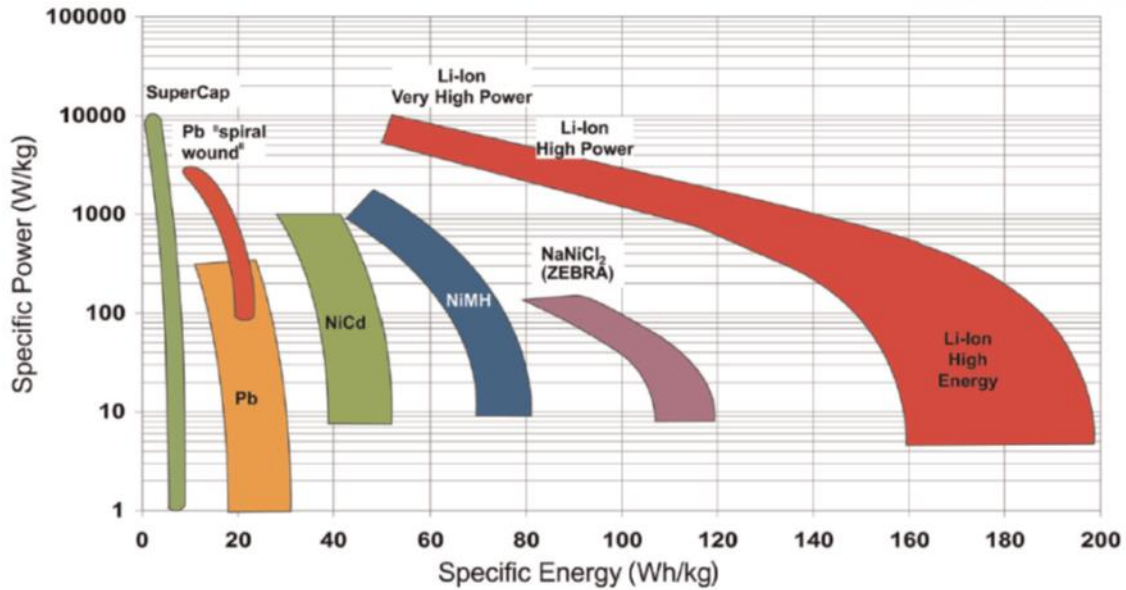


**Figure 1.1** Ragone plot of various rechargeable power sources. (D. U. Sauer et al. Proc IMechE Part D: J Automobile Engineering, 2013, 227, 761)

## 1.2 Principle of lithium-ion batteries

Among a variety of systems, lithium-ion batteries (LIBs) are the most suitable energy storage systems due to their high volumetric and gravimetric energy density. The motivation for using LIBs is from not only the lowest reduction potential ( $-3.04\text{V}$  vs. standard hydrogen electrode (SHE)) but also the lightest weight (equivalent weight  $M = 6.94 \text{ g mol}^{-1}$ , and specific gravity  $\rho = 0.53 \text{ g cm}^{-3}$ ). Since Sony had introduced the commercial LIB technology based on lithium-ion intercalation compounds in 1991. This type of LIB has presented an operating potential exceeding  $3.6\text{V}$  (three times that of alkaline types) and higher gravimetric energy densities ( $150 \text{ Wh Kg}^{-1}$ ) than usual Ni-Cd batteries. LIBs are still spotlighted as the most attractive energy storage system because of their long cycle life and low self-discharging.<sup>[5,6]</sup> The main components of commercial LIBs are lithium cobalt oxide ( $\text{LiCoO}_2$ , as a cathode), graphite ( $\text{C}_6$ , as an anode), polyolefin separator and organic carbonate electrolytes. Both electrodes can store the lithium-ions by a redox reaction. The lithium-ions move from  $\text{LiCoO}_2$  to Graphite with the deintercalation/intercalation process through the separator and electrolyte during charging. The process is reversed on discharge. Figure 1.2 shows the schematic of a discharge process of LIBs. The following equations exhibit the overall redox reactions.



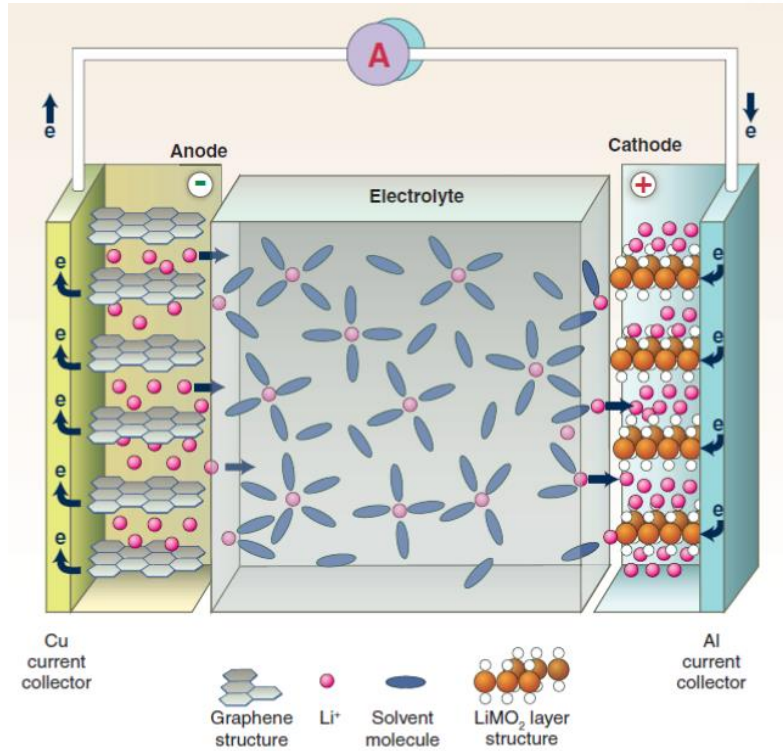


**Figure 1.2** Schematic of a discharge process of lithium-ion battery (J.-M. Tarascon Science, 2011, 35, 928)

### 1.3 Lithium-ion battery materials

#### 1.3.1 Cathodes active materials

Lithium transition metal oxides are most commonly used for cathode active materials. They can be classified into three major categories:  $\text{LiMO}_2$  (M denotes a transition metal) with the layered structure,  $\text{LiM}_2\text{O}_4$  with the spinel structure and polyanion-based compounds with the olivine structure. Their structures are shown in Figure 1.3.

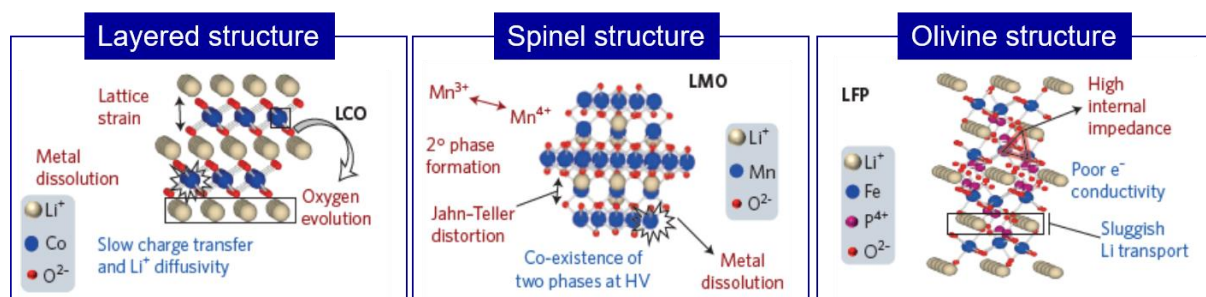


**Figure 1.3** Various structures of cathode materials (P. M. Ajayan et al. Nature energy, 2017, 2, 17108)

The layered structure cathodes (including  $\text{LiCoO}_2$ ,  $\text{LiNiO}_2$ , and  $\text{LiMnO}_2$ ) have a high theoretical

capacity assuming complete Li extraction. However, the reversible capacity of the layered structure is limited to about half of theoretical value due to the structural degradation by deintercalation of lithium-ions. Previous studies on this issue have focused on surface doping and coating for improving structural stability. The spinel lithium manganese oxide ( $\text{LiMn}_2\text{O}_4$ ) has attracted continued interest as a promising cathode material owing to its good rate capability, favorable safety, and natural abundance. Despite these advantageous characteristics, practical application of  $\text{LiMn}_2\text{O}_4$  materials is staggering due to several formidable challenges mainly because of the problems with Jahn-Teller distortion and Mn ion dissolution in the electrolyte. To overcome the intrinsic issues, the nanostructured and coated active materials were performed. Polyanion-based compounds ( $\text{Li}_x\text{M}_y(\text{XO}_4)_z$ , X = P, S, Si, etc) are considered as the most promising materials for LIBs to the power source of electric vehicles due to their high safety. Among them,  $\text{LiFePO}_4$  is the most studied materials. Because this has merits including high reversible capacity ( $170\text{mAh g}^{-1}$ ) and favorable reversibility of lithium-ion storage. However, the rate capability of the material is insufficient owing to the intrinsic electronic conductivity and lithium-ion diffusivity. Moreover, it is difficult to increase energy density because the reduction potential is lower ( $\sim 3.4\text{V}$ ) than other materials.<sup>[7,8]</sup>

### 1.3.2 Anode active materials

The anode active materials can be classified according to the mechanism such as intercalation, alloy, and conversion that react with lithium ion. A commercialized anode material, graphite stores lithium ion according to the intercalation/deintercalation mechanism. Therefore, the theoretical capacity is limited to  $372\text{mAh g}^{-1}$ . To increase the energy density of LIBs, alloy and conversion type materials have been studied to create more active spaces or sites for lithium-ion storage. Among the various alloy compounds candidates (e.g., Si, Sn, Ge, Al and Sb) Silicon (Si) have garnered considerable attention as potential alternatives beyond graphite, due to high theoretical capacities ( $4,200\text{mAh g}^{-1}$ ) and an appropriate discharge voltage at  $0.4\text{V}$  (vs.  $\text{Li/Li}^+$ ) in average. Unfortunately, the main challenges of silicon anode are the intrinsic low electronic conductivity and huge volume change ( $\sim 300\%$ ) during alloying/dealloying process. Especially, the volume variation induces the break of a conductive network in the electrode resulting in the severe capacity fade. In case of the transition metal oxide as a conversion type materials (e.g.,  $\text{M}_x\text{O}_y$ , M = Fe, Co, Ni, Mn, Ti, and Cu), they have low reversibility by volume variation and high redox potential. Moreover, they are higher than graphite but have lower capacity than Si. So, further considerations include the development of electrochemical characteristics are needed. Several anode materials for application in LIBs are presented by Figure 1.4. <sup>[9,10]</sup>

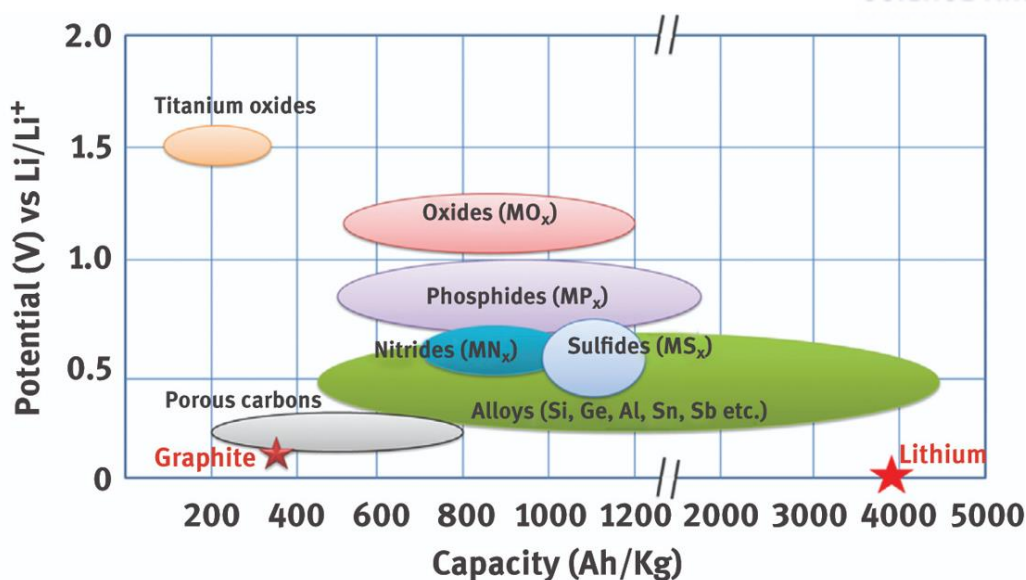


**Figure 1.4** Several anode materials for LIBs (C. Capiglia et al. Journal of Power sources, 2014, 257, 421)

### 1.3.3 Separators

The separator is placed between the cathode and anode. The essential properties of the separator of LIBs are wettability by the liquid electrolyte, high porosity for ion transport. General requirements of separator for LIBs are exhibited in Table 1.1. <sup>[11]</sup> The separator should also have high mechanical properties including tensile strength and puncture strength to prevent an internal short circuit. Commercial polyolefin separators (polyethylene (PE), polypropylene (PP) and their combinations) of LIBs are fabricated by orientation to the machine direction (MD) or transverse direction (TD). For this reason, the commercial separator has intrinsic limitations that arising from the non-uniform porous structure and insufficient thermal/mechanical properties raise problems regarding ion transport related to electrochemical performance and electrical isolation related to battery safety issues. <sup>[12,13]</sup>

### 1.3.4 Electrolytes

Commercial electrolytes which are a liquid state at the usage-temperature range of LIB are consist of a lithium salt and organic solvent mixture (A variety of lithium salt and solvent are shown in Table 1.2 and 1.3). <sup>[14]</sup> Electrolytes serve to carry lithium-ion between cathode and anode without electron transport. Therefore, excellent ionic conductivity and redox stability are required. Design of electrolyte materials is important because electrolyte decomposition within battery operating voltage range causes poor battery performance. Also, the electrolyte/electrode active material interfacial characteristics should be considered. The solid electrolyte interphase (SEI) layer is formed on the surface of the active

material by additional reaction between electrolyte and electrode. Since the SEI layer affects lithium-ion diffusivity and additional side reaction during charging/discharging process, continuous research and analysis are necessary. [15,16]

Parameter	Requirement
<b>Chemical and electrochemical stabilities</b>	stable for a long period of time
<b>Wettability</b>	wet out quickly and completely
<b>Mechanical property</b>	> 1000 kg/cm (98.06 MPa)
<b>Thickness</b>	20 – 25 $\mu\text{m}$
<b>Pore size</b>	< 1 $\mu\text{m}$
<b>Porosity</b>	40-60%
<b>Permeability (Gurley)</b>	< 0.025 sec/ $\mu\text{m}$
<b>Dimensional stability</b>	no curl up and lay flat
<b>Thermal stability</b>	< 5% shrinkage after 60 min at 90 °C
<b>Shutdown</b>	effectively shut down the battery at elevated temperatures

**Table 1.1** General requirements of separator membranes for LIBs (X. Zhang et al. Energy and Environment Science, 2014, 7, 3857)

Solvent	Structure	M. Wt	$T_m/^\circ\text{C}$	$T_b/^\circ\text{C}$	$\eta/\text{cP}$ 25 °C	$\epsilon$ 25 °C	Dipole Moment/debye	$T_f/^\circ\text{C}$	$d/\text{gcm}^{-3}$ , 25 °C
EC		88	36.4	248	1.90, (40 °C)	89.78	4.61	160	1.321
PC		102	-48.8	242	2.53	64.92	4.81	132	1.200
BC		116	-53	240	3.2	53	4.23	97	1.199
$\gamma$ BL		86	-43.5	204	1.73	39	4.29	81	1.057
$\gamma$ VL		100	-31	208	2.0	34	4.52	110	1.17
NMO		101	15	270	2.5	78	0.76	18	1.063
DMC		90	4.6	91	0.59 (20 °C)	3.107	0.96	31	0.969
DEC		118	-74.3 <sup>a</sup>	126	0.75	2.805	0.89		1.006
EMC		104	-53	110	0.65	2.958	6.02	-3	0.902
EA		88	-84	77	0.45			11	0.898
MB		102	-84	102	0.6			19	0.878
EB		116	-93	120	0.71				

**Table 1.2** Carbonates and esters as electrolyte solvents (K. Xu, Chemical Reviews, 2004, 104, 4303)

Salt	Structure	M. Wt	$T_m/^\circ\text{C}$	$T_{\text{decomp.}}/^\circ\text{C}$ in solution	Al-corrosion	$\sigma/\text{mS cm}^{-1}$ (1.0 M, 25 °C)	
						in PC	in EC/DMC
<b>LiBF<sub>4</sub></b>		93.9	293 (d)	> 100	N	3.4 <sup>a</sup>	4.9 <sup>c</sup>
<b>LiPF<sub>6</sub></b>		151.9	200 (d)	~ 80 (EC/DMC)	N	5.8 <sup>a</sup>	10.7 <sup>d</sup>
<b>LiAsF<sub>6</sub></b>		195.9	340	> 100	N	5.7 <sup>a</sup>	11.1 <sup>c</sup>
<b>LiClO<sub>4</sub></b>		106.4	236	>100	N	5.6 <sup>a</sup>	8.4 <sup>d</sup>
<b>Li Triflate</b>	$\text{Li}^+ \text{CF}_3\text{SO}_3^-$	155.9	>300	>100	Y	1.7 <sup>a</sup>	
<b>Li Imide</b>	$\text{Li}^+ [\text{N}(\text{SO}_2\text{CF}_3)_2]^-$	286.9	234 <sup>b</sup>	>100	Y	5.1 <sup>a</sup>	9.0 <sup>e</sup>
<b>Li Beti</b>	$\text{Li}^+ [\text{N}(\text{SO}_2\text{CF}_2\text{CF}_3)_2]^-$				N		

**Table 1.3** Lithium salts as electrolyte solutes (K. Xu, Chemical Reviews, 2004, 104, 4303)

### 1.3.5 Electrode components

It is well known that electrodes mainly determine the capacity and rate capability of battery performance. Since the redox reaction occurs in the electrode, the ion/electron networks of the electrode are very important. Therefore many previous studies focused on the novel materials which have high ionic/electronic conductivity. The conventional electrodes are generally composed of electrode active materials (e.g., cathode active material and anode active material) and non-faradaic additives (e.g., conductive carbon materials, polymeric binders, and metallic current collectors). For improvement for the energy density of LIBs, high capacity active materials are considered. However, no matter how uses the high capacity electrode materials, it is not enough to the high-performance electrode. [17,18]

Conductive carbon materials provide electron pathway from current collector to active materials. The carbon material is suitable as a conductive material because it has high intrinsic electronic conductivity and non-faradaic reaction. Nano-sized carbon materials including carbon black are generally used because it can form enough electron network by small amounts. Polymeric binders act as an adhesive between the electrode active materials and the conductive carbon materials and the current collector. They should have redox stability and mechanical/structural durability during repeating of the battery cycling. Polyvinylidene fluoride (PVDF) for the cathode and carboxymethyl cellulose (CMC)/styrene butadiene rubber (SBR) for the anode are typically applied as binders. Current collectors play a vital role in gathering and transferring of an electron from an external circuit to the electrode. Metallic foil is considered as a general current collector due to robust mechanical properties and excellent electronic

conductivity. There are many metal candidates, but the well-fitted materials are selected depending on the redox stability. Aluminum (Al) and Copper (Cu) are applied to cathode current collector and anode current collector respectively. [19,20]

#### 1.4 Research objective

The ultimate goal of battery technology development is to increase energy density. Energy density ( $\text{Wh kg}^{-1}$  or  $\text{Wh L}^{-1}$ ) is a multiplication of capacity ( $\text{Ah kg}^{-1}$  or  $\text{Ah L}^{-1}$ ) and operating voltage (V). In other words, the greater the capacity of the active material and the greater the difference between cathode and anode operating potentials, are the better (Figure 1.5). [17] Therefore, numerous studies focus on electrode active materials by now. However, the electrode active material is mixed with the binder and conductive material to form a typical electrode, so structure and effectiveness of the ion/electron pathway in the electrode are definitely a key factor governing energy density. The objective of this research is to design and provide a new class of electrode architecture for high energy density lithium-ion batteries.

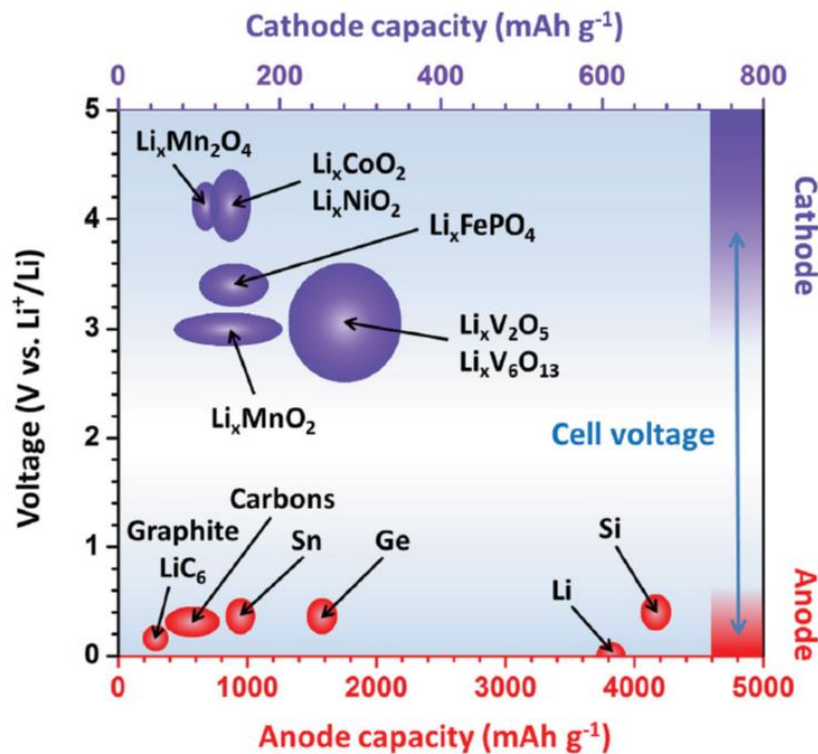


**Figure 1.5** Diagram illustrating the capacities and electrochemical potentials of important cathode and anode materials (Y. Lei et al., *Advanced Energy Materials*, 2016, 6, 1502514)

### 1.4.1 Limitations of the conventional electrode architecture

From the electrode architecture point of view, a typical conventional electrode consists of a random pile-up of electrode active materials, conductive carbon powder, and polymeric binders on top of metallic foil current collectors. This monotonous architecture has several drawbacks.<sup>[17,18]</sup>

First, the random stacking of electrode components such as active materials, conductive additives, and polymeric binders causes irregular electron/ion transport pathway through-thickness direction. Second, the incomplete electron/ion transport pathway increases unnecessary electrochemical polarization. Third, the non-faradaic materials such as metallic current collector, conductive additives and polymeric binders account for a great part of the total mass of electrode, resulting in lower areal capacity and energy densities of the LIBs. Furthermore, due to the flat and smooth surface of the metallic current collector, a very weak adhesion and limited contact between the electrode materials and the current collector resulting in weak mechanical deformation. Figure 1.6 shows the schematic illustration of the above-mentioned drawbacks.

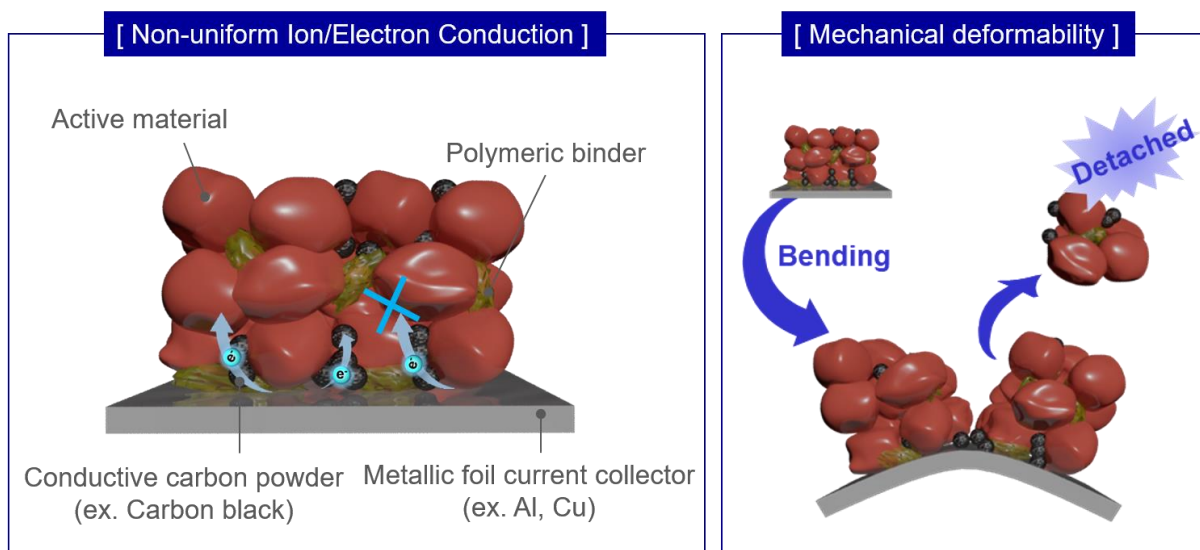


**Figure 1.6** Schematic illustration of the drawbacks of the conventional electrode architecture

### 1.4.2 Research progress in electrode architecture for LIBs

There are four strategies about electrode architecture classified as fabrication methods. Using the textile or carbon form as the 3D conductive substrate is an initial version of electrode architecture studies. These 3D substrate act as a flexible, strong current collector which easy to allow for fast ion/electron migrations (Figure 1.7a). However, the coating or impregnation method can load only a very small amount of active material on the current collector.<sup>[21,22]</sup>

In the case of hydrogels and aerogels, they got a high porosity, providing excellent electrolyte wettability and fast conduction pathways resulting in enhancement of electrochemical properties (Figure 1.7b).<sup>[23,24]</sup> But, they often suffer limitation of mechanical flexibility owing to weak physical properties.

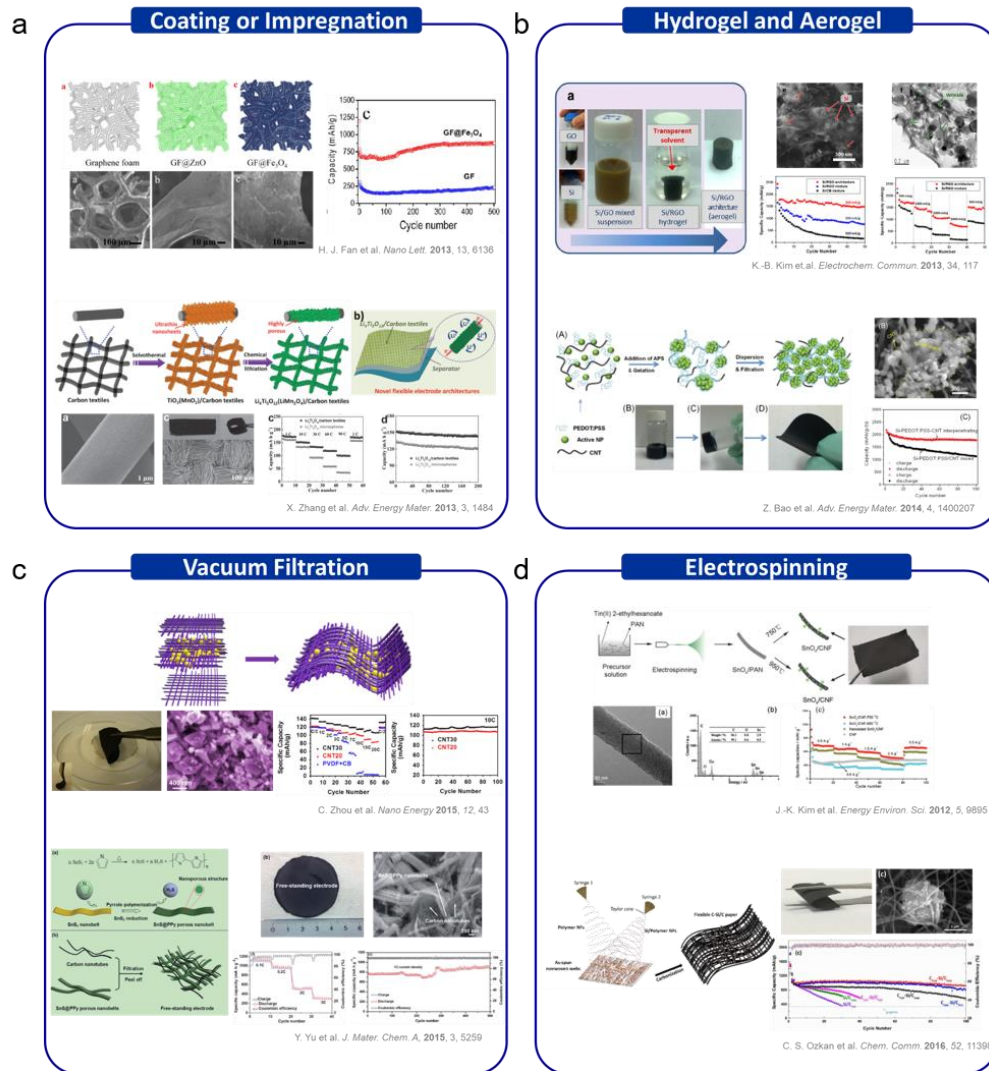


**Figure 1.7** Previous studies about electrode architectures for LiBs classified as fabrication methods; (a) coating or impregnation, (b) hydrogel and aerogel, (c) vacuum filtration, (d) electrospinning

One of the popular approaches to forming a uniform conducting network in the electrode is vacuum filtration. They generally use mixed suspension solutions of electrically conductive materials with active materials for the improvement of the rate and cycling capabilities (Figure 1.7c).<sup>[25,26]</sup> However, it is difficult to make large-scaled electrodes.

To improve the electrochemical properties, free-standing 3D mat electrode consisting of active material/carbon fibers produced by electrospinning (Figure 1.7d).<sup>[27,28]</sup> But the active material loading is limited by covering the surface of the carbon mat. Furthermore, they have a limitation of mechanical

flexibility because they were carbonized to obtain electrical conductivity.

These previous works showed some meaningful results, however, most of them still suffered from the limitations in mass loading of electrode active materials, mechanical flexibility, and manufacturing processability.

### 1.4.3 Strategies

To realize the aforementioned goal, our primary interest is focused on the design/synthesis of multifunctional polymer fibrils and also heteronanomat (HM) electrode architecture, along with a proper selection of target electrode active materials. In addition, much attention should be also devoted to manufacturing processes and optimization fabrication conditions for the HM electrodes. To explore the potential applicability of the HM electrodes for LIBs, structural/electrochemical characterizations are comprehensively conducted, with a particular focus on 3D-reticulated, bicontinuous ion/electron conduction pathways.

### 1.5 References

1. C. Liu, F. Li, L.-P. Ma, H.-M. Cheng, *Adv. Mater.* **2010**, 22, E28.
2. F. Cheng, J. Liang, Z. Tao, J. Chen, *Adv. Mater.* **2011**, 23, 1695.
3. H. Budde-Meiwes, J. Drillkens, B. Lunz, J. Muennix, S. Rothgang, J. Kowal, D. U. Sauer, *Proc IMechE Part D: J Automobile Engineering* **2013**, 227, 761.
4. C. P. Grey, J. M. Tarascon, *Nat. Mater.* **2017**, 16, 45.
5. J.-M. Tarascon, M. Armand, *Nature* **2001**, 414, 359.
6. J. W. Choi, D. Aurbach, *Nat. Rev. Mater.* **2016**, 1, 1.
7. M.-T. F. Rodrigues, G. Babu, H. Gullapalli, K. Kalaga, F. N. Sayed, K. Kato, J. Joyner, P. M. Ajayan *Nat. Energy* **2017**, 2, 17108.
8. M. S. Whittingham, *Chem. Rev.* **2004**, 104, 4271.
9. S. Goriparti, E. Miele, F. D. Angelis, E. D. Fabrizio, R. P. Zaccaria, C. Capiglia, *J. Power Sources* **2014**, 257, 421.
10. J. Lu, Z. Chen, Z. Ma, F. Pan, L. A. Curtiss, K. Amine, *Nat. Nanotech.* **2016**, 11, 1031.
11. H. Lee, M. Yanilmaz, O. Toprakci, K. Fu, X. Zhang, *Energy Environ. Sci.* **2014**, 7, 3857.
12. J. B. Goodenough, K.-S. Park, *J. Am. Chem. Soc.* **2013**, 135, 1167.
13. P. Arora, Z. J. Zhang, *Chem. Rev.* **2004**, 104, 4419.
14. K. Xu, *Chem. Rev.* **2004**, 104, 4303.
15. A. M. Haregewoin, A. S. Wotango, B.-J. Hwang, *Energy Environ. Sci.* **2016**, 9, 1955.
16. W. Xu, X. Chen, F. Ding, J. Xiao, D. Wang, A. Pan, J. Zheng, X. S. Li, A. B. Padmaperuma, J.-G. Zhang, *J. Power Sources* **2012**, 213, 304.
17. Y. Xu, M. Zhou, Y. Lei, *Adv. Energy Mater.* **2016**, 6, 1502514.
18. M. Yousaf, H. T. H. Shi, Y. Wang, Y. Chen, Z. Ma, A. Cao, H. E. Naguib, R. P. S. Han, *Adv. Energy Mater.* **2016**, 6, 1600490.

19. Y. Lee, J. Choi, M.-H. Ryou, Y. M. Lee, *Poly. Sci. Tech.* **2013**, 24, 603.
20. J. W. Braithwaite, A. Gonzales, G. Nagasubramanian, S. J. Lucero, D. E. Peebles, J. A. Ohlhausen, W. R. Cieslak, *J. Electrochem. Soc.* **1999**, 146, 448.
21. J. Luo, J. Liu, Z. Zeng, C. F. Ng, L. Ma, H. Zhang, J. Lin, Z. Shen, H. J. Fan, *Nano Lett.* **2013**, 13, 6136.
22. L. Shen, B. Ding, P. Nie, G. Cao, X. Zhang, *Adv. Energy Mater.* **2013**, 3, 1484.
23. Z. Chen, J. W. F. To, C. Wang, Z. Lu, N. Liu, A. Chortos, L. Pan, F. Wei, Y. Cui, Z. Bao, *Adv. Energy Mater.* **2014**, 4, 1400207.
24. S.-H. Park, H.-K. Kim, D.-J. Ahn, S.-I. Lee, K. C. Roh, K.-B. Kim, *Electrochem. Commun.* **2013**, 34, 117.
25. X. Fang, C. Shen, M. Ge, J. Rong, Y. Liu, A. Zhang, F. Wei, C. Zhou, *Nano Energy* **2015**, 12, 43.
26. J. Liu, Y. Wen, P. A. Aken, J. Maier, Y. Yu, *J. Mater. Chem. A*, **2015**, 3, 5259.
27. B. Zhang, Y. Yu, Z. Huang, Y.-B. He, D. Jang, W.-S. Yoon, Y.-W. Mai, F. Kang, J.-K. Kim, *Energy Environ. Sci.*, **2012**, 5, 9895.
28. C. Li, C. Liu, W. Wang, J. Bell, Z. Mutlu, K. Ahmed, R. Ye, M. Ozkan, C. S. Ozkan, *Chem. Commun.* **2016**, 52, 11398

## Chapter 2. Electrospayed CNT/electrospun polymer heteronanomat-mediated LIB electrodes

### 2.1 One-dimensional building elements-intermingled heteronanomats as a platform architecture for superior performance ultrahigh-capacity lithium-ion battery cathodes

#### 2.1.1 Introduction

To date, numerous studies have been undertaken to continuously improve electrochemical performances of lithium-ion batteries, with a particular focus on their energy density. The core battery materials such as electrode active materials, electrolytes, and separator membranes have been developed by most of the research activities.<sup>[1-4]</sup>

From the electrode architecture point of view, most conventional electrodes are fabricated by a simple and random pile-up of electrode active materials and non-faradaic additives on top of metallic foil current collectors. Unfortunately, such a stereotyped electrode architecture often gives rise to non-uniform and sluggish ion/electron transport particularly in their through-thickness direction and is also vulnerable to structural disruption upon mechanical deformation.<sup>[5-7]</sup> Especially, the irregular ion/electron conduction pathways of the electrodes eventually lead to unwanted electrochemical polarization, which becomes more serious at harsh operating conditions such as high-mass loading electrodes and fast charge/discharge current densities that are urgently needed for high-energy EV batteries. Due to these inevitable limitations, the conventional electrode architecture has posed a formidable challenge to sustainable progress of battery performance, thus pushing us to search for alternative solutions.<sup>[8,9]</sup>

In pursuit of the higher energy density of electrodes, a minimal use of non-faradaic (e.g., electrochemically-inactive) materials including metallic foil current collectors, polymeric binders and conductive additives is strongly preferred. In order to develop the binder-/conductive powder-/current collector-free electrodes, a number of approaches have been reported, which could be largely classified as follows: i) self-standing carbon nanofibers (or carbon nanotubes (CNTs)) sheets containing electrode active materials, including CNTs/LiNi<sub>0.5</sub>Mn<sub>1.5</sub>O<sub>4</sub> electrodes prepared by vacuum filtration process,<sup>[5,10]</sup> CNTs/Fe<sub>3</sub>O<sub>4</sub> composite electrodes via polyacrylic acid-assisted assembly,<sup>[11]</sup> CNTs/Li<sub>4</sub>Ti<sub>5</sub>O<sub>12</sub> composite electrodes fabricated through aerosol spray process,<sup>[3,12]</sup> CNTs/conducting polymer hydrogel network electrodes,<sup>[6]</sup> ii) coating or impregnation of electrode active materials into pre-formed electroconductive porous scaffolds made of graphite foam,<sup>[7,8]</sup> carbon textile<sup>[13]</sup> and carbon cloth<sup>[14,15]</sup>. These previous works showed some meaningful results, however, most of them have still suffered from the limitations in mass loading of electrode active materials, structural integrity, mechanical flexibility, and manufacturing processability.

Here, as a facile and versatile electrode strategy to resolve the long-standing challenges of conventional electrodes mentioned above, we demonstrate a new class of heteronanomat-architected electrodes (referred to as HM electrodes), which comprise one-dimensional (1D) nanobuilding blocks of polyacrylonitrile (PAN) nanofibers/multi-walled carbon nanotubes (MWCNTs)-mediated heteronanomat and densely-packed electrode active particles. The HM electrodes are fabricated through simultaneous electrospinning (for MWCNTs/electrode active powders) and electrospinning process (for PAN nanofibers) without the use of typical polymer binders, carbon powder conductive additives and metallic foil current collectors. Notably, the electrospun MWCNTs and electrospun PAN nanofibers are intermingled in close contact with the electrode active particles, eventually leading to electrode active particles-embedded self-standing heteronanomat electrodes. The PAN nanofibers act as a mechanically-reinforcing building element and also 1D-shaped electrode binders. The MWCNTs build well-interconnected electronic networks and also play a role as an alternative current collector.

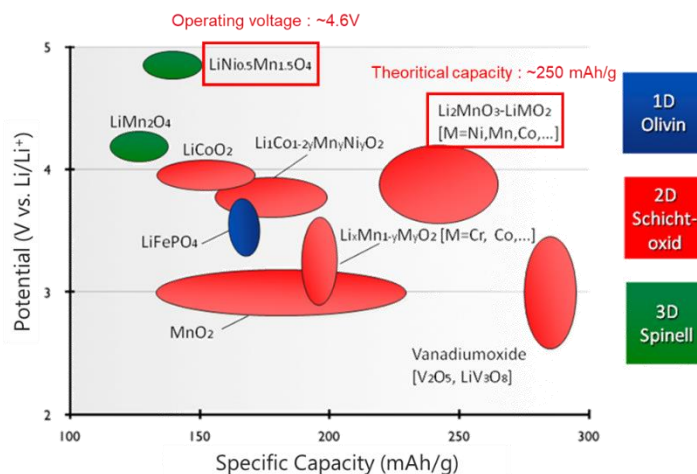


**Figure 2.1** OLO and LNMO cathode materials respectively represent high-capacity and high-voltage cathode materials (S. Passerini et al. Adv. Energy Mater. 2016, 6, 1600906)

Such uniqueness in the materials/architecture of the HM electrodes is anticipated to enable substantial improvements in the electrochemical performance and mechanical flexibility far beyond those accessible with conventional electrode technologies. First, the removal of metallic current collectors in the HM electrodes allows larger amount of electrode active materials to be loaded in a fixed weight/volume of electrodes. Moreover, the HM electrodes are free from metallic foil current collectors-induced spatial blocking of ion transport between adjacent electrodes and thus can be multiple-stacked in series, eventually achieving a remarkable increase in areal active-mass loading of electrodes. Second, owing to the PAN nanofibers/MWCNTs-intermingled heteronanomat architecture, MWCNT electronic networks and also interstitial void channels (allowing facile electrolyte accessibility) are uniformly

formed in the through-thickness direction of the HM electrodes, thereby constructing three-dimensional (3D) bincontinuous ion/electron conduction pathways which can mitigate electrochemical polarization and also facilitate redox reaction kinetics. Third, the highly-networked heteronanomat architecture contributes to mechanical flexibility and dimensional tolerance of the HM electrodes. Fourth, a variety of electrode active materials can be adopted in the HM electrodes, underscoring their versatility and universality as a new concept of electrode platform. As a proof-of-concept for the HM electrodes, we chose two representative cathode active materials, which were over-lithiated layered oxide (OLO,  $0.49\text{Li}_2\text{MnO}_3 \cdot 0.51\text{LiNi}_{0.37}\text{Co}_{0.24}\text{Mn}_{0.39}\text{O}_2$ )<sup>[16]</sup> and spinel-type  $\text{LiNi}_{0.5}\text{Mn}_{1.5}\text{O}_4$  (LNMO)<sup>[17]</sup>. Among various cathode materials, OLO and LNMO powders respectively represent high-capacity and high-voltage cathode materials (Figure 2.1), which have attracted great attention as promising candidates to enable high energy (= capacity  $\times$  voltage) density cells.

## 2.1.2 Experimental section

### 2.1.2.1 Architectural design and fabrication of HM cathode

The HM cathodes were fabricated through the simultaneous electrospaying (for MWCNTs/cathode active powders) and electrospinning (for PAN nanofibers). As cathode active materials,  $0.49\text{Li}_2\text{MnO}_3 \cdot 0.51\text{LiNi}_{0.37}\text{Co}_{0.24}\text{Mn}_{0.39}\text{O}_2$  (OLO, average diameter  $\sim 5 \mu\text{m}$ ) or  $\text{LiNi}_{0.5}\text{Mn}_{1.5}\text{O}_4$  (LNMO, average diameter  $\sim 14 \mu\text{m}$ ) were chosen. To enable the electrospaying process without sedimentation problem, the cathode active materials were down-sized to nanopowders by ball milling in water. The prepared active nanoparticles were then mixed with the MWCNTs in water/isopropyl alcohol (IPA) (= 70/30 (w/w)) mixture solvent using sonication for 1.5 h, wherein 0.5 wt.% polyvinylpyrrolidone (PVP) was used as a dispersing additive for MWCNTs. At the same time, PAN (molecular weight = 150,000  $\text{g mol}^{-1}$ ) was dissolved in dimethylformamide (DMF) at  $80 \text{ }^\circ\text{C}$  for 12 h, wherein the PAN concentration was 10 wt.%. The OLO/MWCNT mixture solution and the PAN solution were respectively subjected to simultaneous electrospaying/electrospinning through different nozzles at room temperature, thus producing the cathode active nanoparticles-embedded PAN/MWNT heteronanomat sheet. The detailed processing conditions were 7 kV with a feed rate of  $5 \mu\text{L min}^{-1}$  (for electrospinning) and 15 kV with a feed rate of  $70 \mu\text{L min}^{-1}$  (for electrospaying). The resulting heteronanomat sheet was collected on a stainless steel plate. After the PVP additives were removed with water (followed by ethanol), the heteronanomat sheet was thermally treated ( $120 \text{ }^\circ\text{C}/12 \text{ h} \rightarrow 150 \text{ }^\circ\text{C}/2 \text{ h}$  in a vacuum oven) in order to improve chemical resistance of the PAN nanofibers and then roll-pressed at room temperature. Finally, the self-standing heteronanomat-architected cathodes were obtained. As a control sample, a conventional cathode was fabricated by casting a slurry mixture (cathode active materials/carbon black

conductive additive/polyvinylidene fluoride (PVDF) binder = 80/10/10 (w/w/w) in NMP) on an Al foil current collector.

#### 2.1.2.2 Structural/physicochemical characterization of HM cathodes

The particle size and structural phase of cathode active materials were analyzed by TEM (JEM-2100F, JEOL) and powder XRD (D/MAZX 2500V/PC) measurements. The surface and cross-sectional porous morphologies of HM cathodes were investigated using FE-SEM (S-4800, Hitachi) and EDS (JSM 6400, JEOL). The electrolyte wettability of HM cathodes was estimated by measuring electrolyte immersion-height. The composition ratio of HM cathodes was determined from the TGA measurement (SDT Q600, TA Instruments) at a heating rate of 5 °C min<sup>-1</sup> under air atmosphere. The electronic conductivities of HM cathodes were measured using a four-point probe technique (CMT-SR1000N, Advanced Instrument Technology). The Raman spectra were recorded by a micro-Raman spectroscope (alpha 300R, WITec) equipped with He/Ne laser (2 mW, 532 nm). The structural change of cathode surface after cycling test was analyzed using TOF-SIMS (ION TOF) with Bi<sub>3</sub><sup>2+</sup> gun (50 keV, 0.32 pA)

#### 2.1.2.3 Electrochemical performance of HM cathodes

The electrochemical performance of HM cathodes was characterized using a 2032-type coin half cell (= HM cathode/PE separator (thickness = 20 μm, Toray-tonen)/Li metal, 1 M LiPF<sub>6</sub> in EC/DMC = 1/1 (v/v)). All assembly of cells was carried out in an argon-filled glove box. The cell performance was investigated using a cycle tester (PNE Solution) at various charge/discharge conditions. The GITT analysis was performed with a potentiostat/galvanostat (VSP classic, Bio-Logic).

### 2.1.3 Result and discussion

#### 2.1.3.1 Structural and physicochemical properties of HM OLO cathode

To fabricate the HM OLO cathode, the OLO powders (average diameter ~ 5 μm) were dispersed in water/IPA (= 7/3 (w/w)) mixture solvent. An important prerequisite for the electro spraying process is to ensure no sedimentation of electrode active powders in the dispersion solution. The pristine OLO powders, due to their large particle size and density (= 2.85 g cc<sup>-1</sup>), were easily precipitated in the dispersion solution (Figure 2.2). In order to resolve this sedimentation problem, the OLO particles were down-sized to nanopowders by ball-milling.<sup>[18]</sup>

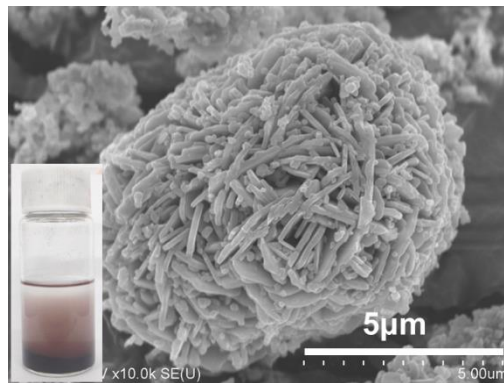


**Figure 2.2** A SEM image of pristine (micro-sized) OLO powders, wherein an inset is a photograph showing the precipitation of OLO-dispersed solution.

As a result, the precipitation problem was not observed even after being stored at 5 h (Figure 2.3a) The high-resolution transmission electron microscopy (HR TEM) image verifies the reduction of the particle size and also no disruption of layered crystal structure of the OLO nanopowders (Figure 2.3b). The X-ray diffraction (XRD) patterns confirm that hexagonal  $\alpha$ - $\text{NaFeO}_2$  structure<sup>[19]</sup> was clearly found in the OLO nanopowders as well as micro-sized OLO ones (Figure 2.4a). The charge/discharge profiles of half cells (OLO cathode/Li metal anode) showed an inappreciable difference in the charge/discharge reaction between the micro and nano OLO powders (Figure 2.4b).

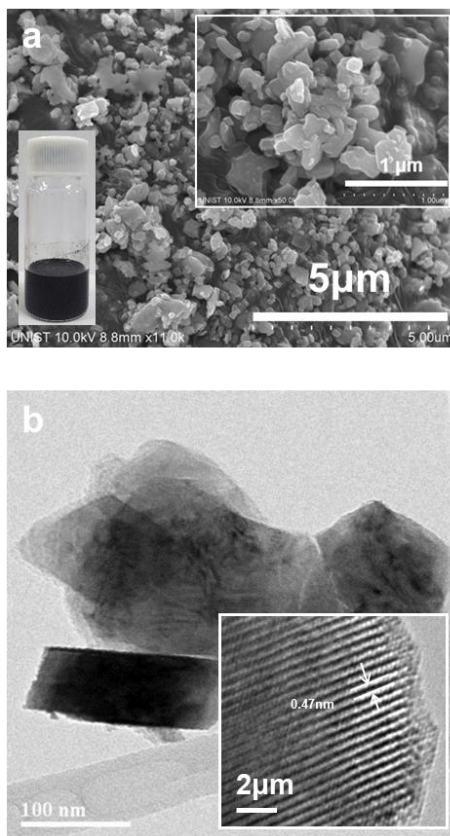


**Figure 2.3** (a) SEM images of OLO nanopowders, wherein an inset is a photograph showing that the good dispersion state of OLO nanopowders in the solution after being stored at 5 h. (b) HR TEM images of OLO nanoparticles.

The prepared OLO nanopowders were then mixed with the MWCNTs in water/IPA mixture solvent, wherein the composition ratio of OLO/MWCNT was 100/5 (w/w) and 0.5 wt.% PVP<sup>[20]</sup> was used as a dispersing additive for MWNTs. Meanwhile, PAN was dissolved in DMF, wherein the PAN concentration was 10 wt.%. The OLO/MWCNT mixture solution and the PAN solution were respectively subjected to simultaneous electrospinning/electrospinning through different nozzles (schematic illustration was shown in Figure 2.5), thus producing nano OLO-embedded PAN/MWNT heteronanomat sheet. After the PVP additives were removed with water (followed by ethanol), the heteronanomat sheet was thermally treated (120 °C/12 h → 150 °C/2 h in a vacuum oven) in order to improve chemical tolerance of PAN nanofibers<sup>[21,22]</sup> and then roll-pressed at room temperature. Finally, the self-standing HM OLO cathode was obtained. From the initial composition ratio of OLO/MWCNT (= 95.2/4.8 (w/w)) and the thermogravimetric analysis (TGA) measurement (Figure 2.6), the composition ratio of the HM OLO cathode was estimated to be (OLO/MWCNT)/PAN = (74.0/3.7)/22.3 (w/w/w).

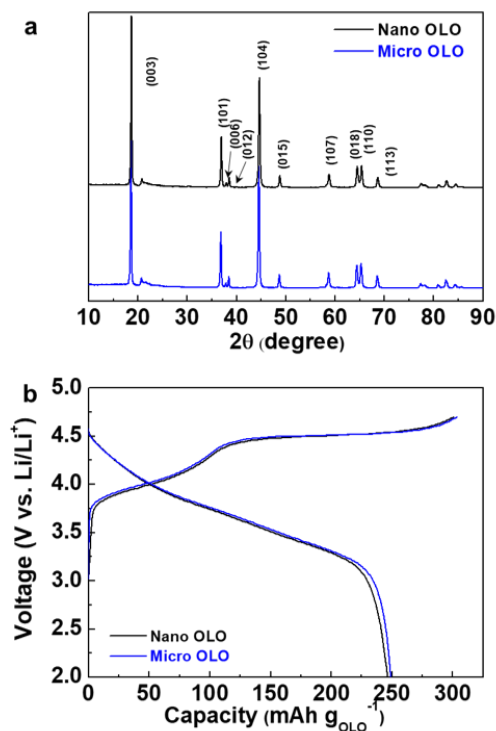


**Figure 2.4** Comparison in pristine (= microsized) and nanosized OLO powders: (a) XRD patterns; (b) charge/discharge profiles (current density = 0.1 C/0.1 C).

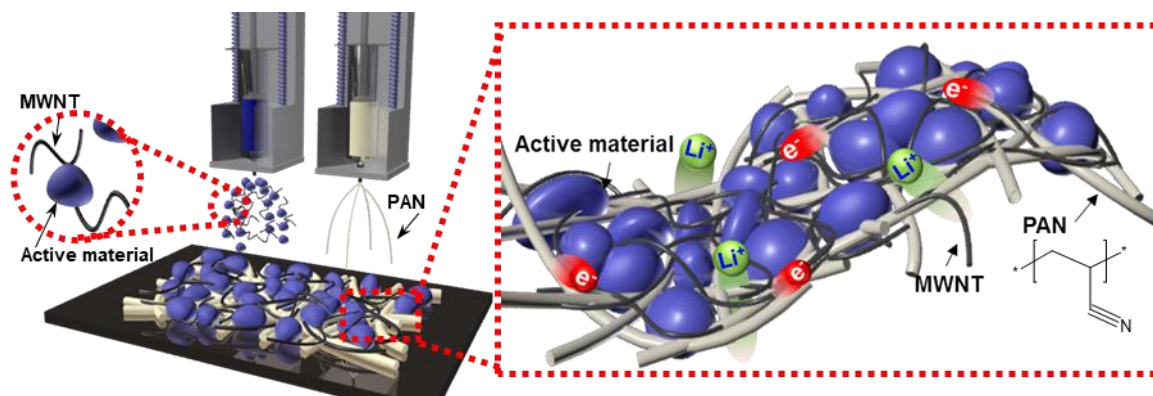


**Figure 2.5** Schematic illustration depicting the manufacturing procedure of HM cathodes through simultaneous electrospinning/electrospraying process. Structural/physicochemical characterization of HM cathodes.

The top-viewed and cross-sectional SEM images (Figure 2.7a and 2.7b) show that the OLO nanoparticles are densely packed in the electrospun PAN nanofibers/electrosprayed MWCNTs-intermingled heteronanomat. Such compact packing of the OLO active materials is a distinctive difference compared to the morphologies of the previously reported binder-/conductive powder-/current collector-free electrodes<sup>[8,15,23,24]</sup> (most of them had difficulty achieving high active-mass loading), which consequently plays an important role in realizing high-capacity cathodes. More details will be

discussed in the next section. Notably, metallic foil current collectors, carbon powder conductive additives and polymer binders such as PVdF, all of which are indispensably used for conventional cathodes, were not found in the HM OLO cathode. For comparative analysis, a control OLO cathode (nano OLO/PVdF binder/carbon black additive = 80/10/10 (w/w/w) on an aluminum (Al) foil current collector) was prepared (Figure 2.7c).

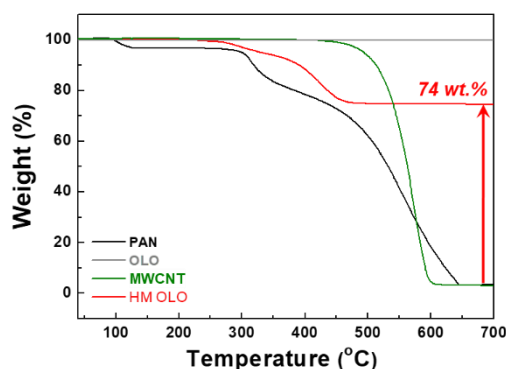


**Figure 2.6** TGA profiles used for estimating composition ratio of HM OLO cathode.

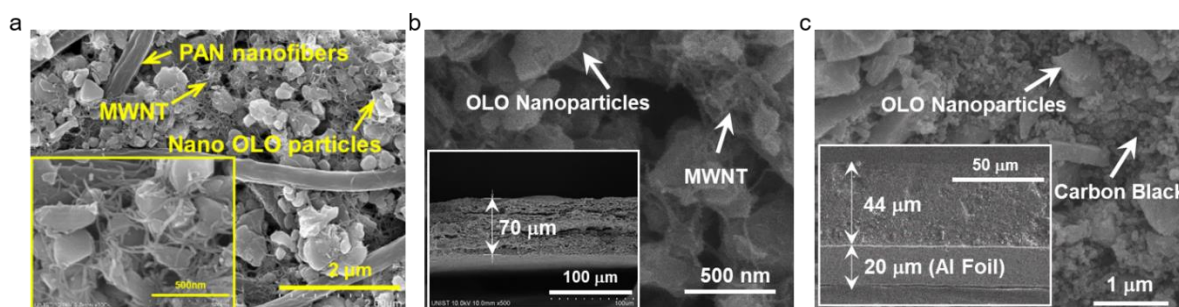


**Figure 2.7** SEM image (surface view) of (a) HM OLO cathode and cross-sectional SEM images (focusing on cathode thickness) of: (b) HM OLO cathode and (c) control OLO one.

The presence of MWCNTs in the HM OLO cathode was further verified with the Raman spectra (Figure 2.8). It is apparent that D and G bands corresponding to MWCNTs<sup>[25]</sup> were respectively observed at 1345 and 1586  $\text{cm}^{-1}$ , along with the characteristic peaks (438, 499, 612  $\text{cm}^{-1}$ ) assigned to  $\text{Li}_2\text{MnO}_3$  phase<sup>[26]</sup> of OLO powders. Figure 2.9a shows that the HM OLO cathode presents the higher electronic conductivity ( $= 3.0 \text{ S cm}^{-1}$ ) than the control OLO cathode ( $= 0.6 \text{ S cm}^{-1}$ ). This is attributed to the well-interconnected MWCNT electronic networks and the removal of PVdF binders (that could partially shield OLO powders and conductive pathways). Meanwhile, the spatially-reticulated interstitial voids (to be filled with liquid electrolytes) and also the elimination of PVdF binders/carbon black powders allow the higher porosity (59 % for HM OLO cathode vs. 24 % for control OLO cathode). The

interstitial voids-based porous channels, in combination with the polar PAN nanofibers, facilitate capillary intrusion of liquid electrolyte into the HM OLO cathode (Figure 2.9b). These results demonstrate that the PAN nanofibers/MWCNTs-intermingled heteronanomat constructs the well-developed ion/electron conduction pathway, which is anticipated to eventually boost redox reaction kinetics of the HM OLO cathode.

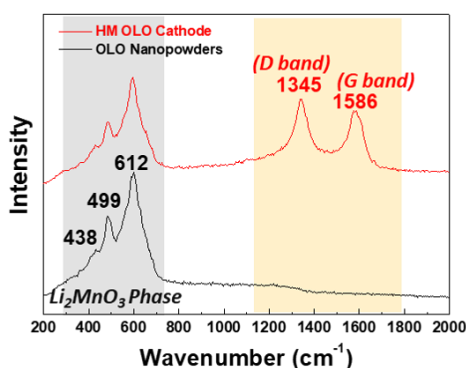


**Figure 2.8** Raman spectra of HM OLO cathode and OLO nanopowders.

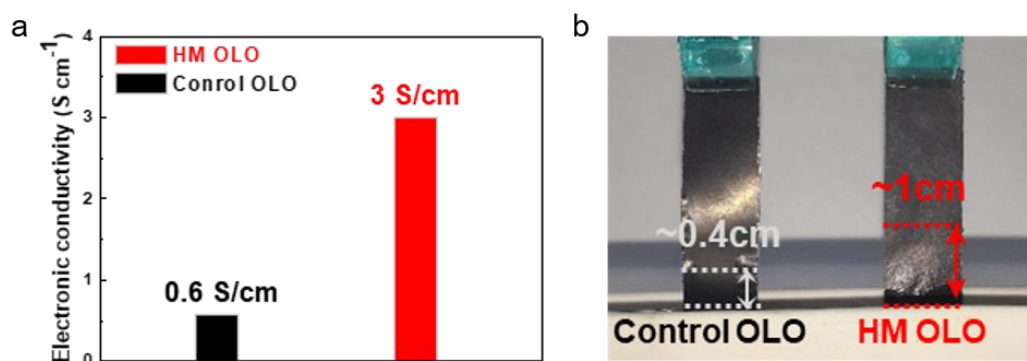


**Figure 2.9** (a) Electronic conductivity of HM OLO cathode and control OLO one. (b) Electrolyte wettability (determined by electrolyte-immersion height) of HM OLO cathode and control OLO one.

One major concern of metallic foil current collector-/polymer binder-free electrodes is the insufficient mechanical flexibility/dimensional robustness upon external deformation.<sup>[7,27]</sup> Figure 2.10a shows that the HM OLO cathode was bendable and also wound along a glass rod (diameter = 5 mm) without mechanical rupture. This excellence in the mechanical flexibility of the HM OLO cathode was further verified by quantitatively measuring the change of its electronic resistance as a function of longitudinal compression cycle (bending radius = 20 mm, deformation rate = 200 mm in<sup>-1</sup>, Figure 2.10b). The electronic resistance of the HM OLO cathode was little changed after 200 bending cycles, whereas the control OLO cathode showed an increase in electronic resistance with bending cycle and, eventually,

was mechanically broken after 95 cycles (inset of Figure 2.10b). Moreover, the unique heteronanomat structure of the HM OLO cathode was not impaired after the bending cycle test (Figure 2.10c). These results underline the mechanical tolerance of the OLO-embedded PAN nanofibers/MWCNTs heteronanomat architecture, even in the absence of PVdF binders and Al foil current collectors.

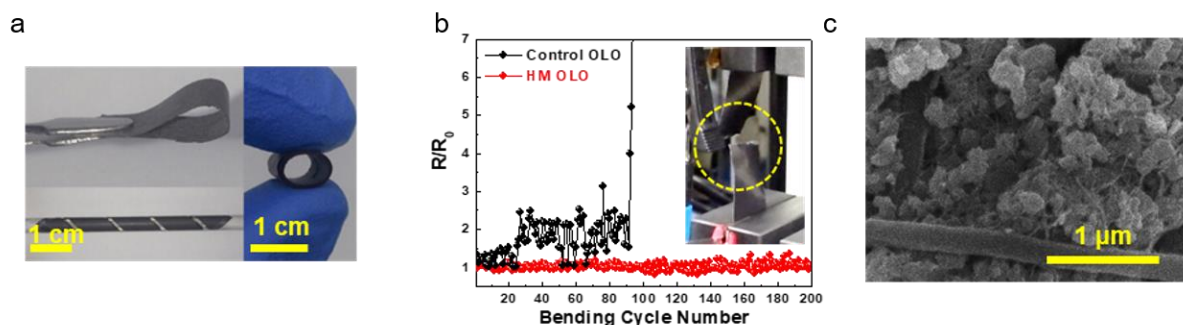


**Figure 2.10** (a) Mechanical flexibility and dimensional integrity of HM OLO cathode. (b) Change in electronic resistance as a function of longitudinal compression cycle (bending radius = 20 mm, deformation rate = 200 mm min<sup>-1</sup>), wherein an inset is a photograph showing the mechanical rupture of control OLO cathode after 95 bending cycles. (c) SEM image (surface view) of HM OLO cathode after the bending cycle test.

### 2.1.3.2 Electrochemical properties of HM OLO cathodes

Based on this comprehensive understanding of the structural and physicochemical properties of the HM OLO cathodes mentioned above, their application to lithium-ion cells was explored using a coin-type half-cell (= OLO cathode/Li metal). The HM OLO cathode showed normal charge/discharge profiles at a current density of 0.1 C/0.1 C under voltage range of 2.0 - 4.7 V (Figure 2.11a). The voltage plateau observed above 4.5 V in the charge profiles indicates the extraction of lithium ions from a Li<sub>2</sub>MnO<sub>3</sub> phase in the HM OLO cathode.<sup>[28]</sup> Intriguingly, the discharge capacity of the HM OLO cathode (= 263 mAh g<sub>OLO</sub><sup>-1</sup>) is larger than that of the control OLO cathode (= 246 mAh g<sub>OLO</sub><sup>-1</sup>) and even slightly surpasses the theoretical value (= 250 mAh g<sub>OLO</sub><sup>-1</sup>). Such an increase in the capacity is believed to arise from non-faradaic reaction of MWCNTs (i.e., adsorption and desorption of ions on MWCNT surface<sup>[29]</sup>) in the HM OLO cathode. To prove this MWCNTs-driven additional capacity gain, a model electrode composed of MWCNTs (without OLO powders) and PAN nanofibers were prepared using the simultaneous electrospinning/electrospraying process. The galvanostatic charge/discharge curves (Figure 2.11b) reveal that the MWCNTs undergo the non-Faradaic electrochemical reaction, thus yielding appreciable level of discharge capacity (= 22 mAh g<sub>MWCNT</sub><sup>-1</sup>). The similar results previously reported that the engagement of CNTs in the electrochemical reaction is allowed only if CNTs are sufficiently wetted with liquid electrolyte.<sup>[30]</sup> Therefore, the additional capacity originating from the

MWCNTs is an indirect evidence to prove facile electrolyte accessibility of the HM OLO cathode.

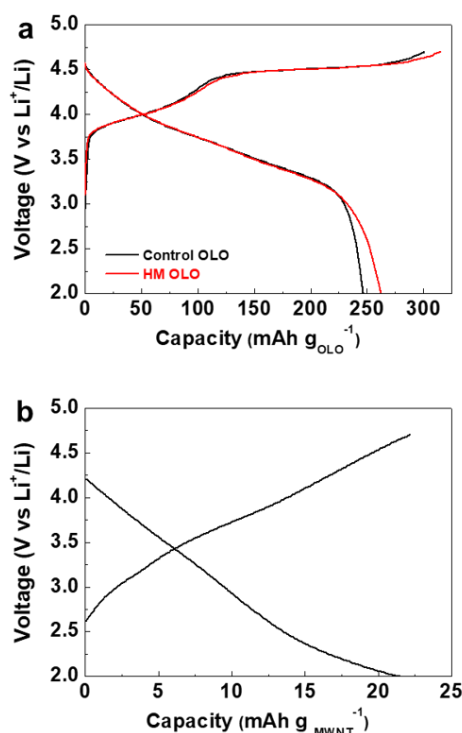


**Figure 2.11** (a) Comparison in discharge capacity (normalized by OLO mass) between HM OLO cathode and control OLO one at current density of 0.1 C/0.1 C under voltage range of 2.0 - 4.7 V. (b) Charge/discharge profile of a model electrode (MWCNTs/PAN nanofibers without OLO powders).

It is again underlined that the HM OLO cathode does not contain electrochemically-inert/heavy Al foil current collectors, thus enabling the larger mass loading of electrode active materials. Figure 12a shows that, owing to the removal of Al foil current collector, the total areal weight of the HM OLO cathode was reduced compared to that of the control OLO cathode, wherein the areal active-mass loading (calculated exclusively by the weight of OLO active powders) is similar between the HM OLO cathode and control OLO one. As a consequence, the HM OLO cathode allows a significant increase in the specific gravimetric capacity (= capacity per cathode weight (mAh g<sub>cathode</sub><sup>-1</sup>), Figure 2.12b).

OLO active materials are known to suffer from their low electronic conductivity,<sup>[31,32]</sup> which is one of the formidable obstacles impeding their application to lithium-ion battery cathodes. Figure 12b also shows that, at a higher charge/discharge current density (= 5.0 C/5.0 C), the advantageous effect of the HM OLO cathode on the capacity and the cell polarization was more pronounced. This result demonstrates that the PAN nanofibers/MWCNTs-intermingled heteronanomat (enabling the 3D bicontinuous ion/electron transport pathways) of the HM OLO cathode could be suggested as a promising solution to address the kinetics-related issue of OLO active materials.

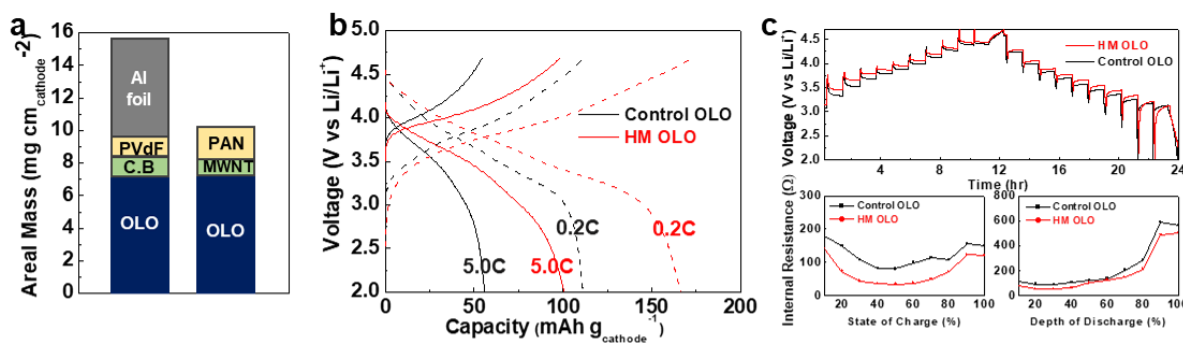


**Figure 2.12** (a) Comparison in total areal weight ( $\text{mg cm}_{\text{cathode}}^{-2}$ ) between HM OLO cathode and control OLO one. (b) Charge/discharge profiles of HM OLO cathode and control OLO one. (c) GITT profiles of cells assembled with HM OLO cathode or control OLO one and variation in internal cell resistance as a function of state of charge and depth of discharge.

To further verify the faster rate performance of the HM OLO cathode, Galvanostatic Intermittent Titration Technique (GITT) analysis<sup>[30,33]</sup> was conducted. Figure 12c shows that the HM OLO cathode effectively mitigates the rise in cell polarization upon the repeated current stimuli (at current density = 1.0 C, interruption time between each pulse = 60 min) during the charge/discharge reaction, wherein the internal cell resistances were summarized as a function of state of charge and depth of discharge. In addition, overpotential distribution of the HM OLO cathode in the through-thickness direction was investigated using a kind of *in-situ* electrochemical impedance spectroscopy (EIS) measurement. For this analysis, an elaborately-designed pouch cell (Figure 2.13a) was prepared based on the previous study<sup>[34]</sup>, wherein Al taps were attached on both top and bottom of a target cathode (= working electrode) and a lithium metal disc was used as a counter/reference electrode. During the galvanostatic discharging at a current density of 1.0 C, the voltage variation at both sides was monitored as a function of redox reaction time. At the discharge voltage of 3.8 V (measured from the bottom side), the HM OLO cathode showed the smaller voltage difference between the top and bottom side (Figure 2.13b), as compared to the control OLO cathode (Figure 2.13c). Such uniform voltage distribution in the through-thickness direction becomes more noticeable at the higher discharge current density of 5.0 C (Figure 2.13d and 2.13e). This result indicates that the cell polarization of the HM OLO cathode was effectively alleviated due to the heteronanomat-enabled 3D bicontinuous electron/ion conduction pathways. A comparison with the control OLO cathode showing the sluggish/nonuniform electron/ion conduction behavior was conceptually illustrated in the inset images of Figure 2.13b and 2.13c.

The architectural excellence (in terms of ion/electron transport phenomena) of the HM OLO cathode allowed significant improvement in the cycling performance at fast charge/discharge current density = 5.0 C/5.0 C (Figure 2.14a and 2.14b). The HM OLO cathode showed the stable charge/discharge

profiles with cycling (capacity retention after 200 cycles = 67 %), while the control OLO cathode presented a sharp decay in capacity retention (= 34 %) and also large cell polarization. This superior cycling performance was verified by conducting a postmortem analysis of the cathode surface after the cycling test. The time-of-flight secondary ion mass spectroscopy (TOF-SIMS) images (Figure 2.14c) show that LiF, one of the byproducts generated from electrochemical decomposition of LiPF<sub>6</sub> salts in liquid electrolytes,<sup>[35,36]</sup> was sparsely dispersed over wide area and also its absolute amount was lower at the HM OLO cathode, as compared to the control OLO cathode. In addition, for the HM OLO cathode, neither appreciable cracks nor morphological disruptions were found after 200 cycles (Figure 2.14d), demonstrating its structural/electrochemical tolerance to the repeated charge/discharge reaction.

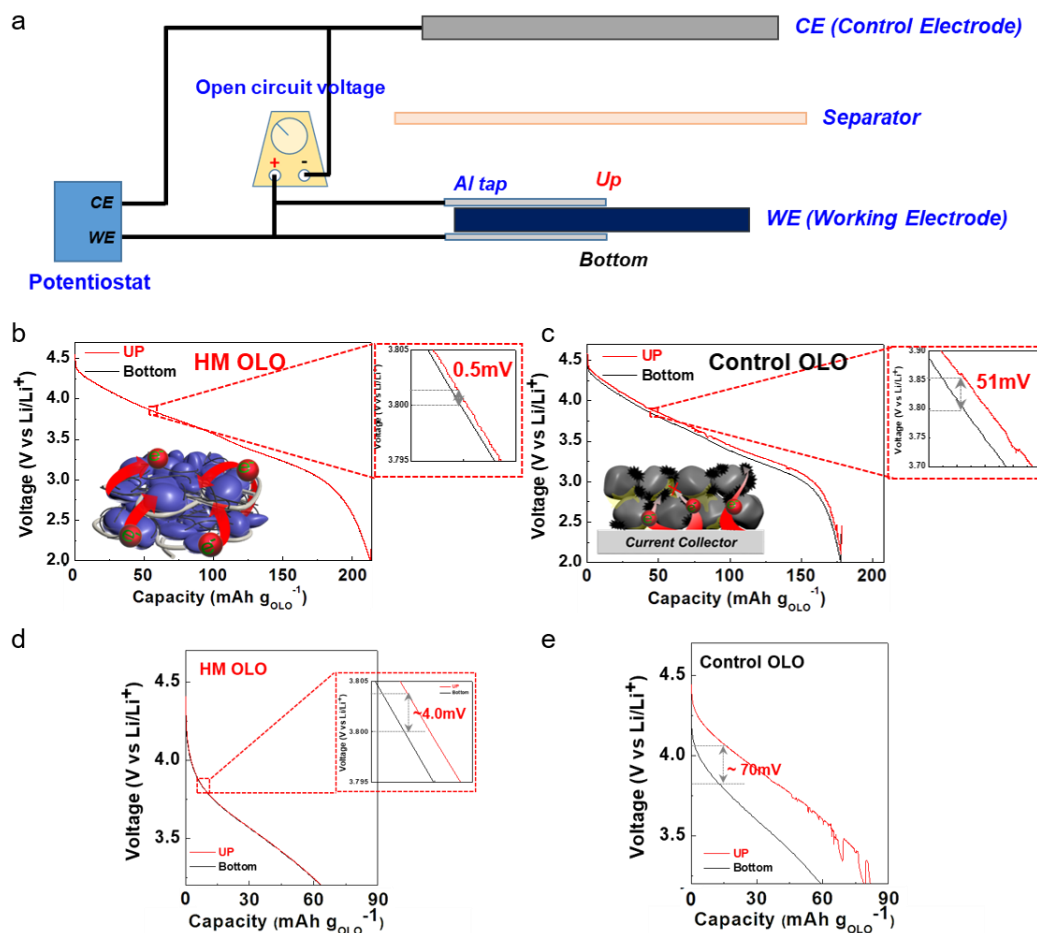


**Figure 2.13** (a) Schematic representation depicting a pouch cell designed for *in-situ* EIS measurement of thickness-directional overpotential distribution (i.e., voltage difference between top and bottom side) of cathodes. Overpotential distribution of the cathodes in the through-thickness direction (i.e., voltage difference between the top and bottom side of cathodes) at current density of 1.0 C/1.0 C and 5.0C/5.0C, wherein inset images illustrate electronic/ionic transport phenomena of the cathodes: (b) HM OLO cathode; (c) control OLO cathode at 1.0C/1.0C, (d) HM OLO cathode; (e) control OLO cathode at 5.0C/5.0C.

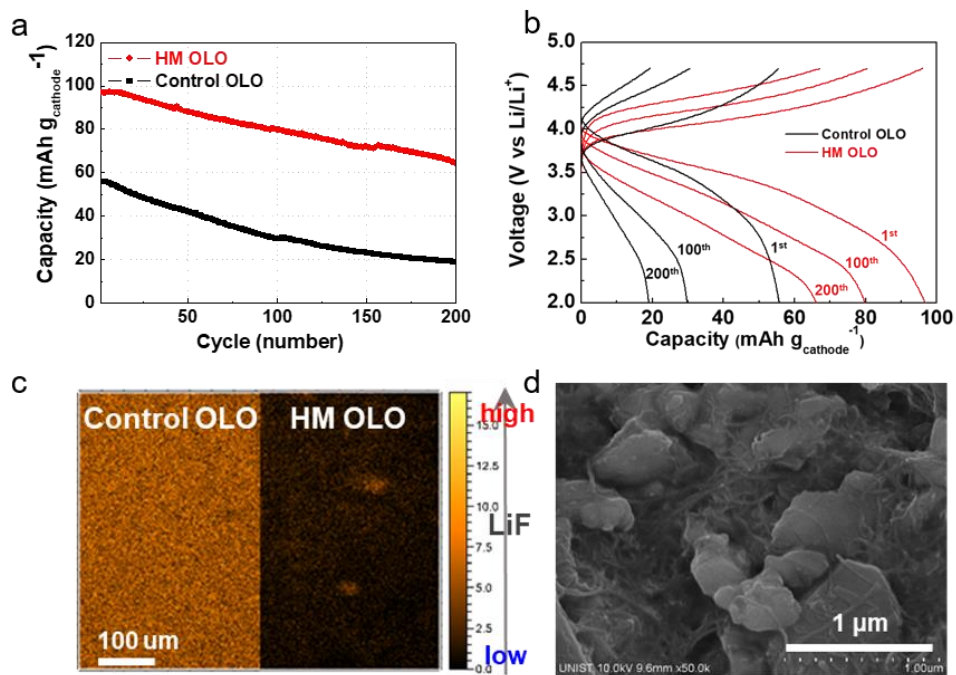


**Figure 2.14** (a) Comparison in cycling performance (at charge/discharge current density of 5.0 C/5.0 C under voltage range of 2.0 - 4.7 V) between HM OLO cathode and control OLO one. (b) Charge/discharge profiles with cycling (up to 200 cycles) of half cells assembled with HM OLO cathode or control OLO one. (c) TOF-SIMS images of LiF byproduct on cathode surface after 200 cycles. (d) SEM image of HM OLO cathode after 200 cycles.

### 2.1.3.3 Ultrathick HM OLO cathodes for high capacity

The heteronanomat-driven structural uniqueness of the HM OLO cathode is expected to provide a new opportunity for developing ultrathick (i.e., extreme high-mass loading) cathodes that lie far beyond those achievable with conventional electrode technology. The removal of Al foil current collectors could allow facile fabrication of user-tailored, multiple-stacked HM OLO cathodes in series, which is schematically represented in Figure 2.15a. Zhang et. al.<sup>[37]</sup> reported a similar electrode concept, however, different from the OLO-embedded PAN nanofibers/MWCNTs heteronanomat presented herein, sulfur electrodes consisting of sulfur-loaded MWCNTs and vertically-aligned CNTs were stacked layer-by-layer. Figure 2.15b shows that a diversity of HM OLO cathodes in thickness were fabricated by simply varying the number of cathode sheets (70  $\mu\text{m}$  (= 1 sheet), 230  $\mu\text{m}$  (= 4 sheets), 450  $\mu\text{m}$  (= 8 sheets)). The elementary cathode sheets were stacked in series and then subjected to roll pressing in order to secure the tightly-interlocked interface between the adjacent cathode sheets. It is of note that, even at

the larger cathode thickness of 450  $\mu\text{m}$ , the heteronanomat architecture was well preserved in the through-thickness direction. By comparison, the control OLO cathode failed to reach the thickness above 400  $\mu\text{m}$  (Figure 2.16). The slightly smaller thickness of the multi-stacked cathodes, with respect to the theoretical thickness simply calculated from the stacked number of the cathode sheets, is due to the thickness-directional compression during the roll pressing.

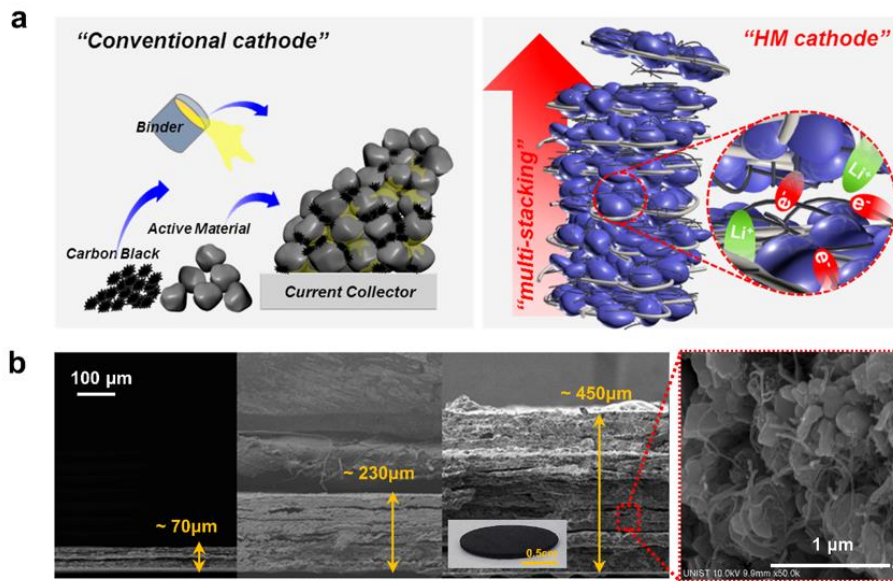


**Figure 2.15** (a) Conceptual illustration depicting facile fabrication of user-tailored, multi-stacked HM OLO cathodes in series. (b) SEM images (cross-sectional view) of multi-stacked HM OLO cathodes with various thickness (70  $\mu\text{m}$  (= 1 sheet), 230  $\mu\text{m}$  (= 4 sheets), 450  $\mu\text{m}$  (= 8 sheets)).

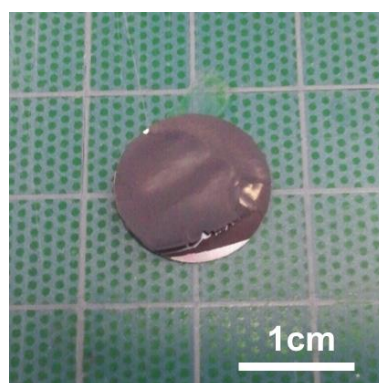


**Figure 2.16** A photograph showing the poor structural stability of control OLO cathode (thickness ~ 400  $\mu\text{m}$ ).

The multi-stacked HM OLO cathodes brought unprecedented improvement in their areal capacity. In proportion to the thickness of the HM OLO cathodes, the discharge capacities per cathode area (mAh

$\text{cm}_{\text{cathode}}^{-2}$ ) tend to increase (Figure 2.17a). At charge/discharge current density of 0.1 C/0.1 C, the areal capacity of 450  $\mu\text{m}$  (= 8 sheets) HM OLO cathode was 13.0  $\text{mAh cm}_{\text{cathode}}^{-2}$ , which is a remarkably high value that corresponds to stripping/plating of a lithium metal layer with thickness 65  $\mu\text{m}$ <sup>[38]</sup>. The cycling performance of the multi-stacked HM OLO cathodes was examined at charge/discharge current density of 0.5 C/0.5 C under voltage range of 2.0 - 4.7 V (Figure 2.17b). The 4 and 8 sheets-stacked HM OLO cathodes as well as the 1 sheet HM OLO cathode showed stable charge/discharge profiles with cycling (Figure 2.17c and 2.17d). The SEM image (inset of Figure 2.17d) exhibits that the heteronanomaterial structure of the 8 sheets-stacked ultrathick HM OLO cathode was well preserved after 30 cycles, indicating its structural/electrochemical durability with cycling.

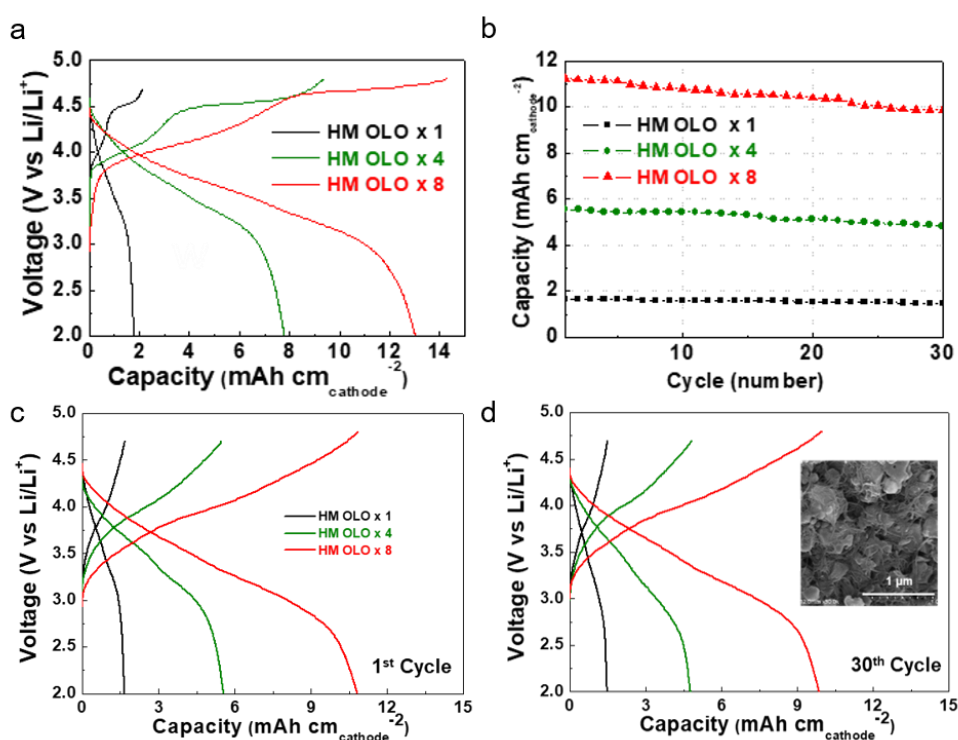


**Figure 2.17** (a) Charge/discharge capacities per cathode area ( $\text{mAh cm}_{\text{cathode}}^{-2}$ ) of multi-stacked HM OLO cathodes. (b) Cycling performance (expressed as  $\text{mAh cm}_{\text{cathode}}^{-2}$ ) of multi-stacked HM OLO cathodes as a function of cathode thickness. Charge/discharge profiles with cycling of multi-stacked HM OLO cathodes as a function of cathode thickness: (c) after 1 cycle; (d) after 30 cycles (inset: SEM image (surface view) of 8 sheets-stacked HM OLO cathode after the cycling test).

#### 2.1.3.4 Physicochemical and electrochemical properties of HM LNMO cathodes

Another noteworthy advantage of the HM cathode concept is the versatility in the adoption of cathode active materials. In pursuit of high energy density (= capacity  $\times$  voltage) cathodes, high-voltage spinel

LNMO active materials, in addition to the above-mentioned OLO powders, have garnered a great deal of attention due to their exceptional high working voltage.<sup>[17,39]</sup> By exploiting the approach used for the HM OLO cathodes, LNMO particles (average diameter = 14  $\mu\text{m}$ , Figure 2.18a) were down-sized to nanopowders (Figure 2.18b). The XRD pattern (Figure 2.18c) shows no appreciable difference in the spinel crystalline structure<sup>[40]</sup> between the micro and nano LNMO powders.

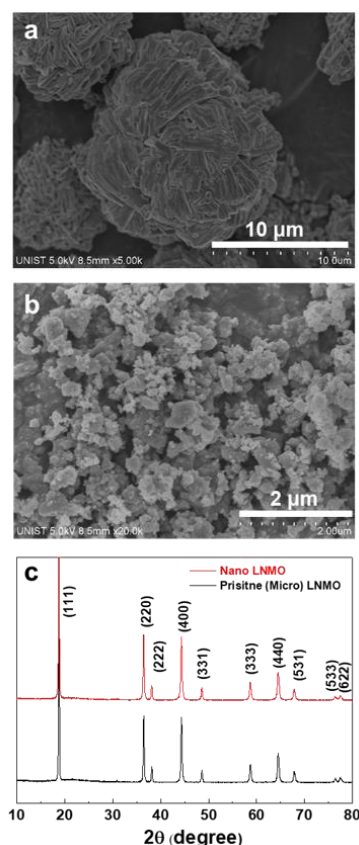


**Figure 2.18** (a) SEM image of pristine (= microsized) LNMO particles. (b) SEM image of nanosized LNMO particles. (c) Comparison in XRD patterns between pristine (= microsized) LNMO particles and nanosized LNMO ones.

The HM LNMO cathodes were fabricated through the same manufacturing procedure (i.e., simultaneous electrospinning/electrospinning) used for the HM OLO cathodes. The LNMO nanoparticles are compactly packed in the PAN nanofibers/MWCNTs-intermingled heteronanomat (Figure 2.19a). From the TGA results (Figure 2.19b), the composition ratio of the HM LNMO cathode was observed to be (LNMO/MWCNT)/PAN = (72.0/3.6)/24.4(w/w/w). Even without the incorporation of Al foil current collectors and PVdF binders, the structural integrity of the HM LNMO cathode was not impaired upon exposure to bending and winding deformation (Figure 2.20). The heteronanomat-driven increase in the electronic conductivity was observed at the HM LNMO cathode (= 4.3 S  $\text{cm}^{-1}$ ,

Figure 2.21), which was significantly higher than that ( $= 0.7 \text{ S cm}^{-1}$ ) of the control LNMO cathode (nano LNMO/PVDF binder/carbon black additive = 80/10/10 (w/w/w) on an Al foil current collector).

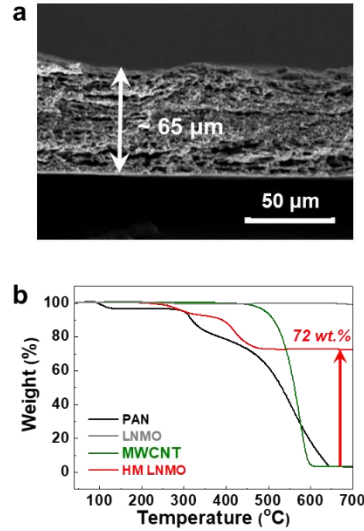


**Figure 2.19** (a) SEM image (cross-sectional view) of HM LNMO cathode. (b) TGA profiles used for estimating composition ratio of HM LNMO cathode.

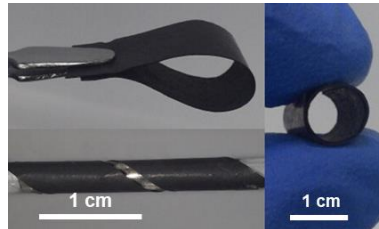


**Figure 2.20** Mechanical flexibility and dimensional integrity of HM LNMO cathode.

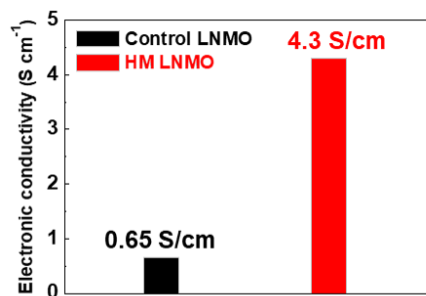


**Figure 2.21** Electronic conductivities of HM LNMO cathode and control LNMO one.

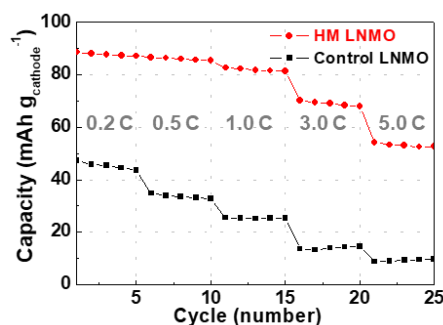


**Figure 2.22** Discharge rate capability over a wide range of discharge current densities (= 0.2 - 5.0 C) at a fixed charge current density of 0.2 C.

The HM LNMO cathode showed the improvement in the areal capacity and also rate capability (Figure 22). Moreover, the HM LNMO cathodes were multi-stacked in series (65  $\mu\text{m}$  (= 1 sheet), 220  $\mu\text{m}$  (= 4 sheets), 420  $\mu\text{m}$  (= 8 sheets), Figure 2.23a), thus contributing to the areal capacity (= capacity per cathode area) is proportional to their thickness (Figure 2.23b). The cycling performance of the 8 sheets-stacked HM LNMO cathode was examined using a half cell (HM LNMO cathode/Li metal anode), where the cell was cycled at charge/discharge current density of 0.2 C/0.2 C under voltage range of 3.50 - 4.95 V. Even at such harsh operating condition (i.e., ultrathick (= 420  $\mu\text{m}$ ) cathode and high charging voltage (= 4.95 V)), the HM LNMO cathode showed good cycling performance (capacity retention after 30 cycles = 78.5 %, Figure 2.23c), although its capacity retention was slightly lower than that of thinner HM LNMO cathodes. Future works will be devoted to further improving the capacity retention with cycling. Meanwhile, PAN is known to be electrochemically vulnerable particularly upon exposure to high voltage conditions,<sup>[21,22]</sup> however, the thermal treatment (120  $^{\circ}\text{C}/12\text{ h}$   $\rightarrow$  150  $^{\circ}\text{C}/2\text{ h}$  in a vacuum oven) performed during the HM cathode fabrication contributed to widening electrochemical stability window of PAN nanofibers (Figure 2.24). As a consequence, PAN-triggered harmful side effects on high-voltage cycling performance were not observed at the HM LNMO cathode.

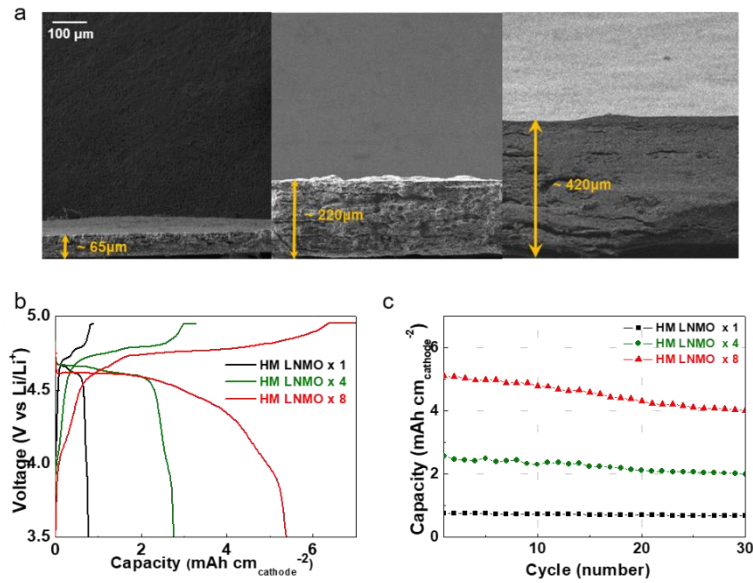


**Figure 2.23** (a) Charge/discharge profiles of cells assembled with HM LNMO cathode or control LNMO one. (b) Charge/discharge capacities per cathode area ( $\text{mAh cm}_{\text{cathode}}^{-2}$ ) of multi-stacked HM LNMO cathodes. (c) Cycling performance (expressed as  $\text{mAh cm}_{\text{cathode}}^{-2}$ ) of multi-stacked HM LNMO cathodes.

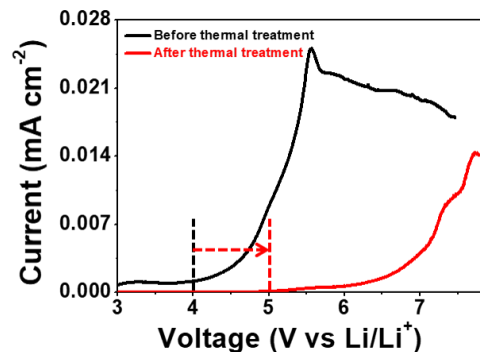


**Figure 2.24** Change in electrochemical stability window of PAN nanofibers after thermal treatment ( $120\text{ }^\circ\text{C}/12\text{ h} \rightarrow 150\text{ }^\circ\text{C}/2\text{ h}$  in a vacuum oven).

#### 2.1.4 Conclusion

In summary, we presented the cathode active particles-embedded PAN nanofibers/MWCNTs heteronanomat cathode (HM cathode) as a new concept of electrode platform to overcome the long-standing challenges (in particular, mechanical flexibility and capacity issues) of conventional cathodes. The HM cathode was fabricated via the simultaneous electrospinning (for MWCNTs/OLO (or LNMO) mixtures) and electrospinning process (for PAN nanofibers) without the use of Al foil current

collectors/carbon powder additives/PVDF binders. Such material/structure uniqueness of the HM cathode significantly improved the mechanical flexibility/dimensional tolerance and, most notably, enabled the formation of 3D bicontinuous MWCNT electron networks/interstitial void channels (ensuring electrolyte accessibility) in the presence of densely-packed cathode active powders. This facile electron/ion transport of the HM cathodes boosted up the redox reaction kinetics, leading to the superior rate capability and cycling performance. Furthermore, the Al foil current collector-free, PAN/MWCNT heteronanomat allowed the HM cathodes to be multiple-stacked in series, which eventually produced the user-tailored, ultrathick cathodes (i.e., extremely high areal capacity: 13.0 mAh  $\text{cm}_{\text{cathode}}^{-2}$  for HM OLO cathode & 5.4 mAh  $\text{cm}_{\text{cathode}}^{-2}$  for HM LNMO cathode) that lie far beyond those accessible with conventional cathode technologies. We envision that the 1D nanobuilding blocks-mediated heteronanomat cathode strategy presented herein holds a great deal of promise as an effective and versatile platform technology to open a new route toward high-performance ultrahigh-capacity cathodes in urgent need for forthcoming smart power sources.

#### 2.1.5 Reference

1. X. Fang, M. Ge, J. Rong, C. Zhou, *ACS Nano* **2014**, 8, 4876.
2. Y. Cheng, Z. Chen, M. Zhu, Y. Lu, *Adv. Energy Mater.* **2015**, 5, 1401207.
3. X. Jia, Y. Kan, X. Zhu, G. Ning, Y. Lu, F. Wei, *Nano Energy* **2014**, 10, 344.
4. X. Jia, Z. Chen, X. Cui, Y. Peng, X. Wang, G. Wang, F. Wei, Y. Lu, *ACS Nano* **2012**, 6, 9911.
5. X. Fang, C. Shen, M. Ge, J. Rong, Y. Liu, A. Zhang, F. Wei, C. Zhou, *Nano Energy* **2015**, 12, 43.
6. Z. Chen, J. W. F. To, C. Wang, Z. Lu, N. Liu, A. Chortos, L. Pan, F. Wei, Y. Cui, Z. Bao, *Adv. Energy Mater.* **2014**, 4, 1400207.
7. Z. Chen, Y. Yuan, H. Zhou, X. Wang, Z. Gan, F. Wang, Y. Lu, *Adv. Mater.* **2014**, 26, 339.
8. J. Luo, J. Liu, Z. Zeng, C. F. Ng, L. Ma, H. Zhang, J. Lin, Z. Shen, H. J. Fan, *Nano Lett.* **2013**, 13, 6136.
9. L. Shen, B. Ding, P. Nie, G. Cao, X. Zhang, *Adv. Energy Mater.* **2013**, 3, 1484.
10. X. Fang, M. Ge, J. Rong, C. Zhou, *ACS Nano* **2014**, 8, 4876.
11. Y. Cheng, Z. Chen, M. Zhu, Y. Lu, *Adv. Energy Mater.* **2015**, 5, 141207.-
12. X. Jia, Y. Cheng, Y. Lu, F. Wei, *ACS Nano* **2014**, 8, 9265.
13. L. Shen, B. Ding, P. Nie, G. Cao, X. Zhang, *Adv. Energy Mater.* **2013**, 3, 1484.
14. H. Yu, C. Zhu, K. Zhang, Y. Chen, C. Li, P. Gao, P. Yang, Q. Ouyang, *J. Mater. Chem. A* **2014**, 2, 4551.
15. B. Liu, J. Zhang, X. Wang, G. Chen, D. Chen, C. Zhou, G. Shen, *Nano Lett.* **2012**, 12, 3005.
16. T.-H. Kim, J.-S. Park, S. K. Chang, S. Choi, J. H. Ryu, H.-K. Song, *Adv. Energy Mater.* **2012**, 2, 860

17. K. Zhang, X. Han, Z. Hu, X. Zhang, Z. Tao, J. Chen, *Chem. Soc. Rev.* **2015**, 44, 699
18. W.-H. Ryu, D.-H. Kim, S.-H. Kang, H.-S. Kwon, *RSC Adv.* **2013**, 3, 8527.
19. L. Zhang, N. Li, B. Wu, H. Xu, L. Wang, X.-Q. Yang, F. Wu *Nano Lett.* **2015**, 15, 656.
20. T. Hasan, V. Scardaci, P. Tan, A. G. Rozhin, W. I. Milne, A. C. Ferrari, *J. Phys. Chem. C* **2007**, 111, 12594.
21. A. Gupta, R. Singhal, V. Agarwal, *J. Appl. Polym. Sci.* **1981**, 26, 3599.
22. A. Gupta, A. Maiti, *J. Appl. Polym. Sci.* **1982**, 27, 2409.
23. Y. Xu, Y. Zhu, F. Han, C. Luo, C. Wang, *Adv. Energy Mater.* **2015**, 5, 1400753.
24. D. Chao, X. Xia, J. Liu, Z. Fan, C. F. Ng, J. Lin, H. Zhang, Z. X. Shen, H. J. Fan, *Adv. Mater.* **2014**, 26, 5794.
25. J. H. Lehman, M. Terrones, E. Mansfield, K. E. Hurst, V. Meunier, *Carbon* **2011**, 49, 2581.
26. Z. Li, F. Du, X. Bie, D. Zhang, Y. Cai, X. Cui, C. Wang, G. Chen, Y. Wei, *J. Phys. Chem. C* **2010**, 114, 22751.
27. Z. Cao, B. Wei, *ACS Nano* **2014**, 8, 3049.
28. J. Zheng, M. Gu, J. Xiao, P. Zuo, C. Wang, J. G. Zhang, *Nano Lett.* **2013**, 13, 3824.
29. S. W. Lee, B. M. Gallant, Y. Lee, N. Yoshida, D. Y. Kim, Y. Yamada, S. Noda, A. Yamada, Y. Shao-Horn, *Energy Environ. Sci.* **2012**, 5, 5437.
30. K.-H. Choi, S.-J. Cho, S.-J. Chun, J. T. Yoo, C. K. Lee, W. Kim, Q. Wu, S.-B. Park, D.-H. Choi, S.-Y. Lee, *Nano Lett.* **2014**, 14, 5677.
31. J. Zhao, R. Huang, W. Gao, J.-M. Zuo, X. F. Zhang, S. T. Mixture, Y. Chen, J. V. Lockard, B. Zhang, S. Guo, M. R. Khoshi, K. Dooley, H. He, Y. Wang, *Adv. Energy Mater.* **2015**, 5, 1401937.
32. P. Oh, M. Ko, S. Myeong, Y. Kim, J. Cho, *Adv. Energy Mater.* **2014**, 4, 1400631.
33. J.-H. Kim, J.-H. Kim, K.-H. Choi, H. K. Yu, J. H. Kim, J. S. Lee, S.-Y. Lee, *Nano Lett.* **2014**, 14, 4438.
34. S. Klink, W. Schuhmann, F. La Mantia, *ChemSusChem* **2014**, 7, 2159.
35. S. Lux, I. Lucas, E. Pollak, S. Passerini, M. Winter, R. Kostecki, *Electrochem. Commun.* **2012**, 14, 47.
36. J.-M. Kim, J.-H. Park, C. K. Lee, S.-Y. Lee, *Sci. Rep.* **2014**, 4, 4602.
37. Z. Yuan, H.-J. Peng, J.-Q. Huang, X.-Y. Liu, D.-W. Wang, X.-B. Cheng, Q. Zhang, *Adv. Funct. Mater.* **2014**, 24, 6105.
38. M. S. Park, S. B. Ma, D. J. Lee, D. Im, S.-G. Doo, O. Yamamoto, *Sci. Rep.* **2014**, 4, 3815.
39. L. Zhou, D. Zhao, X. D. Lou, *Angew. Chem.* **2012**, 124, 243.
40. S.-H. Park, Y.-K. Sun, *Electrochim. Acta* **2004**, 50, 439.

\* Chapter 2.1 is reproduced in with a permission of “Ju-Myung Kim, Chang-Hoon Park, Qinglin Wu,

Sang-Young Lee, 1D Building Blocks-Intermingled Heteronanomats as a Platform Architecture for High-Performance Ultrahigh-Capacity Lithium-Ion Battery Cathodes *Adv. Energy Mater.* 6, 1501594 (2016)". Copyright © 2016 John Wiley & Sons, Inc.

## 2.2 All-nanomat lithium-ion batteries: A new cell architecture platform for both ultrahigh energy density and mechanical flexibility

### 2.2.1 Introduction

The forthcoming ubiquitous electronics era, which will involve the widespread use of flexible electronic devices, Internet of Things (IoT) and electric vehicles (EVs), is in urgent need of advanced rechargeable power sources (e.g., lithium-ion batteries (LIBs)) that afford reliable/sustainable electrochemical performance and mechanical flexibility.<sup>[1-3]</sup>

From the electrode structure perspective, conventional electrode sheets consist of a random pile-up of electrode active materials, carbon powder conductive additives, and polymer binders on top of metallic foil current collectors. This monotonous electrode architecture often gives rise to non-uniform and sluggish ion/electron transport in the through-thickness direction and also dimensional disruption upon mechanical deformation.<sup>[4,5]</sup>

Moreover, the presence of electrochemically inert materials such as metallic foil current collectors, conductive carbon additives and binders, which account for a significant portion of the electrode mass, results in the inevitable loss of the areal capacity of the electrodes.<sup>[6]</sup>

Several approaches have sought to make electrodes free of electrochemically inert materials,<sup>[7-10]</sup> which include self-standing sheets based on electrode materials/carbon substances (e.g., carbon nanofibers, carbon nanotubes (CNTs), and graphenes) and conductive porous scaffolds impregnated with electrode materials. However, the majority of these studies have shown limitations in simultaneously achieving electrochemical performance, mass loading of electrode materials, mechanical flexibility, and manufacturing processability.

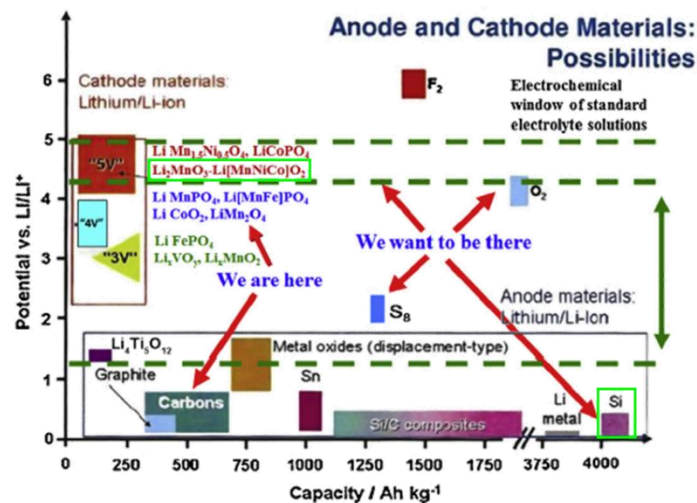


**Figure 2.25** The roadmap for Li battery technology (D. Aurbach et al. Materials Today, 2014, 17, 110)

Among the numerous electrode active materials, silicon (Si, for anode) and over-lithiated layered oxide (OLO,  $0.33\text{Li}_2\text{MnO}_3 \cdot 0.67\text{LiNi}_{0.18}\text{Co}_{0.17}\text{Mn}_{0.65}\text{O}_2$ , for cathode) have garnered considerable attention as potential alternatives beyond graphite and  $\text{LiCoO}_2$  that are widely used in commercial LIBs, due to their exceptionally high theoretical capacities ( $4,200 \text{ mAh g}^{-1}$  (Si) and  $250 \text{ mAh g}^{-1}$  (OLO) as shown in Figure 2.25).<sup>[11-14]</sup> This information suggests that the combination of Si anodes and OLO cathodes could be an effective way to enable ultrahigh-capacity LIB full cells. However, the fabrication of (Si anode/OLO cathode) LIB full cells has rarely been reported<sup>[15]</sup> and still remains a formidable challenge, mainly because the problems with Si (volume change during lithiation/delithiation)<sup>[16]</sup> and OLO (poor electronic conductivity and structural degradation with charge/discharge reaction)<sup>[17,18]</sup> have not yet been resolved despite enormous research efforts.

Here, as a simple and versatile cell architecture strategy to address the aforementioned long-standing challenges, we demonstrate a new class of all-nanomaterial (Si anode/ $\text{Al}_2\text{O}_3$  separator/OLO cathode) LIB full cells based on 1D building elements-interweaved heteronanomaterial skeletons, with particular attention to the development of 3D-bicontinuous ion/electron transport pathways and the removal of metallic foil current collectors. The nanomaterial electrodes are fabricated through a one-pot manufacturing process, *i.e.*, concurrent electrospinning (for polymeric nanofibers) and electrospraying (for electrode materials/CNTs).<sup>[19]</sup> As part of our continuing efforts to develop advanced rechargeable power sources beyond current state-of-the-art LIBs, we fabricate all-nanomaterial LIB full cells by assembling nanomaterial Si anodes and OLO cathodes together with  $\text{Al}_2\text{O}_3$  nanoparticles-incorporated nanomaterial separators.

In nanomaterial electrodes, Si (or OLO) powders are densely embedded in spatially interweaved polymeric nanofiber/CNT heteromaterial frameworks, enabling the construction of 3D-bicontinuous ion/electron conduction channels that can facilitate redox reaction kinetics in the electrodes. Moreover, the highly-reticulated CNT electronic networks allow for the elimination of metallic foil current collectors, leading to a significant increase in the areal capacity of the electrodes. The polymeric nanofibers are rationally designed to act as multifunctional 1D-shaped electrode binders that preserve the structural integrity of the electrodes and scavenge metal ions (e.g.,  $\text{Mn}^{2+}$ ) dissolved from OLO cathode materials. In addition to the nanomaterial electrodes, the nanomaterial  $\text{Al}_2\text{O}_3$  separator, which can be proposed as an appealing alternative<sup>[20]</sup> to commercial polyolefin separators in terms of its porous structure, thermal tolerance, and mechanical stability, is fabricated using a concurrent electrospinning (for polymeric nanofibers)/electrospraying (for  $\text{Al}_2\text{O}_3$  nanoparticles) process.

Driven by the aforementioned structural/chemical novelties resulting from the heteronanomaterial skeleton-mediated cell architecture, the all-nanomaterial LIB (*i.e.*, nanomaterial Si anode/nanomaterial  $\text{Al}_2\text{O}_3$  separator/nanomaterial OLO cathode) shows unprecedented improvements in cell performance (notably, cell weight-based energy density =  $479 \text{ Wh kg}_{\text{Cell}}^{-1}$ ) and mechanical deformability which are difficult to attain with conventional LIB technologies, eventually opening up a new route toward the realization of

advanced LIB full cells with ultrahigh energy density and flexibility.

## 2.2.2 Experimental section

### 2.2.2.1 Design and fabrication of nanomat Si anodes

The nanomat Si anodes consisted of sandwich-like trilayers. First, the bottom layer was produced by concurrent electrospinning (for PAN nanofiber) and electrospraying (for single-walled carbon nanotube (SWCNT)) through two different nozzles. Subsequently, the Si active layer was introduced onto the bottom layer using the same concurrent electrospinning (for PAN nanofiber) and electrospraying (for Si nanoparticle/SWCNT/ poly(3,4-ethylene dioxothiophene) polystyrene sulfonate (PEDOT: PSS)). Finally, the top layer, which has the same materials, composition ratio, and thickness as the bottom layer, was fabricated on top of the Si active layer through the same electrospinning and electrospraying process. For the fabrication of the Si active (middle) layer, Si nanoparticles (Alfa Aesar, the average diameter of 100 nm) were mixed with SWCNTs (Tuball) and PEDOT: PSS (Clevios, PH1000) in water/isopropyl alcohol (IPA) (= 90/10 (w/w)) solvent. The concentration of the PEDOT: PSS in the suspension solution was 0.03 wt%. The SWCNTs were purified in advance by refluxing in 3 M nitric acid at 120°C for 16 h. For the top and bottom layers, the SWCNT suspension solution was prepared and PAN powders (Aldrich, the molecular weight of 150,000 g mol<sup>-1</sup>) were dissolved in dimethyl formamide (DMF) at 80°C for 12 h at a PAN concentration of 10 wt%. The detailed processing conditions were 9 kV with a feed rate of 5 μL min<sup>-1</sup> for electrospinning and 15 kV with a feed rate of 120 μL min<sup>-1</sup> for electrospraying. The resultant nanomat Si anode was dried at 150°C for 2 h in a vacuum oven and then roll-pressed at room temperature. Finally, a self-standing and flexible nanomat Si anode was obtained. As a control sample, a conventional Si anode was fabricated by casting a slurry mixture (Si nanoparticles/ polyacrylic acid (PAA)-carboxyl methyl cellulose (CMC) binder/carbon black conductive additive = 70/20/10 (w/w/w) in water) on a Cu foil current collector.

### 2.2.2.2 Fabrication of nanomat OLO cathodes incorporating rambutan-shaped OLO/MWCNT nanocomposite powders

As cathode active materials, 0.33Li<sub>2</sub>MnO<sub>3</sub>•0.67LiNi<sub>0.18</sub>Co<sub>0.17</sub>Mn<sub>0.65</sub>O<sub>2</sub> (OLO, average diameter = 5 μm) powders were chosen. MWCNTs (average length = 1.5 μm, diameter = 9.5 nm) were purchased from NANOCYL (Belgium). The OLO powders were mixed with the MWCNTs in 1 wt% polyvinylpyrrolidone (PVP) (Aldrich, average molecular weight = 55,000 g mol<sup>-1</sup>)-dissolved aqueous solution. Subsequently, the mixture was subjected to ball milling for 0.5 h, eventually yielding

rambutan-shaped OLO/MWCNT nanocomposite (referred to as “R-OM”) powders. The prepared R-OM powders were mixed with MWCNTs in a water/IPA (= 70/30 (w/w)) solvent, in which 0.5 wt% PVP was used as a dispersing additive for MWCNTs. PAN (Aldrich, molecular weight = 150,000 g mol<sup>-1</sup>) and PVP (Aldrich, molecular weight = 1,300,000 g mol<sup>-1</sup>) powders were dissolved in DMF at 80°C for 12 h, where the polymer concentration was 10 wt% and the composition ratio of PAN/PVP = 50/50 (w/w). The PAN/PVP solution and R-OM powder/MWCNT mixture solution were respectively subjected to concurrent electrospinning and electrospaying through two different nozzles, thus yielding the self-standing and flexible nanomat OLO cathode. The detailed processing conditions were 9 kV with a feed rate of 5 μL min<sup>-1</sup> for electrospinning and 15 kV with a feed rate of 70 μL min<sup>-1</sup> for electrospaying. The resultant nanomat OLO cathode was roll-pressed and dried at 120°C/12 h in a vacuum oven. As a control sample, a conventional OLO cathode was fabricated by casting a slurry mixture (OLO powders/PVDF binder/carbon black conductive additive = 80/10/10 (w/w/w) in NMP) on an Al foil current collector.

#### 2.2.2.3 Fabrication of nanomat Al<sub>2</sub>O<sub>3</sub> separator

PAN (Aldrich, molecular weight = 150,000 g mol<sup>-1</sup>) powder was dissolved in DMF at 80°C for 12 h at a polymer concentration of 10 wt%. A 5 wt% Al<sub>2</sub>O<sub>3</sub> solution dissolved in acetone was mixed with an acetone/butanol (= 70/30 (w/w)) solvent. The PAN solution and Al<sub>2</sub>O<sub>3</sub> solution were respectively subjected to concurrent electrospinning and electrospaying through two different nozzles to produce the nanomat Al<sub>2</sub>O<sub>3</sub> separator. The detailed processing conditions were 9 kV with a feed rate of 5 μL min<sup>-1</sup> for electrospinning and 12 kV with a feed rate of 50 μL min<sup>-1</sup> for electrospaying. The resultant nanomat Al<sub>2</sub>O<sub>3</sub> separator was roll-pressed and dried at 60°C/12 h in a vacuum oven.

#### 2.2.2.4 Structural/physicochemical characterization of the nanomat electrodes

The surface and cross-sectional morphologies of the electrodes were investigated using Field emission-scanning electron microscopy (FE-SEM, S-4800, Hitachi) and Energy dispersive spectrometer (EDS, JSM 6400, JEOL). The porous structure of the R-OM powders was further analyzed by Transmission electron microscopy (TEM, JEM-2100F, JEOL). The N<sub>2</sub> adsorption-desorption isotherms and Barrett-Joyner-Halenda (BJH) profiles of the R-OM powders were obtained using an Auto Physisorption Analyzer (ASAP2020 Analysis). The electronic conductivities of the electrodes were measured using a four-point probe technique (CMT-SR1000N, Advanced Instrument Tech). The electrode was placed on a glass substrate, and at least ten different positions were measured to obtain reproducible data. The electronic resistivity was calculated using Equation (1).

$$\Lambda = (1/R) \times (l/A) \quad (1)$$

where  $\Lambda$  is the electronic conductivity ( $S\text{ cm}^{-1}$ ),  $R$  is the resistivity ( $\Omega = 1/S$ ),  $l$  is the distance between the probes (cm), and  $A$  is the unit area ( $\text{cm}^2$ ). The electrolyte wettability of the electrodes was estimated by measuring electrolyte immersion-height. The composition ratios of the nanomat electrodes were estimated from the Thermogravimetric analysis (TGA) measurement (SDT Q600, TA Instruments) at a heating rate of  $5^\circ\text{C min}^{-1}$  under an air atmosphere. Inductively coupled plasma mass spectrometry (ICP-MS, ELAN DRC-II, Perkin Elmer) analysis was conducted to quantitatively analyze the amount of  $\text{Mn}^{2+}$  ions chelated by the PAN/PVP films or deposited on the lithium anode surface.

#### 2.2.2.5 Electrochemical characterization of nanomat electrodes and all-nanomat full cells

The electrochemical performance of the nanomat electrodes was characterized using 2032-type coin cells (= nanomat electrode/ polyethylene (PE) separator (thickness of 20  $\mu\text{m}$ , Toray-tonen)/Li metal). The liquid electrolytes 1.3 M  $\text{LiPF}_6$  in EC/DEC = 3/7 (v/v) with 10 wt% fluoroethylene carbonate (FEC) and 1 M  $\text{LiPF}_6$  in EC/DMC = 1/1 (v/v) were chosen for the nanomat Si anode and nanomat OLO cathode, respectively. The full cells were also assembled using 2032-type coins. Pouch-type cells (width  $\times$  length = 25  $\times$  50 mm/mm) were fabricated to investigate the mechanical flexibility of the full cells. A liquid electrolyte (1.3 M  $\text{LiPF}_6$  in EC/DEC = 3/7 (v/v) with 10 wt% FEC and 1.0 wt% vinylene carbonate (VC)) was used for the full cells. The entire assembly of the cells was performed in an argon-filled glove box. The cell performance was investigated using a cycle tester (PNE Solution) under various charge/discharge conditions. The galvanostatic intermittent titration technique (GITT) profiles and AC impedance of the cells were obtained using a potentiostat/galvanostat (VSP classic, Bio-Logic).

### 2.2.3 Result and discussion

#### 2.2.3.1 Structural uniqueness and electrochemical superiority of nanomat Si anodes

The nanomat Si anode is characterized by sandwich-like trilayers. A schematic representation depicting the stepwise fabrication of the nanomat Si anode is shown in Figure 2.26. First, the bottom layer was produced by concurrent electrospinning (for PAN nanofiber)/electrospraying (for SWCNT) through two different nozzles. Then, the Si active layer was introduced on the bottom layer using the same concurrent electrospinning (for PAN nanofiber)/electrospraying technique (for Si nanoparticle/SWCNT/PEDOT:PSS). Here, Si nanoparticles were used instead of bulk Si powders to minimize the pulverization-triggered side effects.<sup>[21]</sup> Finally, the top layer, which has the same materials, composition ratio and thickness as the bottom layer, was fabricated on top of the Si active layer using the same

electrospinning/electrospraying process, leading to a self-standing and flexible nanomat Si anode (see the photograph in Figure 2.26).

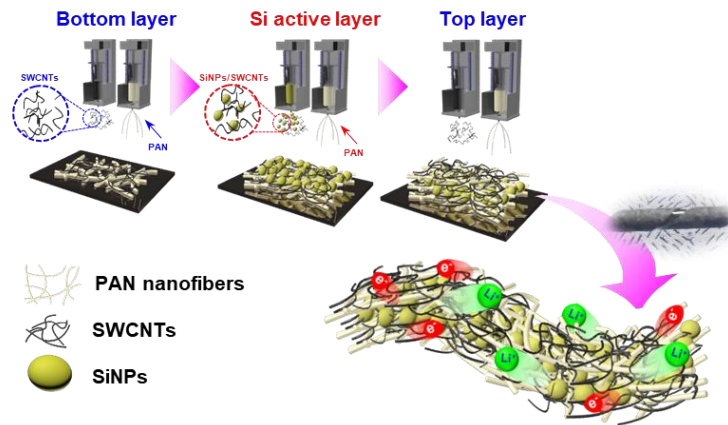


**Figure 2.26** Schematic representation depicting the stepwise preparation process (bottom layer → Si active (middle) layer → top layer) for the nanomat Si anode, along with a photograph. Each layer of the nanomat Si anode was fabricated by concurrent electrospinning and electrospraying through two different nozzles.

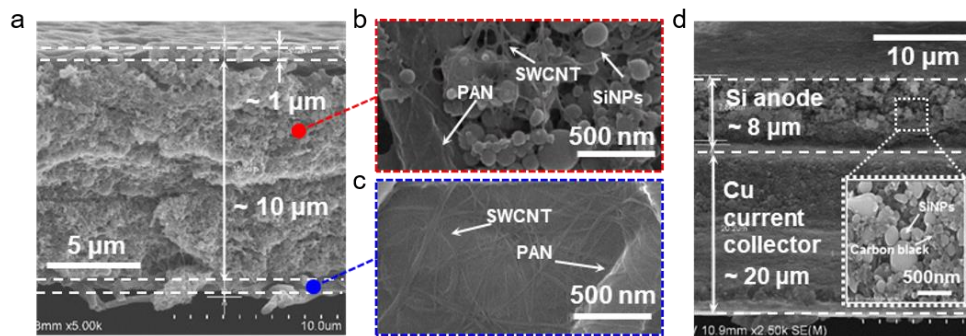


**Figure 2.27** (a) Cross-sectional SEM image of nanomat Si anode (Si active layer ( $\sim 10 \mu\text{m}$ ) sandwiched between thin ( $\sim 1 \mu\text{m}$ ) electroconductive top/bottom layers). (b) SEM image of Si active layer, where the Si nanoparticles were compactly embedded in close contact with the PAN nanofiber/SWCNT-interweaved heteromat. (c) SEM image of SWCNT/PAN-interweaved top and bottom layers. (d) Cross-sectional SEM image of conventional Si anode with a similar Si mass loading. The conventional Si anode consisted of an electrochemically active layer (Si nanoparticles/PAA-CMC binder/carbon black = 70/20/10 (w/w/w), thickness  $\sim 8 \mu\text{m}$ ) on top of a Cu current collector ( $\sim 20 \mu\text{m}$ ).

A cross-sectional scanning electron microscopy (SEM) image (Figure 2.27a) exhibits the formation of sandwich-like trilayers (*i.e.*, the Si active layer (thickness  $\sim 10 \mu\text{m}$ ) sandwiched between the thin ( $\sim 1 \mu\text{m}$ ) electroconductive top/bottom layers) in the nanomat Si anode. Figure 2.27b shows that the Si nanoparticles in the middle layer are compactly embedded in close contact with the PAN

nanofiber/SWCNT-interweaved heteromat skeletons, resulting in the formation of well-interconnected electron transport pathways and porous channels (that will be filled with liquid electrolytes to activate the charge/discharge reaction).

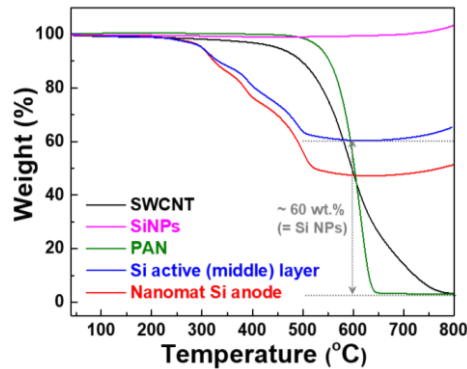


**Figure 2.28** TGA profiles used to estimate the composition ratio of the nanomat Si anode. The composition ratios of the Si active (middle) layer and top/bottom layers were estimated to be (Si nanoparticles/SWCNT)/PAN = (60/6)/34 (w/w/w) and SWCNT/PAN = 40/60 (w/w), respectively. The slight increase in the weight of the Si nanoparticles, Si active (middle) layer, and nanomat Si anode above 700°C was ascribed to the formation of new silicon oxides.

From the thermogravimetric analysis (TGA) measurement (Figure 2.28), the composition ratios of the Si active (middle) layer and top/bottom layers were estimated to be (Si/SWCNT)/PAN = (60/6)/34 (w/w/w) and SWCNT/PAN = 40/60 (w/w), respectively. Meanwhile, the PEDOT:PSS, which was used as an electroconductive dispersing agent<sup>[7]</sup> for SWCNTs, was hardly detected in the SEM image and TGA profiles because of its negligibly small amount (the initial concentration of the PEDOT:PSS in the Si/SWCNT/PEDOT:PSS suspension solution was 0.03 wt%). No inclusion of the PEDOT:PSS resulted in a poor dispersion state of the (Si/SWCNT) suspension solution (Figure 2.29).

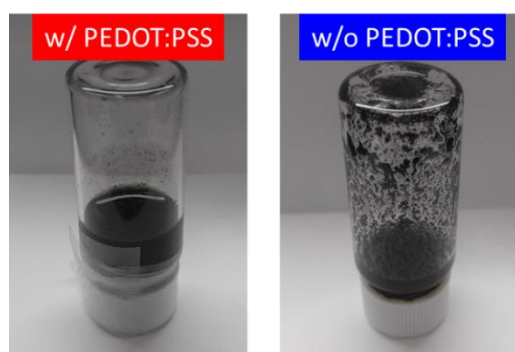


**Figure 2.29** Photograph showing the poor dispersion state of (Si nanoparticle/SWCNT) suspension solution without a PEDOT:PSS additive.

The thin (SWCNT/PAN-interweaved) top/bottom layers in the nanomat Si anodes (Figure 2.27c) was introduced as a type of mat-based flexible electroconductive cushion. A similar concept of the trilayer electrode structure incorporating carbon nanofiber bucky papers as pseudo upper/bottom current collectors was previously reported in the development of metallic current collector-free  $\text{LiNi}_{0.5}\text{Mn}_{1.5}\text{O}_4$  (LNMO)-based cathodes.<sup>[22]</sup> To highlight the structural uniqueness of the nanomat Si anode, a conventional Si anode with a similar Si mass loading ( $\sim 1.5 \text{ mg cm}^{-2}$ ) was prepared using a typical slurry casting method. Figure 2.27d shows that a mixture layer (Si nanoparticles/PAA-CMC binder/carbon black = 70/20/10 (w/w/w), thickness  $\sim 8 \mu\text{m}$ ) was formed on top of a copper (Cu) current collector ( $\sim 20 \mu\text{m}$ ), revealing that the conventional Si anode is thicker than the nanomat Si anode mainly due to the presence of the thick Cu current collector. Figure 2.30a shows that the nanomat Si anode exhibits remarkably higher (in-plane) electronic conductivity (specifically, top/bottom layers =  $72.0 \text{ S cm}^{-1}$ , Si active (middle) layer =  $47.5 \text{ S cm}^{-1}$ ) than the conventional Si anode ( $= 0.1 \text{ S cm}^{-1}$ ), verifying the establishment of highly reticulated SWCNT electronic networks. Meanwhile, the heteronanomat-based porous structure, in combination with the polar PAN nanofibers, allowed for better electrolyte wettability (Figure 2.30b) than the conventional Si anode.

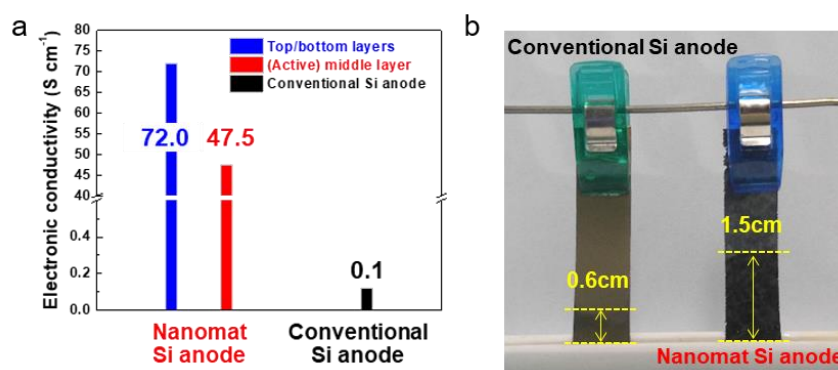


**Figure 2.30** (a) Comparison of the (in-plane) electronic conductivities of the nanomat Si anode and conventional Si anode. (b) Comparison of the electrolyte (1.3 M  $\text{LiPF}_6$  in EC/DEC = 3/7 (v/v) with 10 wt% FEC) wettability between the nanomat Si anode and conventional Si anode.

Driven by the 1D building elements-interweaved heteronanomat skeletons, the nanomat Si anode can withstand mechanical deformation. The change in the electronic resistance of the nanomat Si anode was monitored as a function of the longitudinal compression cycle (bending radius = 5 mm, deformation rate =  $20 \text{ mm min}^{-1}$ , Figure 2.31a). The electronic resistance of the nanomat Si anode remained fairly constant even after 300 bending cycles, whereas a gradual increase in the electronic resistance was observed at the conventional Si anode. This excellent mechanical flexibility was confirmed by the SEM images after the bending cycle test (Figure 2.31b and 2.31c). No significant cracks or defects were

found at the nanomat Si anode, in contrast to the conventional Si anode which was seriously ruptured. The aforementioned results demonstrate that the heteronanomat skeleton-mediated electrode architecture is effective in achieving well-developed 3D-bicontinuous ion/electron transport pathways and mechanical flexibility in the Si anodes.

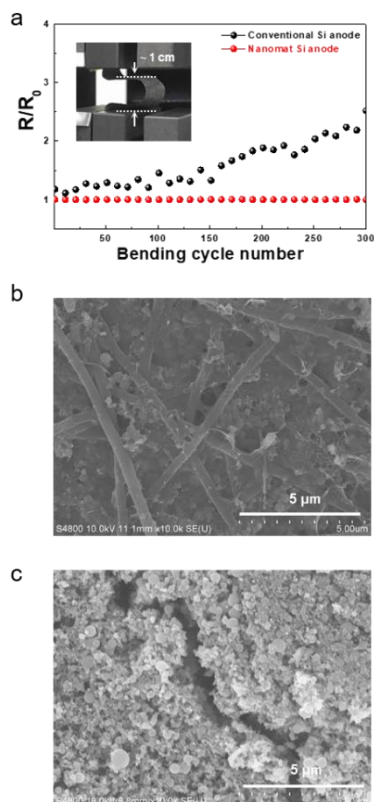


**Figure 2.31** (a) Change in the electronic resistance of nanomat Si and conventional Si anodes as a function of longitudinal compression cycle (bending radius = 5 mm, deformation rate = 20 mm min<sup>-1</sup>). The inset shows a photograph of the deformed nanomat Si anode. SEM images of (b) nanomat Si anode and (c) conventional Si anode after the bending cycle test (300 cycles).

Based on an understanding of the structural/physicochemical properties of the nanomat Si anodes, their electrochemical performance was investigated using a coin half cell (Si anode/PE separator/Li metal). The nanomat Si anode exhibited larger lithiation/delithiation capacities during the 1<sup>st</sup> cycle (at charge/discharge current density = 0.05 C/0.05 C) compared to the conventional Si anode (Figure 2.32a). The larger delithiation capacities (2,431 vs. 2,060 mAh g<sub>Si</sub><sup>-1</sup>) of the nanomat Si anode may arise from the contribution of the SWCNTs. A blank electrode (SWCNT/PAN = 40/60 (w/w), without Si nanoparticles) underwent non-faradaic electrochemical reaction and presented an appreciable level of discharge capacity (= 232 mAh g<sub>SWCNT</sub><sup>-1</sup>, Figure 2.32b). Similar behavior in the CNT-assisted increase in electrode capacity was already reported in our previous work.<sup>[19]</sup> Meanwhile, the nanomat Si anode

presented a larger delithiation capacity than the Si active (middle) layer (Figure 2.32c), indicating that the thin ( $\sim 1 \mu\text{m}$ ) top/bottom layers acted as a nanomat-based electroconductive cushion that could accommodate the lithiation/delithiation-induced volume change of the Si materials.

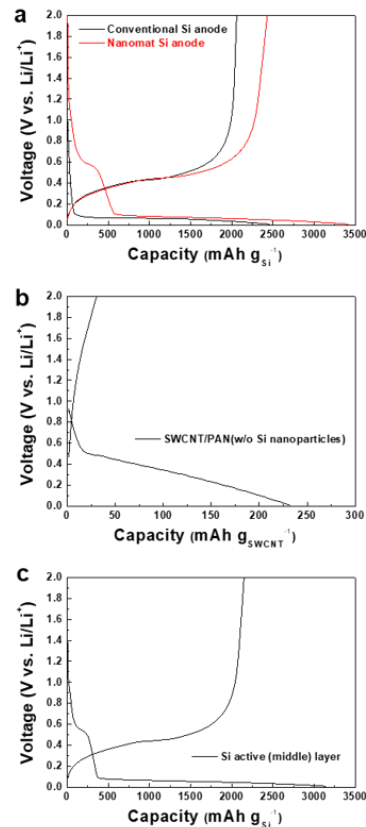


**Figure 2.32** Initial charge (lithiation)/discharge (delithiation) profiles at charge/discharge current densities of 0.05 C/0.05 C, expressed as capacity per Si mass ( $= \text{mAh g}_{\text{Si}}^{-1}$ ). The coin half cell (Si anode/PE separator/Li metal) was used. (a) Nanomat Si anode vs. conventional Si anode. (b) Blank electrode (SWCNT/PAN = 40 / 60 (w/w), without Si nanoparticles). (c) Si active (middle) layer.

To develop practically meaningful high-energy LIBs, considerable attention should be paid to the capacity per mass of the electrode sheets<sup>[19,23,24]</sup> rather than the capacity per mass of electrode active materials which have been widely adopted for describing the electrochemical properties of the electrode active materials themselves. Figure 2.33a shows that the nanomat Si anode presented a substantially higher (initial) delithiation capacity ( $= 1,166 \text{ mAh g}_{\text{anode}}^{-1}$ ) than the conventional Si anode ( $= 122 \text{ mAh g}_{\text{anode}}^{-1}$ ) when our view switched from the capacity ( $\text{mAh g}_{\text{Si}}^{-1}$ ) per mass of Si material to the capacity ( $\text{mAh g}_{\text{anode}}^{-1}$ ) per mass of Si anode sheet. This improvement in the electrode capacity results from the architectural uniqueness of the nanomat Si anode. In particular, the removal of a heavy Cu foil current collector is crucial for lowering the areal weight of the nanomat Si anode (Figure 2.33b), eventually

exerting a beneficial effect on the electrode sheet-based capacity.

In addition, the nanomat Si anode exhibited a higher delithiation rate capability than the conventional Si anode (Figure 2.34a). This result was further verified by galvanostatic intermittent titration technique (GITT) analysis.<sup>[25,26]</sup> Figure 34b shows that the nanomat Si anode effectively suppressed the rise in cell polarization upon repeated current stimuli (at a current density of 0.2 C and interruption time between each pulse of 60 min), wherein the internal cell resistances were presented as a function of the state of charge (SOC) and depth of discharge (DOD). The superior rate performance of the nanomat Si anode was ascribed to the heteronanomat-enabled, 3D-bicontinuous ion/electron transport channels.

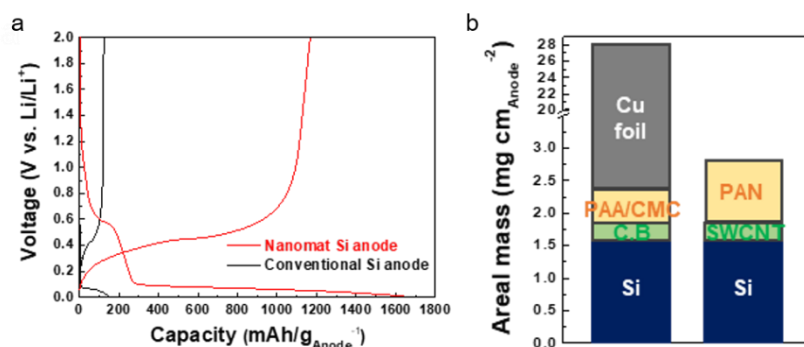


**Figure 2.33** (a) Initial charge (lithiation)/discharge (delithiation) profiles of Si anodes at charge/discharge current densities of 0.05 C/0.05 C, expressed as capacity per mass of Si anode sheet (= mAh g<sub>anode</sub><sup>-1</sup>). (b) Comparison of the areal masses (= mg cm<sub>Anode</sub><sup>-2</sup>) between the nanomat Si anode and conventional Si anode.

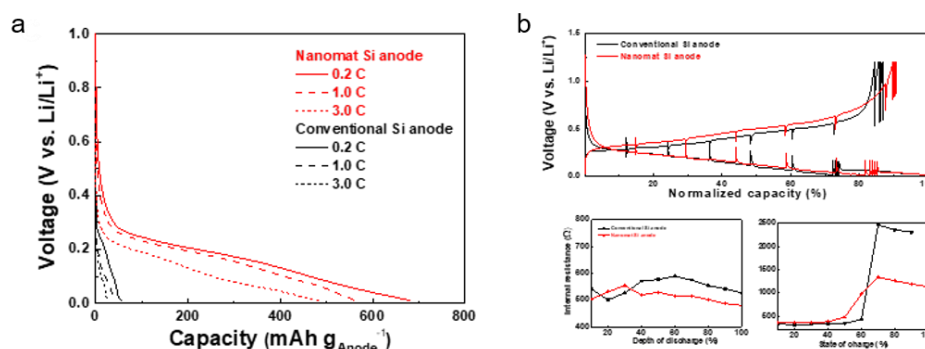


**Figure 2.34** (a) Delithiation rate capability (expressed as mAh g<sub>anode</sub><sup>-1</sup>) of half cells (= Si anode/PE separator/Li metal). The discharge current density was varied from 0.2 to 3.0 C at a constant charge current density of 0.2 C. (b) GITT profiles of half cells upon repeated current stimuli (at a current density of 0.2 C and an interruption time between each pulse of 60 min) and variation in the internal cell resistance as a function of SOC and DOD.

A major challenge facing Si anodes is how to maintain their structural integrity and ion/electron conduction pathways during repeated lithiation/delithiation reactions, which often cause changes in the

volume of the Si anodes. The overpotential distribution of the Si anodes in the through-thickness direction was quantitatively examined as a function of SOC (Figure 2.35a). For this measurement, Cu taps were attached to both the top and bottom sides of the Si anodes (used as a working electrode), and a lithium metal foil was used as a counter/reference electrode (Figure 2.35b). During the lithiation reaction (at a current density of 0.2 C), the nanomat Si anode exhibited a smaller voltage gap ( $\Delta V (= V_{\text{top}} - V_{\text{bottom}}$ , at 50% SOC) = 1.0 mV) than the conventional Si anode ( $\Delta V = 6.5$  mV), indicating lower cell polarization in the through-thickness direction. This result demonstrates that the well-developed ion/electron conduction pathways of the nanomat Si anode facilitated the lithiation kinetics, leading to a uniform voltage distribution in the through-thickness direction.

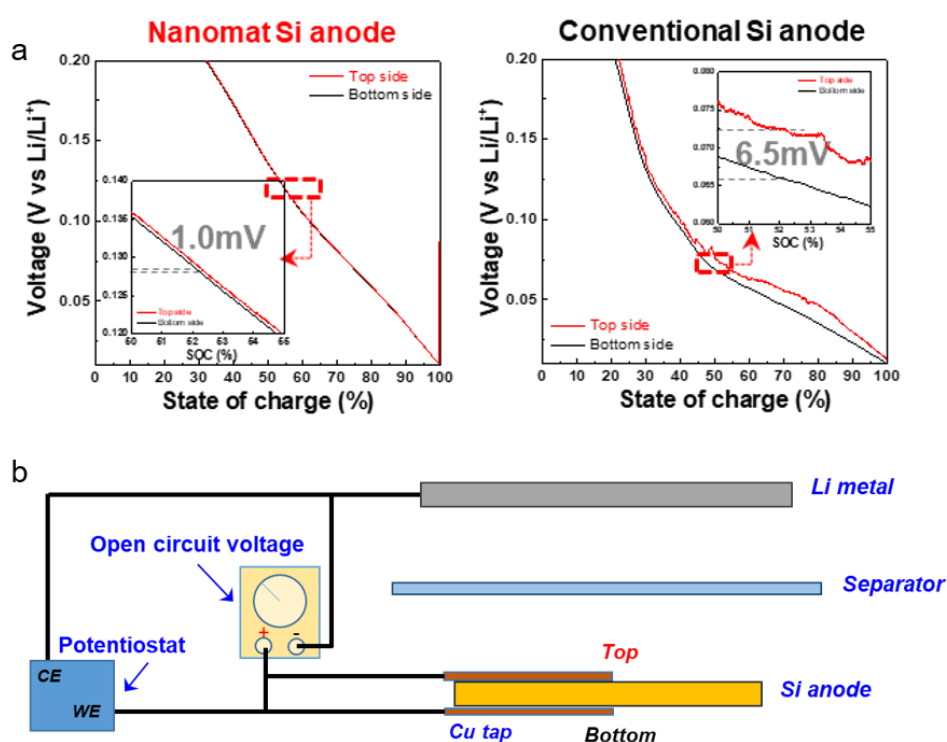


**Figure 2.35** (a) Overpotential distribution of Si anodes in the through-thickness direction as a function of SOC. The voltage gap ( $\Delta V (= V_{\text{top}} - V_{\text{bottom}}$ , at 50% SOC) was measured at a discharge current density of 0.2 C. (b) Schematic representation of a pouch cell designed for the in situ EIS measurement of the overpotential distribution of Si anodes in the through-thickness direction (i.e., voltage difference between the top and bottom sides).

The cycling performance (expressed as  $\text{mAh g}_{\text{Anode}}^{-1}$ ) of the nanomat Si anode was examined at charge/discharge current densities of 0.2 C/0.2 C (Figure 2.36). Remarkable improvement in the capacity retention with cycling (= 87% after 100 cycles) was observed in the nanomat Si anode compared to the conventional Si anode that exhibited a sharp capacity decay ( $\sim 0\%$  after 100 cycles). These cycling results were further verified by analyzing the (through-thickness directional) structural

change of the Si anodes. Figure 2.37a and 2.37c show that the thickness increase in the Si anodes after 100 cycles was significantly suppressed at the nanomat Si anode (12 (before cycling)  $\rightarrow$  21 (after 100 cycles)  $\mu\text{m}$ ) compared to the conventional Si anode (8  $\rightarrow$  45  $\mu\text{m}$ ). Moreover, for the nanomat Si anode, neither appreciable cracks nor morphological disruptions were observed after 100 cycles, in contrast to the conventional Si anode (Figure 2.37b and 2.37d). This result demonstrates that the heteronanomat sheet architecture effectively mitigated the volume change of the Si anodes and maintained the 3D-bicontinuous ion/electron channels during repeated cycling.

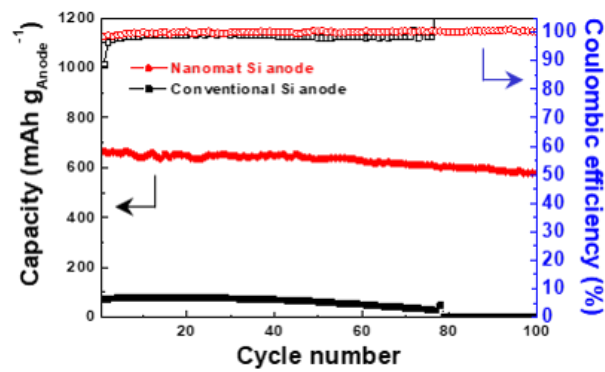


**Figure 2.36** Cycling performance (expressed as  $\text{mAh g}_{\text{Anode}}^{-1}$ ) of half cells: nanomat Si anode vs. conventional Si anode. The half cells were cycled at charge/discharge current densities of 0.2 C/0.2 C under a voltage range of 0.01-1.2 V.

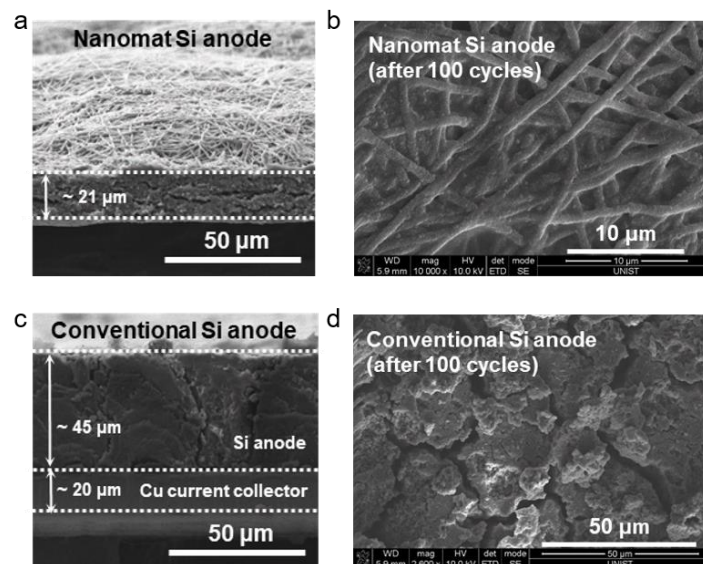


**Figure 2.37** SEM image after the cycle test (100 cycles). (a) and (b) Nanomat Si anode. (c) and (d) Conventional Si anode. The thickness change ( $\Delta t = \text{thickness (after 100 cycles)} - \text{thickness (before cycling)}$ ) of the Si anodes was recorded.

2.2.3.2 Nanomat OLO cathodes based on rambutan-shaped OLO/MWCNT nanocomposite powders

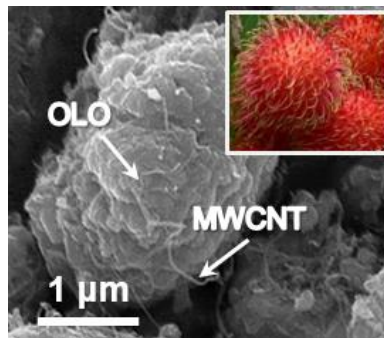


**Figure 2.38** SEM image of rambutan-shaped OLO/MWCNT nanocomposite (referred to as “R-OM”) powders. The inset is a photograph of rambutan fruit.

A formidable problem in OLO cathode materials is their low electronic conductivity. Here, we prepared a new class of nanocomposite powders composed of OLO nanoparticles and multi-walled carbon nanotubes (MWCNTs) to address this issue. The bare OLO powders (average diameter = 5 μm, Figure 2.39a) were mixed with the MWCNTs by ball milling in the presence of 1 wt% PVP, yielding rambutan-shaped OLO/MWCNT (= 100/10 (w/w)) nanocomposite (referred to as “R-OM”) powders (Figure 2.38). Notably, the highly reticulated MWCNT networks in the R-OM powders are expected to provide a significant improvement in electronic conductivity compared to the bare OLO powders, which will be further discussed below.

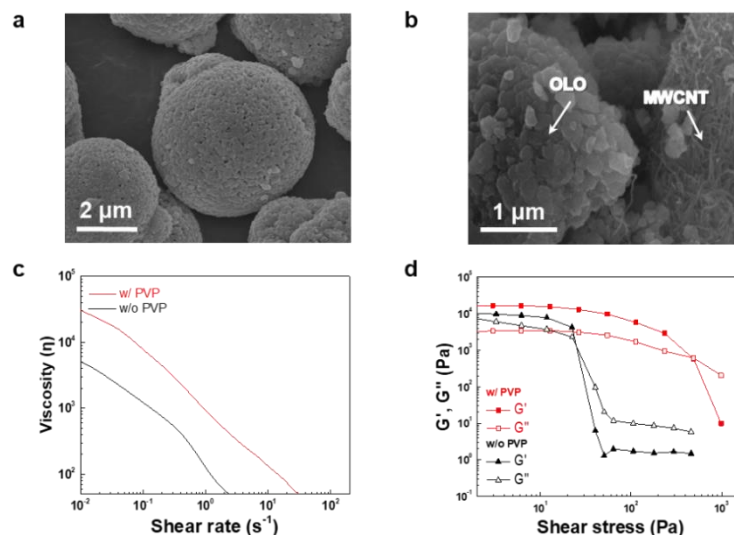


**Figure 2.39** (a) SEM image of bare OLO powders (average diameter = 5 μm). (b) SEM image showing the poor mixing state of OLO nanoparticle aggregates and MWCNTs. (c) Viscosity of the OLO/MWCNT suspension (with PVP vs. without PVP). (d) Viscoelastic properties ( $G'$  and  $G''$ ).

PVP, which is known as a nonionic dispersant for MWCNTs, was used to stabilize the dispersion state of the OLO/MWCNT suspension. As a control sample, OLO/MWCNT (= 100/10 (w/w)) nanocomposite powders were prepared in the absence of PVP. In the control powders, the OLO nanoparticle aggregates were not homogeneously mingled with the MWCNTs (Figure 2.39b). This PVP-assisted stabilization of the OLO/MWCNT suspension was further verified by analyzing its rheological properties (Figure 2.39c and 2.39d).<sup>[27,28]</sup> The OLO/MWCNT suspension containing the PVP dispersant exhibited a higher shear viscosity and more elastic behavior (*i.e.*,  $G'$  (storage modulus)  $>$   $G''$  (loss modulus)) over a wide range of shear stress compared to the OLO/MWCNT suspension without PVP.

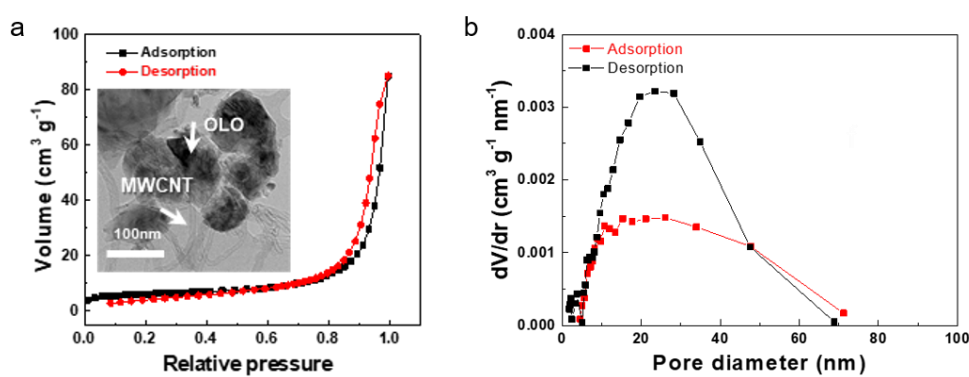


**Figure 2.40** (a)  $N_2$  adsorption-desorption of R-OM powders. The inset shows the HR-TEM image. (b) BJH plot showing the average pore size of the R-OM powders.

The good dispersion state of the OLO/MWCNT suspension allowed for the formation of highly interconnected MWCNT networks/porous interstitial voids (that serve as ionic conduction channels) in close contact with OLO nanoparticles. The porous interstitial voids of the R-OM particles were verified by a high-resolution transmission electron microscopy (HR-TEM) image (inset of Figure 2.40a). The  $N_2$  adsorption-desorption isotherm (Figure 2.40a) shows that the specific surface area of the R-OM powders is  $22.2 \text{ m}^2 \text{ g}^{-1}$ . In addition, the BJH plot (Figure 2.40b) showed that the average pore sizes of the R-OM powders were estimated to be 24.0 nm from the desorption mode and 33.1 nm from the adsorption mode. The porous interstitial voids, in collaboration with the MWCNT networks, are expected to facilitate the redox reaction kinetics of the R-OM powders.

The effect of MWCNT content on the morphology and properties of the R-OM powders was investigated. Randomly aggregated OLO nanoparticles were observed in the absence of MWCNTs (Figure 2.41a). Over the entire range of MWCNT contents (= 3, 5 and 15 wt%, shown in Figure 2.41) examined herein, rambutan-shaped, micron-sized OLO/MWCNT nanocomposite powders were formed, indicating that the MWCNTs act as an electroconductive fibrous binder that tightly holds the OLO

nanoparticles. For MWCNT content of 3 and 5 wt%, the population density of the MWCNTs was not sufficiently high for constructing well-reticulated MWCNT networks. Meanwhile, an excessively high MWCNT content (= 15 wt%) resulted in the generation of independently existing OLO and MWCNT aggregates besides the OLO/MWCNT nanocomposite powders. To quantitatively elucidate the effect of the MWCNT content in the R-OM powders, OLO cathode sheets (R-OM powder/PVDF binder/carbon black additive = 80/10/10 (w/w/w)) were prepared using a typical slurry casting method. The (in-plane) electronic conductivities of the OLO cathodes increased with MWCNT content (Figure 2.42a). The discharge rate capability of the OLO cathodes (at a constant charge current density of 0.2 C) was examined using a coin half cell (OLO cathode/PE separator/lithium metal anode). The R-OM powders with the 10 wt% MWCNT showed the highest rate performance (Figure 2.42b). The lower rate capability of the 15 wt% MWCNT compared to the 10 wt% MWCNT could be attributed to the unwanted formation of the independently existing OLO and MWCNT aggregates, which are unfavorable for ion/electron transport in the R-OM powders. Based on these results, the optimal MWCNT content of the R-OM powders was suggested to be 10 wt%.

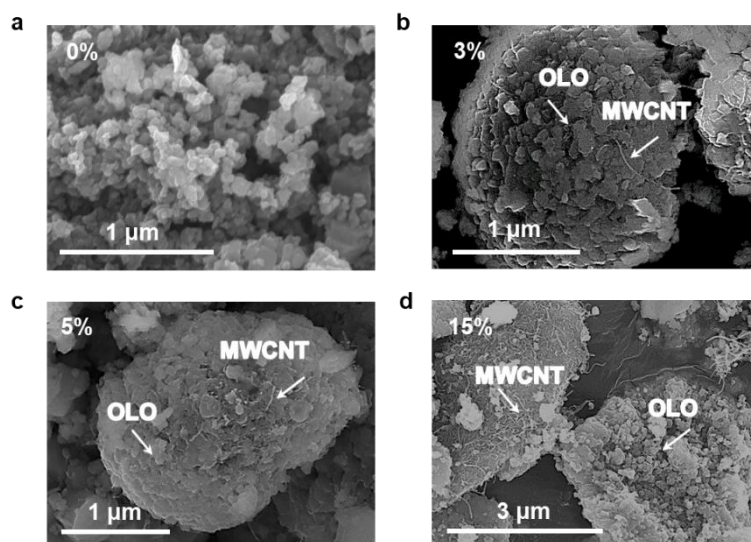


**Figure 2.41** SEM images of R-OM powders with different MWCNT contents: (a) 0, (b) 3, (c) 5, (d) 15 wt%.

The nanomat OLO cathode includes the PAN/PVP mixture nanofibers as 1D-shaped binders. PVP, due to its pyrrolidone ring (containing lone pair electrons)-driven Lewis basicity,<sup>[29,30]</sup> is known to scavenge metal ions (e.g.,  $Mn^{2+}$ ) dissolved from lithium metal oxide-based cathode materials. Here, PAN and PAN/PVP (= 50/50 (w/w)) films were prepared as model systems to quantitatively examine beneficial function of PVP. No bare PVP film was tested because PVP tends to lose its dimensional stability easily upon being immersed in LIB electrolytes.<sup>[20]</sup> The  $Mn^{2+}$ -chelating ability of the PAN and PAN/PVP films in the electrolyte solution was analyzed by measuring the amount of captured  $Mn^{2+}$  ions (Figure 2.43),

where the PAN and PAN/PVP films were immersed in manganese perchlorate solution (10 mM  $\text{Mn}(\text{ClO}_4)_2$ -containing 1.0 M  $\text{LiPF}_6$  in EC/DMC = 1/1 (v/v)) for 2 h at room temperature. The amount of  $\text{Mn}^{2+}$  ions (= 224 ppm) trapped by the PAN/PVP film was significantly larger than for the PAN film (= 3 ppm). The beneficial effect of this  $\text{Mn}^{2+}$ -chelating capability of the PAN/PVP on cell performance will be discussed in the following section.

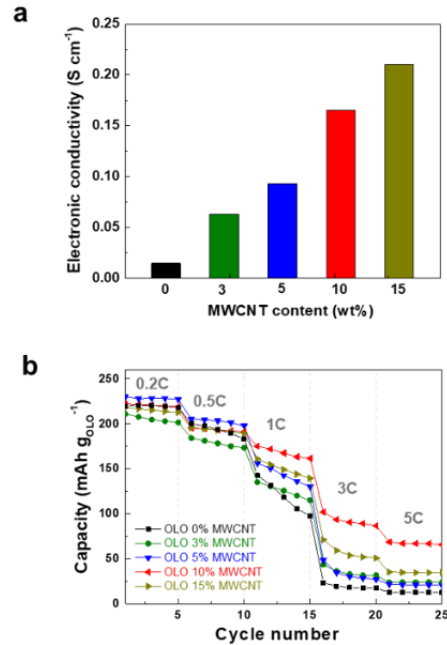


**Figure 2.42** (a) (In-plane) Electronic conductivities and (b) discharge rate capabilities (coin half cell (OLO cathode/PE separator/lithium metal anode, the discharge current density was varied from 0.2 to 5.0 C at a fixed charge current density of 0.2 C) of the OLO cathodes (R-OM powder/PVdF binder/carbon black additive = 80/10/10 (w/w/w), where the MWCNT contents in the R-OM powders were 0, 3, 5, 10 and 15 wt%).

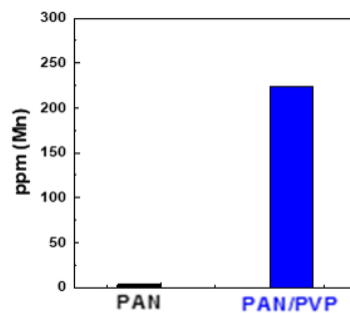


**Figure 2.43** Amount of  $\text{Mn}^{2+}$  ions captured by PAN and PAN/PVP (= 50/50 (w/w)) films (measured by ICP-MS analysis).

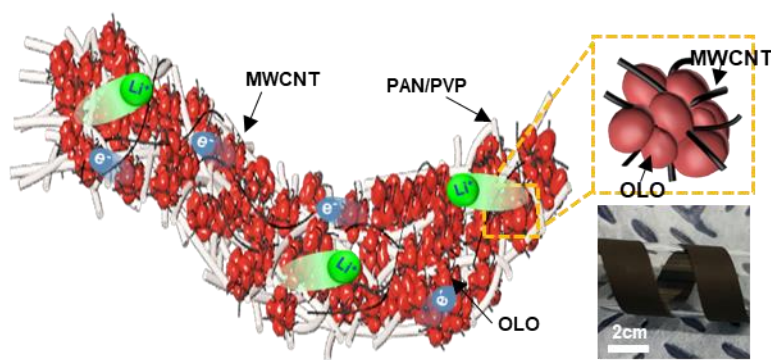


**Figure 2.44** Conceptual representation depicting the structural uniqueness of the nanomat OLO cathode. Its photograph was inserted.

After preparing the major components, the nanomat OLO cathodes were fabricated through concurrent electrospinning (for PAN/PVP nanofibers) and electrospaying (for R-OM powders/MWCNTs). A conceptual representation depicting the structural uniqueness of the nanomat OLO cathode, alongside a photograph showing the mechanical flexibility, is shown in Figure 2.44.

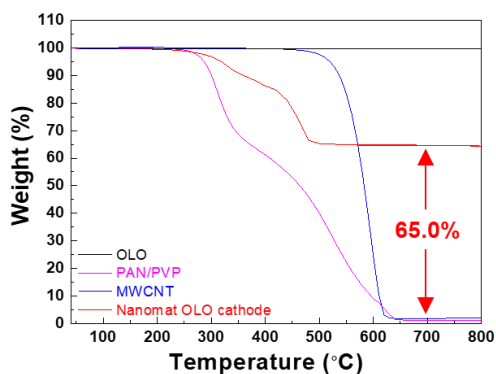


**Figure 2.45** TGA profiles used to estimate composition ratio of the nanomat OLO cathode; the weight-based ratio of OLO/MWCNT/(PAN-PVP) was 65/13/22 (w/w/w).

The composition ratio of the nanomat OLO cathode was estimated to be OLO/MWCNT/(PAN-PVP) = 65/13/22 (w/w/w) from the TGA measurement (Figure 2.45). Figure 2.46a shows that the R-OM powders were densely packed in the MWCNT/(PAN/PVP)-interweaved heteromat without a metallic Al foil current collector, leading to the formation of 3D-bicontinuous ion/electron transport pathways, which appeared similar to the results for the nanomat Si anode. The highly interconnected electronic channels of the nanomat OLO cathode were confirmed by comparing its electronic conductivity with the conventional OLO cathode. The conventional OLO cathode (OLO/PVdF/carbon black = 80/10/10 on an Al foil, Figure 2.46b) was fabricated using a slurry casting method. Figure 2.46c shows that the

nanomat OLO cathode ( $= 7.55 \text{ S cm}^{-1}$ ) exhibited a substantially higher electronic conductivity than the conventional OLO cathode ( $= 0.17 \text{ S cm}^{-1}$ ), which was attributed to the combined effect of the highly interconnected MWCNT networks and the (rambutan-shaped) R-OM powders. In addition to the superior electronic conductivity, the nanomat OLO cathode presented better electrolyte wettability than the conventional OLO cathode (Figure 2.46d), verifying the well-developed porous structure. Meanwhile, the nanomat architecture allowed for a significant improvement in the bending deformation. During the repeated bending cycles, the electronic resistance of the nanomat OLO cathode remained nearly unchanged, in contrast to the conventional OLO cathode that exhibited a gradual increase in the electronic resistance (Figure 2.47).

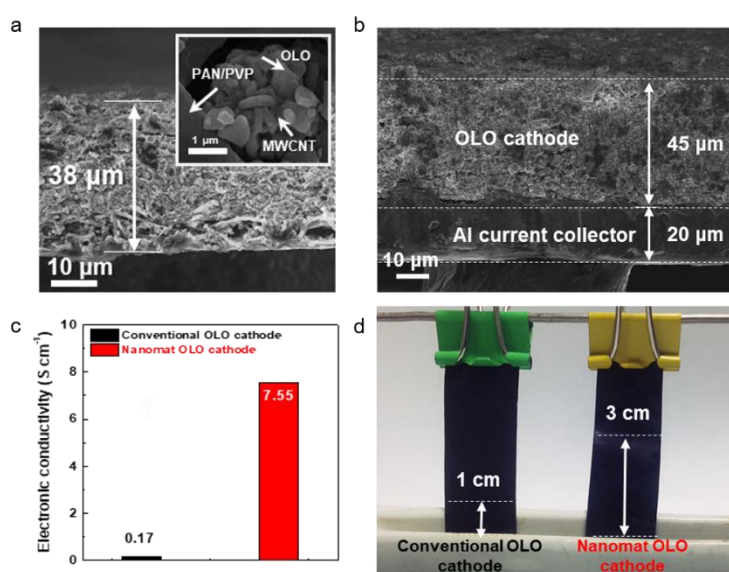


**Figure 2.46** Cross-sectional SEM image of OLO cathodes: (a) Nanomat OLO cathode. R-OM powders were densely packed in the MWCNT/(PAN/PVP)-interweaved heteromat without an Al foil current collector. The inset shows a high-magnification view, (b) conventional OLO cathode (OLO/PVdF/carbon black = 80/10/10 on an Al foil). (c) Comparison of the electronic conductivities between the nanomat OLO cathode and conventional OLO cathode (OLO/PVdF/carbon black = 80/10/10 on an Al foil, fabricated by a slurry casting method). (d) Electrolyte (1 M  $\text{LiPF}_6$  in EC/DMC = 1/1 (v/v)) wettability.

The electrochemical performance of the nanomat OLO cathode was investigated using a coin half cell (OLO cathode/PE separator/Li metal anode). Similar to the approach in the nanomat Si anodes, the charge/discharge capacities of the nanomat OLO cathode were expressed as the capacity (*i.e.*, mAh  $\text{g}_{\text{cathode}}^{-1}$ ) per weight of cathode sheet. A comparison of the total areal mass between the nanomat OLO and conventional OLO cathodes is shown in Figure 2.48a, revealing the lower areal mass of the nanomat OLO cathode. Figure 2.48b shows that the nanomat OLO cathode presented significantly higher

discharge capacities than the conventional OLO cathode over a wide range of discharge current densities (from 0.2 to 5.0 C at a fixed charge current density of 0.2 C). The removal of the heavy Al foil current collector, in combination with the 3D-bicontinuous ion/electron transport channels, contributed to this improvement in the discharge capacities of the nanomat OLO cathode.

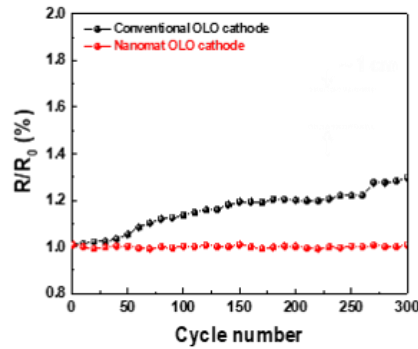


**Figure 2.47** Change in the electronic resistances of the nanomat OLO and conventional OLO cathodes as a function of longitudinal compression cycle (bending radius of 5 mm, deformation rate of 200 mm min<sup>-1</sup>). The inset shows a photograph of the deformed nanomat OLO cathode.

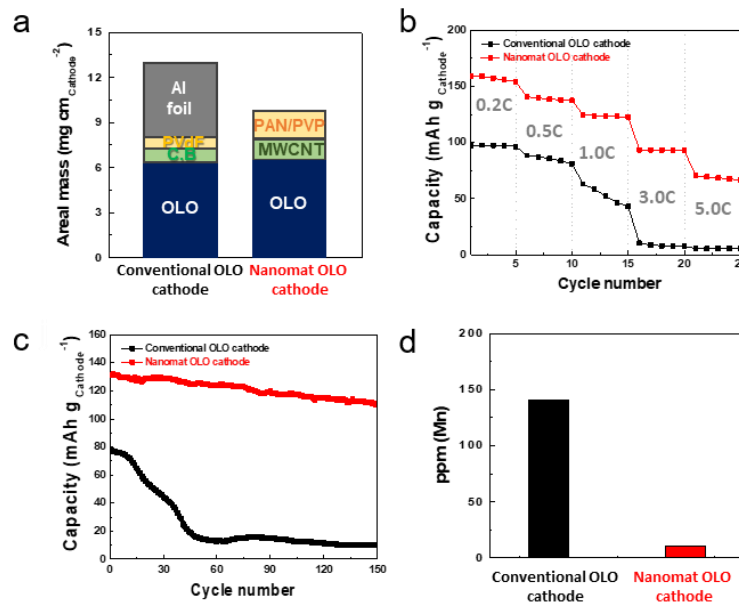


**Figure 2.48** (a) Comparison of the areal masses (= mg cm<sub>Cathode</sub><sup>-2</sup>) between the nanomat OLO cathode and conventional OLO cathode. (b) Discharge rate capability (expressed as mAh g<sub>Cathode</sub><sup>-1</sup>) of half cells (OLO cathode/PE separator/Li metal): nanomat OLO cathode vs. conventional OLO cathode. The discharge current density was varied from 0.2 to 5.0 C at a fixed charge current density of 0.2 C. (c) Cycling performance (expressed as mAh g<sub>Cathode</sub><sup>-1</sup>) of nanomat OLO cathode (vs. conventional OLO cathode) at charge/discharge current densities of 1.0 C/1.0 C under a voltage range of 2.0-4.7 V. (d) Amount of metallic Mn deposited on lithium metal anodes after the cycling test (estimated from ICP-MS analysis).

A more distinctive achievement of the nanomat OLO cathode was the cycling performance (expressed as  $\text{mAh g}_{\text{cathode}}^{-1}$ ), where the cells were cycled at a charge/discharge current density of 1.0 C/1.0 C under a voltage range of 2.0-4.7 V. The nanomat OLO cathode exhibited higher discharge capacities and stable capacity retention with cycling (85% after 150 cycles) (Figure 2.48c), whereas the conventional OLO cathode suffered from a sharp decline in capacity after only 40 cycles. To elucidate this superior cycling performance of the nanomat OLO cathode, the cells were disassembled after the cycling test. The Li metal anodes were selectively collected and then subjected to a post-mortem analysis. The deposition of metallic Mn on the lithium metal anodes<sup>[31,32]</sup> was quantitatively examined using ICP-MS analysis. Figure 2.48d shows that the amount of metallic Mn deposited on the lithium metal anode was significantly lower at the nanomat OLO cathode (= 11 ppm) than at the conventional OLO cathode (= 141 ppm), confirming that the PAN/PVP nanofibers in the nanomat OLO cathode effectively capture the  $\text{Mn}^{2+}$  ions dissolved from the OLO materials.

### 2.2.3.3 All-nanomat (Si anode/ $\text{Al}_2\text{O}_3$ separator/OLO cathode) full cells for ultrahigh energy density and mechanical flexibility

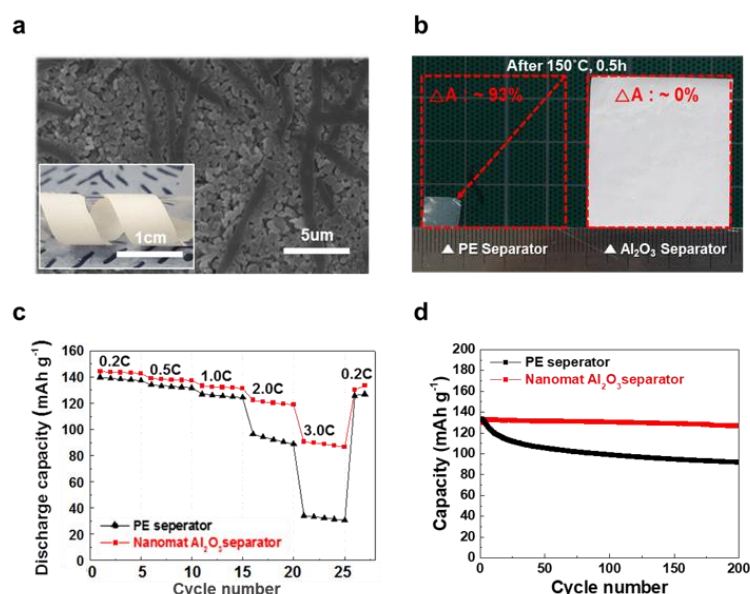


**Figure 2.49** Structure and basic membrane properties of nanomat  $\text{Al}_2\text{O}_3$  separator. (a) SEM image and photograph (inset). (b) Thermal shrinkage after exposure to 150°C for 0.5 h (nanomat  $\text{Al}_2\text{O}_3$  separator vs. PE separator). (c) Discharge rate capability of cells (nanomat  $\text{Al}_2\text{O}_3$  separator vs. PE separator). (d) Cyclability of cells (nanomat  $\text{Al}_2\text{O}_3$  separator vs. PE separator). The cells consisted of a  $\text{LiCoO}_2$  cathode ( $\text{LiCoO}_2/\text{carbon black}/\text{PVdF} = 95/2.5/2.5$  (w/w/w)) and graphite anode ( $\text{graphite}/\text{carbon black}/\text{SBR}/\text{CMC} = 96/1/2/1$  (w/w/w)).

The nanomat Si anodes and OLO cathodes prepared above were assembled with nanomat  $\text{Al}_2\text{O}_3$

separators to produce all-nanomat LIB full cells. Here, the nanomat  $\text{Al}_2\text{O}_3$  separators (Figure 2.49), which were fabricated using the concurrent electrospinning (for polymeric nanofibers)/electrospraying (for  $\text{Al}_2\text{O}_3$  nanoparticles) process, were chosen as an alternative to commercial polyolefin separators. The structural novelty and superior thermal, mechanical and electrochemical properties of the nanomat  $\text{Al}_2\text{O}_3$  separators compared to commercial polyolefin separators were reported in our previous work.<sup>[20]</sup>

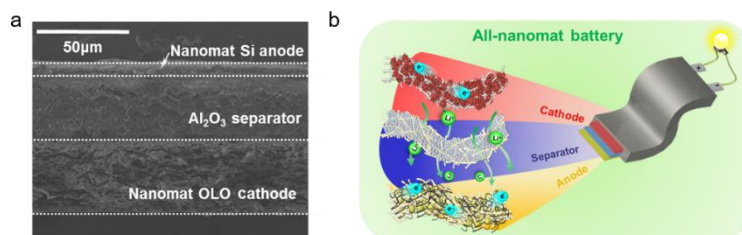


**Figure 2.50** (a) Cross-sectional SEM image of all-nanomat full cell (Si anode/ $\text{Al}_2\text{O}_3$  separator/OLO cathode). (b) Conceptual representation of all-nanomat full cells based on 1D building elements-interweaved heteronanomat skeletons.

A cross-sectional SEM image of the all-nanomat LIB full cell (Si anode/ $\text{Al}_2\text{O}_3$  separator/OLO cathode) is shown in Figure 2.50a. It should be noted that the major components (*i.e.*, anode, cathode, and separator) of the all-nanomat full cell were based on the 1D building elements-interweaved heteronanomat skeletons. Typical metallic (Cu and Al) foil current collectors were not included in the all-nanomat full cell. This architectural uniqueness of the all-nanomat full cell, in combination with its chemical functionalities, plays a significant role in the electrochemical performance and mechanical deformability. These structural features of the all-nanomat full cell are conceptually illustrated in Figure 50b, with particular attention to the 3D bicontinuous ion/electron transport pathways and mechanical flexibility.

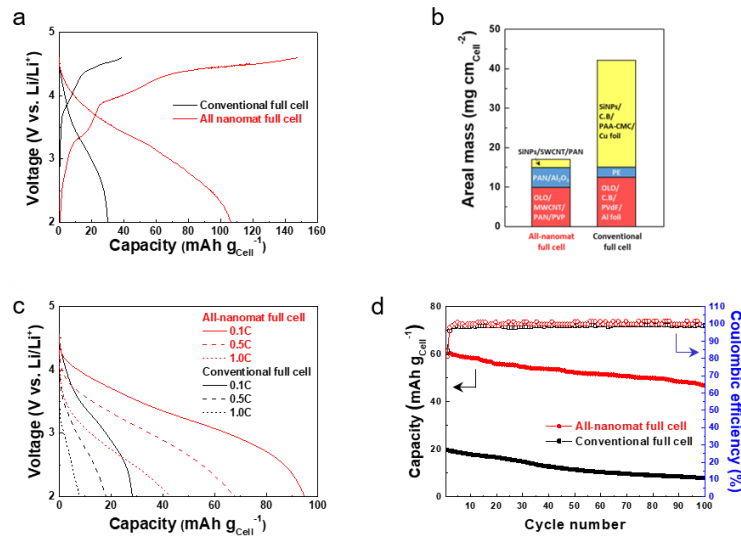


**Figure 2.51** (a) Initial charge/discharge profiles (at charge/discharge current densities of 0.05 C/0.05 C under a voltage range of 2.0-4.6 V) of full cells (all-nanomat vs. conventional), expressed as capacity (mAh g<sub>Cell</sub><sup>-1</sup>) per cell weight (= anode + cathode + separator). (b) Comparison of the areal masses (= mg cm<sub>Cell</sub><sup>-2</sup>) of the cell components (*i.e.*, anode, cathode and separator) between the all-nanomat full cell and conventional full cell. (c) Discharge rate capability (expressed as mAh g<sub>Cell</sub><sup>-1</sup>) of full cells (all-nanomat vs. conventional). The discharge current density was varied from 0.1 to 1.0 C at a fixed charge current density of 0.1 C. (d) Cycling performance (expressed as mAh g<sub>Cell</sub><sup>-1</sup>) of full cells (all-nanomat vs. conventional) at a charge/discharge current density of 0.5 C/0.5 C.

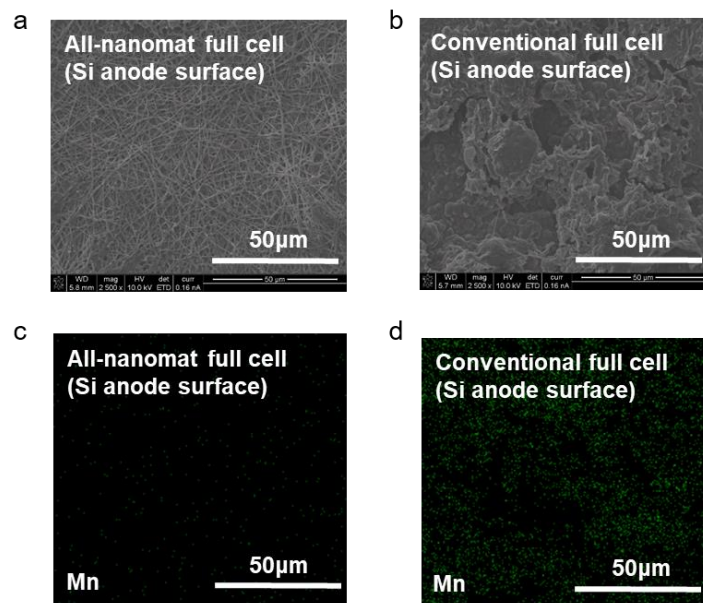


**Figure 2.52** SEM and EDS images (green dots represent metallic Mn deposited on the Si anode surface) showing the structural change of the Si anodes after 100 cycles. (a) and (c) All-nanomat full cell. (b) and (d) Conventional full cell.

In addition, the all-nanomat full cell presented a better discharge rate capability (at a fixed charge current density of 0.1 C) than the conventional full cell (Figure 2.51c), revealing the beneficial effect of the 3D-bicontinuous ion/electron transport pathways on Faradaic reaction kinetics. The cycling performance (expressed as  $\text{mAh g}_{\text{cell}}^{-1}$ ) of the all-nanomat full cell was investigated at a charge/discharge current density of 0.5 C/0.5 C (Figure 2.51d). The conventional cell showed poor cycling performance (capacity =  $7.9 \text{ mAh g}_{\text{cell}}^{-1}$ , capacity retention = 38% after only 100 cycles). In comparison, the all-nanomat full cell showed significant improvement in the cycling performance (capacity =  $46.9 \text{ mAh g}_{\text{cell}}^{-1}$ , capacity retention = 76% after 100 cycles), demonstrating the advantages of the unusual all-nanomat architecture. To further elucidate the superior cycling performance of the all-nanomat full cell, the structural change of the Si anode surface was investigated. The nanomat Si anode (Figure 2.52a and 2.52c) remained relatively clean without structural disruption, whereas the conventional Si anode (Figure 2.52b and 2.52d) was highly contaminated with Mn byproducts. The ICP-MS analysis (Figure 2.53) showed that the amount of metallic Mn deposited on the nanomat Si anode (= 60 ppm) was considerably lower than that on the conventional Si anode (= 326 ppm).

Energy density [Wh $\text{kg}_{\text{Cell}}^{-1}$ ]	Energy density [Wh $\text{kg}_{\text{Anode}}^{-1}$ ]	Current density [C-rate]	Cathode	Reference
	270	0.12C	LiCoO <sub>2</sub>	[33]
	118	0.05C	LiCoO <sub>2</sub>	[34]
	237	0.12C	LiFePO <sub>4</sub>	[35]
	360	0.3C	LiMn <sub>1/3</sub> Ni <sub>1/3</sub> Co <sub>1/3</sub> O <sub>2</sub>	[36]
479		0.2C	OLO	This study

**Table 2.1** Comparison of the gravimetric full cell capacity between the all-nanomat (Si/OLO) full cell (expressed as  $\text{mAh g}_{\text{cell}}^{-1}$ ) and previously reported (Si anode-incorporating) full cells (expressed as  $\text{mAh g}_{\text{Si anode}}^{-1}$ ).

To highlight the superior electrochemical performance of the all-nanomat full cell, its gravimetric energy density (=  $\text{Wh kg}_{\text{cell}}^{-1}$ ) was compared with the values (expressed as  $\text{Wh kg}_{\text{Si anode}}^{-1}$ ) for previously reported (Si anode-containing) full cells. Unfortunately, cell weight-based energy densities were not provided in the previous publications. For this reason, the Si anode weight-based energy densities were considered for this comparison. The all-nanomat full cell exhibited a higher gravimetric energy density ( $479 \text{ Wh kg}_{\text{cell}}^{-1}$ ) (Table 2.1) than the previous results despite the unfair comparison (*i.e.*,  $\text{Wh kg}_{\text{cell}}^{-1}$  vs.  $\text{Wh kg}_{\text{Si anode}}^{-1}$ ). Furthermore, this energy density is significantly higher than a target value ( $350 \text{ Wh kg}_{\text{cell}}^{-1}$ )<sup>[33]</sup> for long-range EV batteries announced by the 2020 commercialization project of the US Advanced Battery Consortium (USABC).

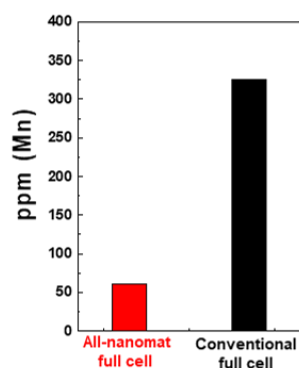


**Figure 2.53** Amount of metallic Mn (estimated from ICP-MS analysis) deposited on Si anodes: all-nanomat full cell vs. conventional full cell.

In addition to the superior electrochemical performance described above, the all-nanomat full cell, driven by its 1D building elements-interweaved heteronanomat skeletons, exhibited good mechanical flexibility. Figure 2.54a shows that the all-nanomat full cell maintained stable charge/discharge profiles without mechanical rupture after 100 bending cycles (bending diameter of 5 mm). Moreover, the all-nanomat full cells operated LED lamps even after being folded 3 times and severely crumpled (Figure 2.54b). This unprecedented progress in electrochemical performance (rate capability, cycling performance, and energy density) and mechanical flexibility underlines the exceptional functions of the all-nanomat cell architecture, suggesting its potential as a competent platform technology for high-performance/flexible rechargeable batteries.

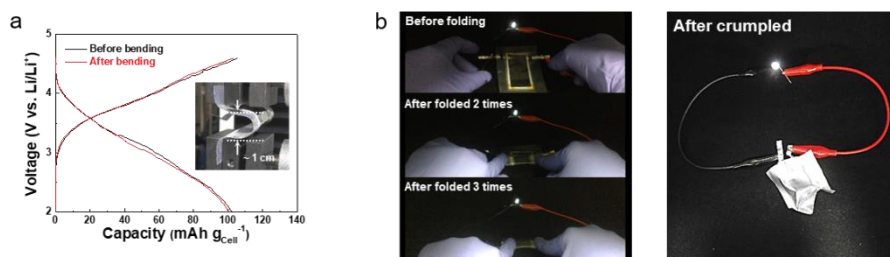


**Figure 2.54** (a) Charge/discharge profiles (expressed as  $\text{mAh g}_{\text{Cell}}^{-1}$ ) of all-nanomat full cell before/after 100 bending cycles (bending diameter = 5 mm). The inset shows a photograph of the deformed all-nanomat full cell. (b) Photographs of all-nanomat full cells showing the operation of LED lamps: after being folded 3 times (left) and after being seriously crumpled (right).

## 2.2.4 Conclusion

In summary, we demonstrated the all-nanomat (Si anode/ $\text{Al}_2\text{O}_3$  separator/OLO cathode) LIB full cells

based on the 1D building elements (polymeric nanofibers and CNTs)-interweaved heteronanomat skeletons as a facile and effective approach to enable ultrahigh energy density and mechanical flexibility. The nanomat Si anodes (or OLO cathodes) were fabricated through concurrent electrospinning (for polymeric nanofibers) and electrospaying (for electrode materials/CNTs), leading to the compact packing of Si (or OLO) powders in close contact with spatially interweaved polymeric nanofibers/CNT heteromats. As a result, 3D-bicontinuous ion/electron transport channels were uniformly developed throughout the entire nanomat electrodes. The highly-reticulated CNT networks allowed for the removal of metallic foil current collectors, in addition to providing well-interconnected electronic pathways in the nanomat electrodes. The polymeric nanofibers (PAN for Si anodes, PAN/PVP for OLO cathodes) acted as multifunctional 1D-shaped electrode binders. In particular, the PVP contributed to trapping the  $Mn^{2+}$  ions dissolved from OLO materials due to its pyrrolidone ring-driven Lewis basicity. The rambutan-shaped OLO/MWCNT composite powders were included in the nanomat OLO cathodes to resolve the low electronic conductivity of OLO materials. The nanomat  $Al_2O_3$  separator was used as an alternative separator beyond commercial polyolefin separators. The all-nanomat (Si/OLO) full cell provided exceptional improvement in cell performance (notably, cell-based gravimetric energy density =  $479 \text{ Wh kg}_{\text{cell}}^{-1}$ ) and mechanical deformability due to the chemical functionalities and structural benefits of the heteronanomat skeleton-mediated electrodes and separators, which were difficult to achieve with conventional LIB technologies. We envision that the all-nanomat cell architecture can be easily combined with a variety of electrode materials, eventually opening up new avenues as a versatile platform for the development of advanced power sources in the incessant pursuit of high-energy density and flexibility.

### 2.2.5 Reference

1. J.-M. Tarascon, M. Armand, *Nature* **2001**, *414*, 359.
2. F. Cheng, J. Liang, Z. Tao, J. Chen, *Adv. Mater.* **2011**, *23*, 1695.
3. Y. Xu, M. Zhou, Y. Lei, *Adv. Energy Mater.* **2016**, *6*, 1502514.
4. M. Yousaf, H. T. H. Shi, Y. Wang, Y. Chen, Z. Ma, A. Cao, H. E. Naguib, R. P. S. Han, *Adv. Energy Mater.* **2016**, *6*, 1600490.
5. W. Liu, M. S. Song, B. Kong, Y. Cui, *Adv. Mater.* **2017**, *29*, 1603436.
6. K. Fu, O. Yildiz, H. Bhanushali, Y. Wang, K. Stano, L. Xue, X. Zhang, P. D. Bradford, *Adv. Mater.* **2013**, *25*, 5109.
7. Z. Chen, J. W. F. To, C. Wang, Z. Lu, N. Liu, A. Chortos, L. Pan, F. Wei, Y. Cui, Z. Bao, *Adv. Energy Mater.* **2014**, *4*, 1400207.
8. Y. Xu, Y. Zhu, F. Han, C. Luo, C. Wang, *Adv. Energy Mater.* **2015**, *5*, 1400753.

9. Y. Ma, R. Younesi, R. Pan, C. Liu, J. Zhu, B. Wei, K. Edström, *Adv. Funct. Mater.* **2016**, *26*, 6797.
10. C. Li, C. Liu, W. Wang, J. Bell, Z. Mutlu, K. Ahmed, R. Ye, M. Ozkan, C. S. Ozkan, *Chem. Commun.* **2016**, *52*, 11398.
11. H. Wu, Y. Cui, *Nano Today* **2012**, *7*, 414.
12. T.-H. Kim, J.-S. Park, S. K. Chang, S. Choi, J. H. Ryu, H.-K. Song, *Adv. Energy Mater.* **2012**, *2*, 860.
13. A. Manthiram, J. C. Knight, S.-T. Myung, S.-M. Oh, Y.-K. Sun, *Adv. Energy Mater.* **2016**, *6*, 1501010.
14. Wang, X. He, E. Paillard, N. Laszczynski, J. Li, S. Passerini, *Adv. Energy Mater.* **2016**, *6*, 1600906.
15. M. Ko, P. Oh, S. Chae, W. Cho, J. Cho, *Small* **2015**, *11*, 4058.
16. X. Zuo, J. Zhu, P. Müller-Buschbaum, Y.-J. Cheng, *Nano Energy* **2017**, *31*, 113.
17. A. R. Armstrong, M. Holzapfel, P. Novák, C. S. Johnson, S.-H. Kang, M. M. Thackeray, P. G. Bruce, *J. Am. Chem. Soc.* **2006**, *128*, 8694.
18. X. Yu, Y. Lyu, L. Gu, H. Wu, S. M. Bak, Y. Zhou, K. Amine, S. N. Ehrlich, H. Li, K. W. Nam, *Adv. Energy Mater.* **2014**, *4*.
19. J.-M. Kim, C.-H. Park, Q. Wu, S.-Y. Lee, *Adv. Energy Mater.* **2016**, *6*, 1501594.
20. J.-H. Kim, J.-H. Kim, J.-M. Kim, Y.-G. Lee, S.-Y. Lee, *Adv. Energy Mater.* **2015**, *5*, 1500954.
21. X. H. Liu, L. Zhong, S. Huang, S. X. Mao, T. Zhu, J. Y. Huang, *ACS Nano* **2012**, *6*, 1522.
22. X. Fang, M. Ge, J. Rong, C. Zhou, *ACS Nano* **2014**, *8*, 4876.
23. S.-J. Cho, K.-H. Choi, J.-T. Yoo, J.-H. Kim, Y.-H. Lee, S.-J. Chun, S.-B. Park, D.-H. Choi, Q. Wu, S.-Y. Lee, S.-Y. Lee, *Adv. Funct. Mater.* **2015**, *25*, 6029.
24. K. H. Choi, S. J. Cho, S. J. Chun, J. T. Yoo, C. K. Lee, W. Kim, Q. Wu, S. B. Park, D. H. Choi, S. Y. Lee, S. Y. Lee, *Nano Lett.* **2014**, *14*, 5677.
25. H. Zhang, P. V. Braun, *Nano Lett.* **2012**, *12*, 2778.
26. N. Ding, J. Xu, Y. X. Yao, G. Wegner, X. Fang, C. H. Chen, I. Lieberwirth, *Solid State Ionics* **2009**, *180*, 222.
27. B. Ahmad, N. Ahmad, A. Saeed, N. Islam, *J. Chem. Soc. Pak.* **1995**, *17*, 7.
28. T.-S. Wei, F. Y. Fan, A. Helal, K. C. Smith, G. H. McKinley, Y.-M. Chiang, J. A. Lewis, *Adv. Energy Mater.* **2015**, *5*, 1500535.
29. A. M. De Ilarduya, J. Iruin, M. Fernandez-Berridi, *Macromolecules* **1995**, *28*, 3707.
30. J.-M. Kim, J.-H. Park, C. K. Lee, S.-Y. Lee, *Sci. Rep.* **2014**, *4*, 4602.
31. C. Zhan, J. Lu, A. J. Kropf, T. Wu, A. N. Jansen, Y.-K. Sun, X. Qiu, K. Amine, *Nature Comm.* **2013**, *4*.
32. J.-M. Kim, C. Kim, S. Yoo, J.-H. Kim, J.-H. Kim, J.-M. Lim, S. Park, S.-Y. Lee, *J. Mater. Chem. A* **2015**, *3*, 10687.

33. H. Zhang, S. Jing, Y. Hu, H. Jiang, C. Li, *J. Power Sources* **2016**, 307, 214.
34. R. V. Salvatierra, A. R. O. Raji, S. K. Lee, Y. Ji, L. Li, J. M. Tour, *Adv. Energy Mater.* **2016**, 6, 1600918.
35. R. A. DiLeo, M. J. Ganter, M. N. Thone, M. W. Forney, J. W. Staub, R. E. Rogers, B. J. Landi, *Nano Energy* **2013**, 2, 268.
36. Y. S. Kim, G. Shoorideh, Y. Zhmayev, J. Lee, Z. Li, B. Patel, S. Chakrapani, J. H. Park, S. Lee, Y. L. Joo, *Nano Energy* **2015**, 16, 446.
37. USCAR, USABC EV Battery Goals, [http://www.uscar.org/guest/article\\_view.php?articles\\_id=85](http://www.uscar.org/guest/article_view.php?articles_id=85).

\* Chapter 2.2 is reproduced in with a permission of “Ju-Myung Kim<sup>†</sup>, Jeong A. Kim<sup>†</sup>, Seung-Hyeok Kim, In Sung Uhm, Sung Joong Kang, Guntae Kim, Sun-Young Lee, Sun-Hwa Yeon, and Sang-Young Lee, All-Nanomat Lithium-Ion Batteries: A New Cell Architecture Platform for Ultrahigh Energy Density and Mechanical Flexibility, *Adv. Energy Mater.* 7, 1701099 (2017)”. Copyright © 2017 John Wiley & Sons, Inc.

## 2.3 Carbon nanotube-cored cobalt porphyrin as a one-dimensional nanohybrid strategy for high-performance lithium-ion battery anodes

### 2.3.1 Introduction

Recently, redox-active organic electrode materials have drawn significant attention as an emerging alternative to currently widespread inorganic (or metal)-based counterparts due to their diversity in molecular-level structural design, solution processability, light weight, flexibility, and environmental benignity.<sup>[1,2]</sup> However, the electrically insulating nature, limited specific capacity, and poor electrochemical durability of these materials have posed formidable obstacles to practical applications. Among the various approaches to resolve the aforementioned problems, combinations of electroconductive nanocarbons (*e.g.*, carbon nanotubes (CNTs), graphenes, and so on) have been extensively investigated due to their beneficial effect on electron conduction and electrolyte accessibility of the organic electrode materials.<sup>[3-15]</sup> Most of these approaches, however, have been devoted to organic cathode materials development (such as organic/carbon composites based on conjugated carbonyls,<sup>[3-9]</sup> free-radicals,<sup>[10,11]</sup> and conducting polymers<sup>[12,13]</sup>). By contrast, few studies have been reported for organic anode materials, which include covalent organic frameworks (COFs) on CNTs<sup>[14]</sup> and lithium terephthalate/graphene composites.<sup>[15]</sup> Furthermore, the mixing of organic materials with nanocarbons is complicated due to their poor compatibility and thus often requires the use of surfactants or pre-/post-treatment steps to achieve a good dispersion state.<sup>[7-10,12]</sup> From the analysis of previous studies, we witness that the rational design of organic anode materials, which can afford reliable/sustainable electrochemical performance and benign affinity with nanocarbons, is needed to achieve high-performance organic/carbon composite materials.

Here, we demonstrate a new class of multi-walled carbon nanotube (MWCNT)-cored, *meso*-tetrakis(4-carboxyphenyl)porphyrinato cobalt (CoTCPP) as a one-dimensional (1D) nanohybrid (denoted as a CC-nanohybrid) for potential use in advanced LIB anodes. CoTCPP, which is one of the metalloporphyrins having multielectron redox activities,<sup>[16-18]</sup> is explored as an organic anode material that can provide lithiation/delithiation in a voltage range of 0.0–3.0 V (vs. Li/Li<sup>+</sup>). In addition, CoTCPP, driven by its extensively conjugated  $\pi$ -bonds, shows a good affinity for the MWCNTs *via* strong noncovalent (*i.e.*,  $\pi$ - $\pi$  and van der Waals) interactions,<sup>[19-24]</sup> which plays a viable role in the formation of the CC-nanohybrids. Benefiting from the chemical/structural uniqueness described above, the CC-nanohybrids allow fast electron transport and easy accessibility of liquid electrolytes, thereby improving their redox kinetics. To the best of our knowledge, this is the first study to report metalloporphyrin/carbon nanohybrids for LIB anodes.

Moreover, intrigued by the 1D structure of the CC-nanohybrid, all-fibrous nanomat anode sheets are

fabricated through concurrent electrospraying/electrospinning processes. The resulting nanomat anode sheets, which are characterized with a heavy metallic foil current collector-free and all-fibrous network architecture, shows fast lithiation/delithiation kinetics due to highly developed three-dimensional (3D) bicontinuous ion/electron conduction pathways, eventually enabling well-distinguishable lithiation behavior (identified by theoretical calculations) of CoTCPP. More notably, the nanomat anode sheets provide exceptional electrochemical performance ( $183 \text{ Wh kg}_{\text{anode}}^{-1}$  at  $3657 \text{ W kg}_{\text{anode}}^{-1}$  and  $>1500$  cycles at fast lithiation/delithiation current densities of  $5.0 \text{ C}/5.0 \text{ C}$ ) and mechanical flexibility that far exceed those attainable with conventional LIB anode technologies.

## 2.3.2 Experimental section

### 2.3.2.1 Synthesis of CoTCPP

960 mg (= 3.85 mmol) of  $\text{Co}(\text{OAc})_2 \cdot 4\text{H}_2\text{O}$  (Sigma Aldrich) and 300 mg (= 0.379 mmol) of *meso*-tetrakis(4-carboxyphenyl)porphyrin (TCPP, TCI Chemicals) was dissolved in 60 mL of dimethylformamide (DMF) and refluxed for 12 h. Subsequently, 150 mL of 1 M aqueous HCl solution was added to the mixture solution, resulting in the precipitation of the powders. The obtained powders were extracted with 150 mL of 0.1 M aqueous NaOH solution and then filtered through Celite. 100 mL of 1 M aqueous HCl solution was added into the resulting solution to produce the reddish-purple precipitates of CoTCPP. After being washed with distilled water and vacuum-dried, the CoTCPP powders (222 mg (= 0.261 mmol)) were obtained.

Ultraviolet–visible–near (UV–vis–NIR) (aqueous NaOH solution):  $\lambda_{\text{max}}/\text{nm}$  ( $\epsilon/\text{M}^{-1}\text{cm}^{-1}$ ) 429 (197500), 546 (12200), 583 (5500). FT-IR (KBr):  $\nu/\text{cm}^{-1}$  3429, 3068, 1703, 1606, 1406, 1005. ICP-MS calcd. for Co: 6.94 wt%, found: 7.08 wt%.

### 2.3.2.2 Dispersion of the MWCNTs in aqueous solutions with various dispersing agents

The above-synthesized CoTCPP was explored as a dispersing agent of the MWCNTs. Meanwhile, typical surfactants for CNTs (such as sodium dodecyl sulfate (SDS, Sigma Aldrich)) and conventional multi-ring aromatic electrode compounds (1,4,5,8-naphthalenetetracarboxylic dianhydride (NTCDA) and perylene-3,4,9,10-tetracarboxylic dianhydride (PTCDA) (both from Sigma Aldrich)) were examined as the control samples of the MWCNT-dispersing agents. These dispersing agents (20 mg) were completely dissolved in 10 mL of distilled water (in the case of SDS) or aqueous NaOH solutions. Specifically, CoTCPP and NTCDA were dissolved in 10 mL of 0.01 M NaOH solution, and PTCDA was added in 10 mL of a 0.1 M NaOH solution. 10 mg of MWCNTs (Nanocyl, carbon purity  $>95 \text{ wt}\%$ )

was added to each solution, and the solution was sonicated for 5 h at room temperature. To obtain supernatants for UV–vis–NIR absorption and fluorescence measurements, the resulting dispersions were centrifuged (at 10000 g for 1 h). Then, 0.5 mL of the supernatants were added to 9.5 mL of distilled water (for a sample of SDS) or aqueous NaOH solutions (for samples of CoTCPP, NTCDA, and PTCDA).

### 2.3.2.3 Preparation of the CC-nanohybrids

The MWCNTs (25 mg) were added into an aqueous NaOH solution (0.01 M, 25 mL) containing CoTCPP (50 mg). The mixture solution was sonicated for 5 h at room temperature, leading to a uniform CoTCPP/MWCNT suspension. The slow addition of the resulting suspension into the 0.1 M aqueous HCl solution (100 mL) with vigorous stirring yielded reddish-purple precipitates. After filtration, washing, and vacuum drying, the CC-nanohybrid powders were obtained.

### 2.3.2.4 Fabrication of the slurry-cast and nanomat CC-nanohybrid anode sheets

Two different types (conventional slurry-cast vs. nanomat) of CC-nanohybrid anode sheets were fabricated. The slurry-cast, CC-nanohybrid anode sheets were prepared by casting an electrode mixture slurry (CC-nanohybrid/carbon black/ carboxyl methyl cellulose (CMC) = 50/37.5/12.5 (w/w/w)) onto a copper (Cu) foil current collector. The metallic foil current collector-free, nanomat CC-nanohybrid anode sheets were fabricated through the concurrent electrospaying (for CC-nanohybrids and SWCNTs (TUBALL, carbon purity >85 wt%))/electrospinning (for PAN) processes. The CC-nanohybrid/SWCNT mixture suspension and PAN solution (10 wt% PAN in DMF) were respectively subjected to electrospaying (10 kV with a feed rate of 5  $\mu\text{L min}^{-1}$ ) and electrospinning (16 kV with a feed rate of 200  $\mu\text{L min}^{-1}$ ) through different nozzles. After roll-pressing at room temperature, the self-standing nanomat CC-nanohybrid anode sheets were obtained.

### 2.3.2.5 Physicochemical and structural characterization

Fourier transform infrared (FT-IR), UV–vis–NIR absorption, and fluorescence spectra were recorded on a Varian 670-IR Spectrometer, an Agilent Cary 5000 UV–vis–NIR Spectrophotometer (cell length = 1.0 mm), and an Edinburgh Instruments FLS920 Fluorescence Spectrometer ( $\lambda_{\text{ex}} = 500 \text{ nm}$ ), respectively. Atomic force microscopy (AFM) images were obtained using a Veeco Multimode V Scanning Probe Microscope. Inductively coupled plasma mass spectrometry (ICP-MS) analyses (Perkin Elmer ELAN DRC-II) were conducted to quantitatively analyze the amount of Co included in the CoTCPP, CC-

nanohybrid, and nanomat CC-nanohybrid anode. The morphological characterization was conducted using a field emission scanning electron microscope (FE-SEM, Hitachi S-4800 and FEI Nova NanoSEM 230) and Transmission electron microscopy (TEM, JEOL JEM-2100F). Raman spectra of the CoTCPP, MWCNTs, and CC-nanohybrids were recorded by a WITec alpha 300R Confocal Raman Imaging Microscope equipped with an Nd–YAG laser ( $\lambda_{\text{ex}} = 532 \text{ nm}$ ). X-ray photoelectron spectroscopy (XPS, Thermo Fisher K-alpha Spectrometer) was used to identify the chemical composition of the CC-nanohybrid. Electronic conductivities were measured using a four-point probe technique (Advanced Instrument Tech CMT-SR1000N). The electrolyte wettability of the slurry-cast and nanomat anode sheets was evaluated by measuring the height of the electrolyte immersion. Mechanical bending tests were conducted under a quantitatively longitudinal compression cycle (bending radius = 5 mm, deformation rate =  $200 \text{ mm min}^{-1}$ ) with a universal testing machine (Petrol LAB DA01). The change in the electronic resistance during the bending tests was investigated by a potentiostat/galvanostat (Bio-Logic VSP classic).

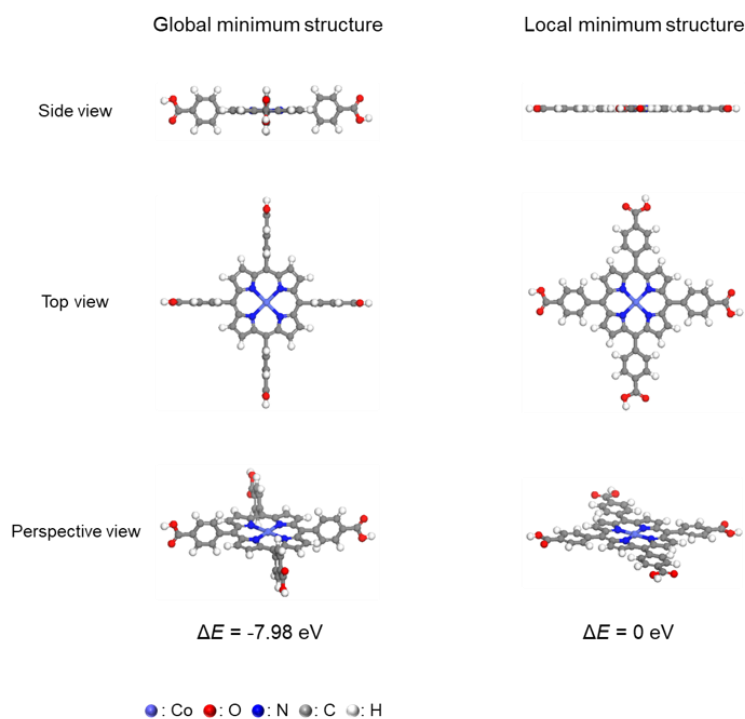


**Figure 2.55** Global minimum (left) and local minimum (right) structures of CoTCPP. The energy difference ( $\Delta E = E_X - E_{\text{local minimum}}$ , X = global minimum or local minimum) was calculated to be  $-7.98 \text{ eV}$ .

### 2.3.2.6 Electrochemical characterization

The electrochemical performance of the CoTCPP (or CC-nanohybrid) anodes were characterized using

a 2032-type coin half-cell (CoTCPP (or CC-nanohybrid) anode/PE separator (thickness = 20  $\mu\text{m}$ , Toray-tonen)/Li metal, 1 M  $\text{LiPF}_6$  in EC/DEC = 1/1 (v/v)). The assembly of all the cells was carried out in an argon-filled glove box. The CV profiles of the cells were obtained using a potentiostat/galvanostat (Bio-Logic VSP classic). The  $dQ/dV$  analyses were performed using a cycle tester (Wonatech WBCS3000). The lithiation/delithiation performance of the cells was investigated using a cycle tester (PNE Solution) under various lithiation/delithiation conditions.

### 2.3.2.7 Theoretical model systems

The global minimum structure of an isolated CoTCPP was determined to have carboxyphenyl groups perpendicular to the Co porphyrin plane (Figure 2.55). The intermolecular interaction of CoTCPP was investigated with both eclipsed and staggered configurations (Figure 2.56). For the CNT models, three types of curved zigzag nanoribbons with varied curvatures of which the edges were passivated by hydrogen atoms were constructed (denoted as c-ZZNR, Figure x). Note that these models underwent geometry optimization and consisted of the same number of atoms (*i.e.*, 216 carbon and 18 hydrogen atoms). The vacuum region was introduced (*i.e.*,  $x = 50 \text{ \AA}$ ,  $z = 50 \text{ \AA}$ ) to avoid interactions among the c-ZZNR systems.

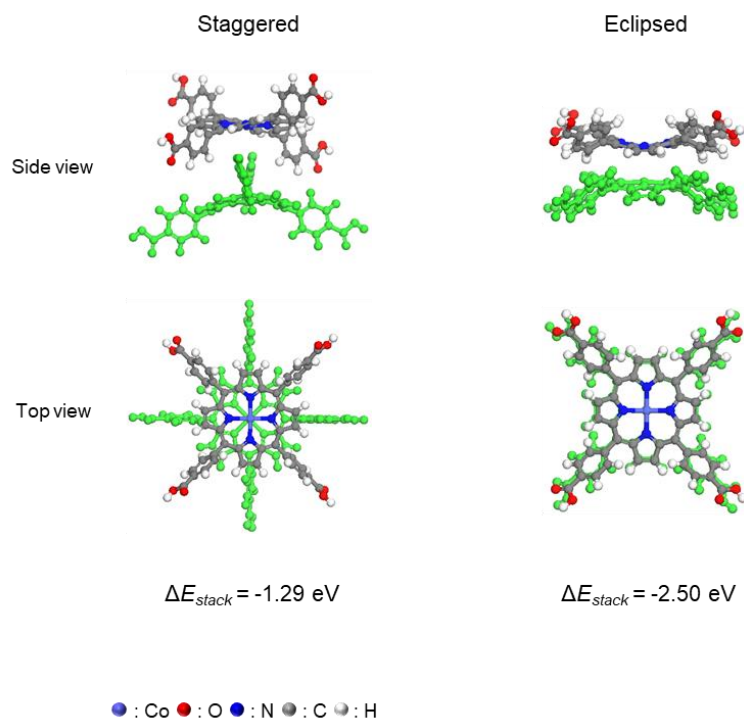


**Figure 2.56** DFT-optimized staggered and eclipsed configurations of CoTCPP, along with the calculated stacking energies ( $\Delta E_{stack}$ ). The CoTCPP molecules at the bottom are green-colored.

*Calculation details:* All DFT calculations were carried out using the DMol<sup>3</sup> program.<sup>[25,26]</sup> The generalized gradient approximation (GGA) with the Perdew-Burke-Ernzerhof (PBE) functional was used for the exchange-correlation energy.<sup>[27]</sup> The spin-polarized calculations were performed with the basis set of DNP 4.4, therein the DFT semi-core pseudopotential (DSPP) was also employed for the core-electron treatment with a smearing value of 0.005 Ha. The semi-empirical Tkatchenko-Scheffler (TS) scheme was included for the dispersion correction.<sup>[28]</sup> The Monkhorst-Pack grid was applied as the  $\Gamma$ -point for all model systems.<sup>[29]</sup> The convergence criteria for the geometry optimization were set to  $1.0 \times 10^{-5}$  Ha for energy, 0.002 Ha/Å for force, and 0.005 Å for displacement. The self-consistent field convergence for the single point energy calculation was set to  $1.0 \times 10^{-6}$  Ha. For the density of states (DOS) calculation, the smearing width was set to 0.05 eV. The atomic charges were obtained by the Mulliken population analysis.<sup>[30]</sup> The stacking energy ( $\Delta E_{stack}$ ) was calculated as follows,

$$\Delta E_{stack} = E_{CoTCPP+X} - E_{CoTCPP} - E_X \quad (X = CoTCPP, c-ZZNR) \quad (1)$$

where  $E_{CoTCPP+X}$  is the total energy of CoTCPP stacked on the other CoTCPP (or c-ZZNR),  $E_{CoTCPP}$  is the total energy of an isolated CoTCPP, and  $E_X$  is the total energy of the counterpart (*i.e.*, the other isolated CoTCPP or c-ZZNR).

The theoretical lithiation voltage ( $V_{Li}$ ) of each stage, during which  $n_2$  Li atoms were inserted into CoTCPP containing  $n_1$  Li atoms, was calculated as follows,<sup>[31]</sup>

$$V_{Li} = - (E_{CoTCPP+(n_1+n_2)Li} - E_{CoTCPP+n_1Li} - n_2 E_{Li}) / n_2 \quad (2)$$

where  $E_{CoTCPP+(n_1+n_2)Li}$  is the total energy of CoTCPP containing  $(n_1+n_2)$  Li atoms,  $E_{CoTCPP+n_1Li}$  is the total energy of CoTCPP containing  $n_1$  Li atoms, and  $E_{Li}$  is the atomic energy of an isolated Li atoms.

### 2.3.3 Result and discussion

#### 2.3.3.1 Preparation and structural characterization of the CC-nanohybrids

The stepwise preparation of the CC-nanohybrids is schematically illustrated in Figure 2.57, along with photographs of the products obtained at each step. CoTCPP, a key component of the CC-nanohybrids, was synthesized by reacting TCPP with  $\text{Co}(\text{OAc})_2 \cdot 4\text{H}_2\text{O}$ , based on previously reported methods.<sup>[24,32]</sup>

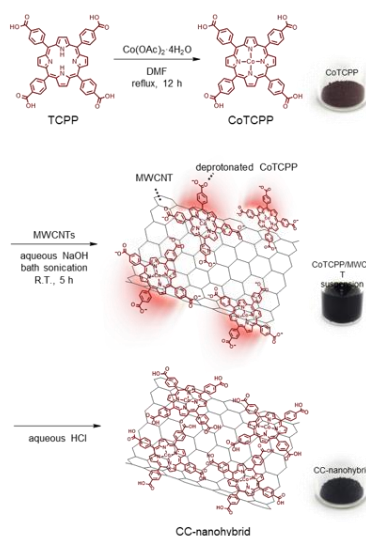


**Figure 2.57** Schematic representation depicting the stepwise preparation of the CC-nanohybrids along with photographs of the products obtained at each step.

The successful synthesis of CoTCPP was verified by analyzing its characteristic UV–vis–NIR absorption and FT-IR spectra (Figure 2.58), and quantitatively estimating its Co content with ICP-MS, Table 2.2. Subsequently, MWCNTs were added into the CoTCPP solution (*i.e.*, CoTCPP in an aqueous NaOH solution), and then the mixture was subjected to sonication, resulting in a reddish-black suspension.

Sample	Amt of Co [wt%]	Amt of CoTCPP [wt%]	Amt of CC-nanohybrids [wt%]
CoTCPP	7.08		
CC-nanohybrids	4.24	59.9	
Nanomat anode	2.02	28.5	47.6

**Table 2.2** Quantitative analysis (estimated from ICP-MS) of the component contents in various samples

The dispersion state of the MWCNTs in the CoTCPP solution was investigated. The AFM image (Figure

2.59) showed well-dispersed, individualized fibrous morphology. The good dispersion of the MWCNTs and their noncovalent interactions with the CoTCPP were further elucidated by UV-vis-NIR absorption spectroscopy (Figure 2.60a). The reddish-black suspension was centrifuged, and the supernatant was selectively collected for this analysis. The absorption spectrum (red line) of the pristine CoTCPP in the NaOH solution showed the Soret at 429 nm and two Q-bands at 546/583 nm without appreciable NIR absorption.<sup>[24,33]</sup> Meanwhile, the spectrum (blue line) of the CoTCPP/MWCNT supernatant provided a wide range of absorption, including the characteristic bands assigned to CoTCPP. The broad absorption that gradually decreases from UV to NIR region is possibly attributed to the MWCNTs, which is verified by the spectrum (black line) of a control sample containing a typical surfactant SDS. Note that the characteristic absorption band at 639 nm was exclusively observed in the CoTCPP/MWCNT supernatant (not in the pristine CoTCPP solution and SDS/MWCNT supernatant), exhibiting a redshift in the Q-bands due to the altered electronic structure<sup>[20]</sup> of the CNT-bound CoTCPP. In addition, fluorescence quenching was observed in the CoTCPP/MWCNT supernatant (Figure 2.60b), which may result from energy transfer<sup>[19-21]</sup> from CoTCPP to MWCNTs. These spectroscopic results demonstrate the presence of strong noncovalent interactions between CoTCPP and MWCNTs.

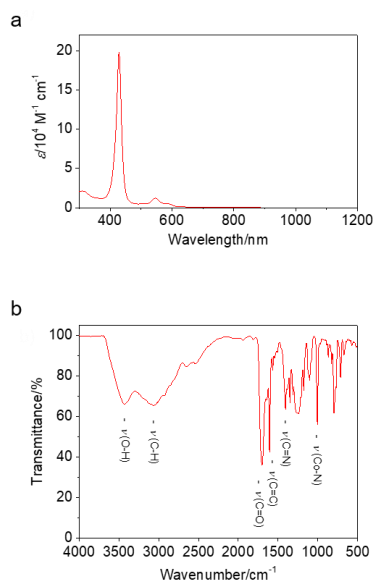


**Figure 2.58** (a) UV-vis-NIR absorption and (b) FT-IR spectra of CoTCPP.

To further clarify the exceptional affinity of CoTCPP for MWCNTs, a control experiment was conducted with NTCDA and PTCDA,<sup>[34]</sup> which were reported as organic anode materials having smaller aromatic units than CoTCPP. Mixing NTCDA (or PTCDA) with the MWCNTs resulted in a very poor dispersion state (Figures 2.60c), verifying the important role of the aromatic rings in the affinity with MWCNTs.

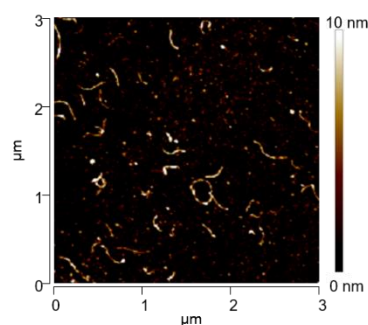


**Figure 2.59** AFM image of CoTCPP/MWCNT suspension casted on a mica substrate.

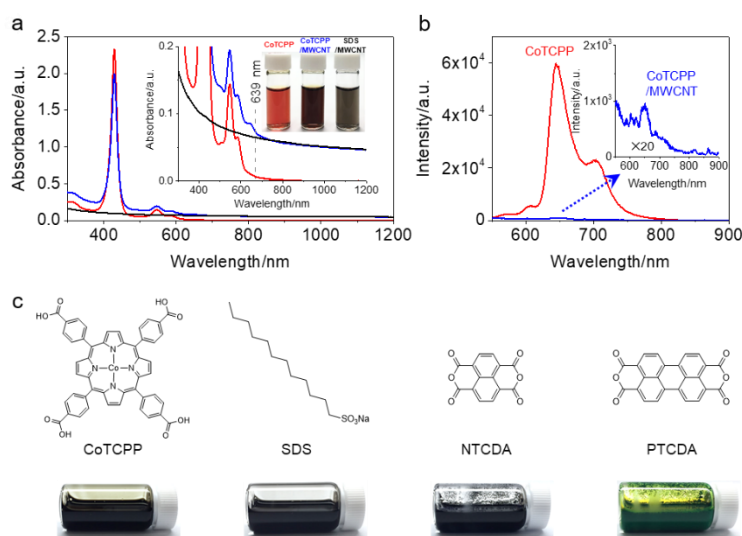


**Figure 2.60** (a) UV–vis–NIR absorption spectra of CoTCPP in aqueous NaOH solution (red line) and supernatant solutions (prepared from CoTCPP/MWCNT (blue line) and SDS/MWCNT suspensions (black line)). The photographs of the corresponding solutions are also displayed. (b) Fluorescence spectra of CoTCPP in aqueous NaOH solution (red line) and supernatant solution from CoTCPP/MWCNT suspension (blue line). (c) Photographs of aqueous MWCNT suspensions prepared with various dispersing agents.

A theoretical study on the stacking behavior of CoTCPP on CNT surfaces was performed by density functional theory (DFT) calculations. As models of the outermost shell of CNT, three types of curved zigzag nanoribbons with varied curvature (denoted as c-ZZNR-16 for (16,16) CNT, c-ZZNR-20 for (20,20) CNT, and c-ZZNR-30 for (30,30) CNT, respectively) were constructed (Figure 2.61a). The stability of the various stacking configurations was evaluated by calculating their stacking energies ( $\Delta E_{stack}$ , see Calculation details in the Experimental section). In regard to the intermolecular interaction of CoTCPP (Figure 2.61b, red columns), the eclipsed configuration ( $\Delta E_{stack} = -2.50$  eV) was estimated to be more stable than the staggered configuration ( $\Delta E_{stack} = -1.29$  eV) (see also Figure 2.56). Notably, considerably increased stacking energies were obtained for the stacking configurations between the

CoTCPP and c-ZZNR systems ( $\Delta E_{stack} = -5.81$  (for c-ZZNR-16),  $-5.90$  (for c-ZZNR-20), and  $-6.15$  eV (for c-ZZNR-30), respectively; blue columns), indicating the superior thermodynamic stability of CoTCPP stacked on the CNT surface. This result correspondingly supports the good dispersion state of the CoTCPP/MWCNT mixture suspension. Note that the stacking energies tend to slightly increase with the reduced curvature of the c-ZZNR systems, which is possibly due to the enlarged contact between the CoTCPP and c-ZZNR systems. In addition, a negligible electron transfer ( $<0.05$  e) between the CoTCPP and c-ZZNR systems was observed, indicating that the stacking of CoTCPP on the CNT surface proceeds *via* noncovalent interactions, not by covalent bonding.

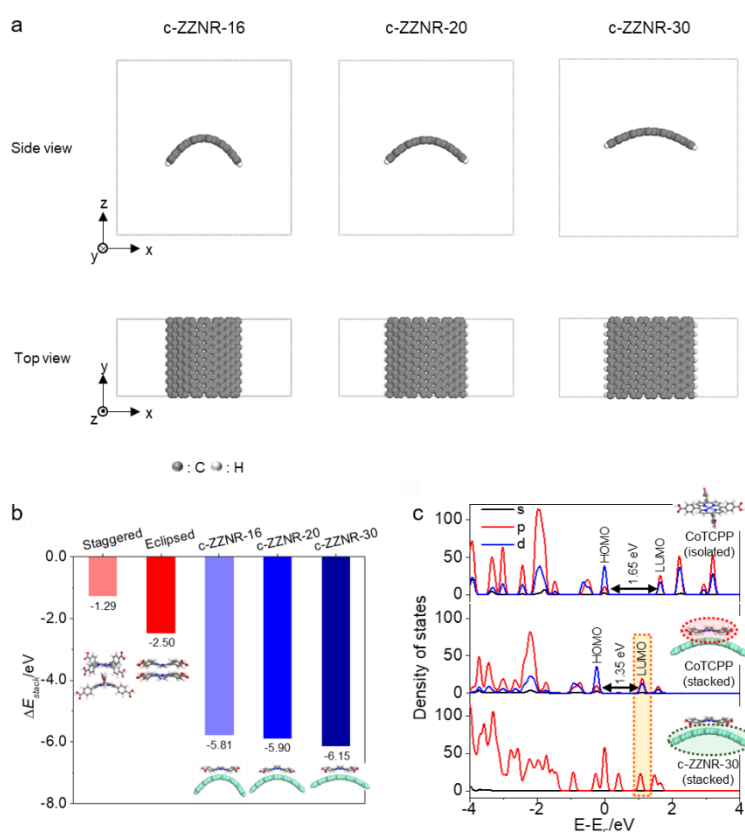


**Figure 2.61** (a) DFT-optimized structures of c-ZZNR-16, c-ZZNR-20, and c-ZZNR-30, (b) Stacking energies ( $\Delta E_{stack}$ ) calculated for the staggered/eclipsed configurations of CoTCPP (red columns) and the stacking configurations between CoTCPP and c-ZZNR systems (blue columns). (c) PDOS of CoTCPP (top: isolated, middle: stacked on c-ZZNR-30) and c-ZZNR-30 stacked with CoTCPP (bottom). EF is the Fermi energy.

The change in the electronic structure of CoTCPP was investigated by the partial density of states (PDOS) analysis (Figure 2.61c). The energy gap between highest occupied molecular orbital (HOMO) and lowest unoccupied molecular orbital (LUMO) levels of an isolated CoTCPP molecule was estimated to be  $\sim 1.65$  eV (top). Meanwhile, the LUMO of CoTCPP stacked on c-ZZNR-30 showed an appreciable downshift in its energy level, which overlapped with the conduction band of c-ZZNR-30

(middle and bottom). This downshift of LUMO level induced a decrease in the energy gap of CoTCPP by  $\sim 0.3$  eV, which could be responsible for the aforementioned redshift of the Q-bands observed in the absorption spectrum (*vide supra*: Figure 2.60a).

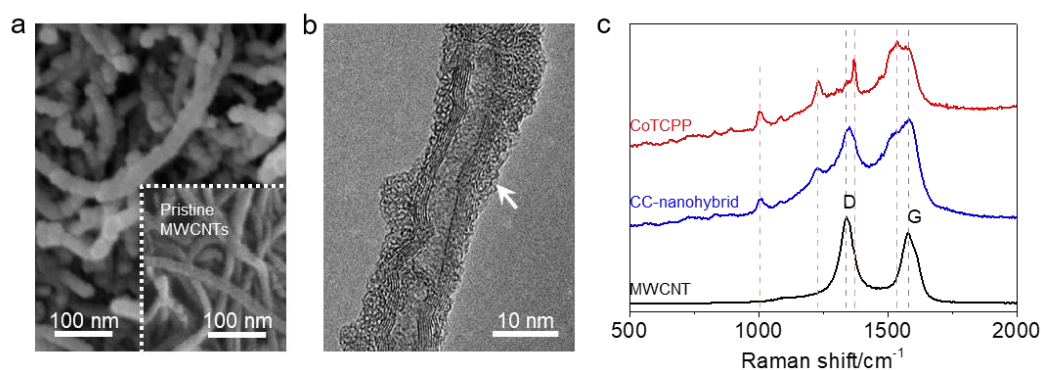


**Figure 2.62** (a) SEM image (inset: pristine MWCNTs) and (b) TEM image of CC-nanohybrids. The arrow indicates the CoTCPP shell layer. Raman spectra of CoTCPP (red line), CC-nanohybrids (blue line), and MWCNTs (black line).

The slow addition of the CoTCPP/MWCNT mixture suspension into an aqueous HCl solution allowed the precipitation and deposition of CoTCPP onto the MWCNT surface, resulting in the formation of the CC-nanohybrids. The CoTCPP content in the CC-nanohybrids was estimated to be 59.9 wt% from the ICP-MS analysis (Table 2.2). The obtained CC-nanohybrids showed rugged surface morphology with a slightly thickened diameter compared to the pristine MWCNTs (Figure 2.62a), revealing the conformal deposition of the CoTCPP thin layers on the MWCNT surface. This unique morphology was verified by TEM, Figure 2.62b. The MWCNT surface was uniformly wrapped with nanothick CoTCPP layers.

Spectral region	Binding energy [eV]	Assignment
C <sub>1s</sub>	284.2	C–C, C=C, C–H
	286.7	C–OH, C–N (C=N)
	288.5	C=O
	290.8	$\pi$ - $\pi^*$
N <sub>1s</sub>	398.1	N–Co
	400.9	N–C (N=C)
O <sub>1s</sub>	531.4	O=C
	533.0	HO–C
Co <sub>2p</sub>	779.9	Co–N
	795.2	

**Table 2.3** Spectral band assignment of key elements in CC-nanohybrids (from XPS analysis)

The structural uniqueness of the CC-nanohybrids was further elucidated using Raman and XPS methods. The Raman spectrum (Figure 2.62c, blue line) of the CC-nanohybrids showed the overlapped characteristic peaks that were assigned to CoTCPP (red line) and MWCNTs (black line). The wide-scan XPS spectrum (Figure S8, Supporting Information) of the CC-nanohybrids showed the characteristic bands at binding energies of 284.2–290.8 (for C<sub>1s</sub>), 398.1–400.9 (for N<sub>1s</sub>), 531.4–533.0 (for O<sub>1s</sub>), and 779.9–795.2 eV (for Co<sub>2p</sub>), confirming the presence of carbon, nitrogen, oxygen, and cobalt in the CC-nanohybrids. The assignments for an existential form of the chemical bonds are provided in Table 2.3.

### 2.3.3.2 Electrochemical Superiority of the CC-nanohybrids over Pristine CoTCPP

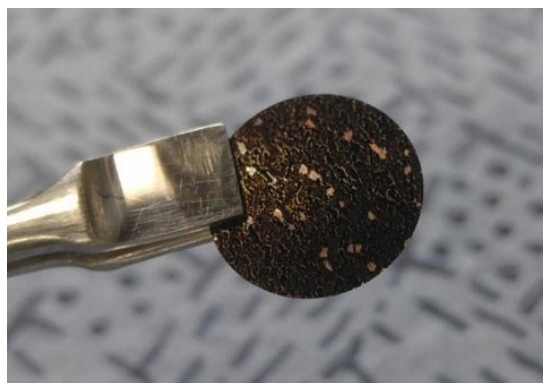


**Figure 2.63** Photograph of slurry-cast anode containing MWCNT additives (weight-based composition ratio: CoTCPP/MWCNT/carbon black/CMC = 30/20/37.5/12.5). The resulting anode showed the structural disruption due to the poor dispersion state of the MWCNTs.

The effect of the structural uniqueness (*i.e.*, MWCNT-cored CoTCPP) of the CC-nanohybrid on the electrochemical performance was investigated by comparing the rate capability between the CC-nanohybrid and pristine CoTCPP. For this measurement, a coin (2032-type) half-cell (CC-nanohybrid anode/polyethylene (PE) separator/Li metal counter electrode, 1 M LiPF<sub>6</sub> in ethylene carbonate/diethyl carbonate (EC/DEC) = 1/1 (v/v)) was used, in which the CC-nanohybrid anode consisted of CC-nanohybrid/carbon black conductive additive/ CMC binder (= 50/37.5/12.5 (w/w/w)) on a Cu foil current collector. Meanwhile, as a control sample, a pristine CoTCPP anode (pristine CoTCPP/carbon black/CMC = 30/57.5/12.5 (w/w/w)) was prepared. Here, considering that the CC-nanohybrid already contains MWCNTs as a core element, additional carbon black additives were introduced to produce a total carbon content equal to that of the CC-nanohybrid anode. When MWCNTs were used as a conductive additive instead of carbon black powders, we failed to fabricate a structurally stable CoTCPP anode due to the poor dispersion state of the MWCNTs (Figure 2.63).

The rate capability of the cells was measured under a constant lithiation current density of 0.1 C (150

mA  $g_{\text{CoTCPP}}^{-1}$ ), in which the delithiation current densities varied from 0.1 to 20 C. The lithiation/delithiation profiles (Figure 2.64a) showed sloping curves in a voltage range of 0.0–3.0 V, which appeared similar to the results of organic anode materials bearing redox-active aromatic rings.<sup>[14,35-42]</sup> Both the CC-nanohybrid and pristine CoTCPP anodes showed large delithiation capacities at low delithiation current densities.

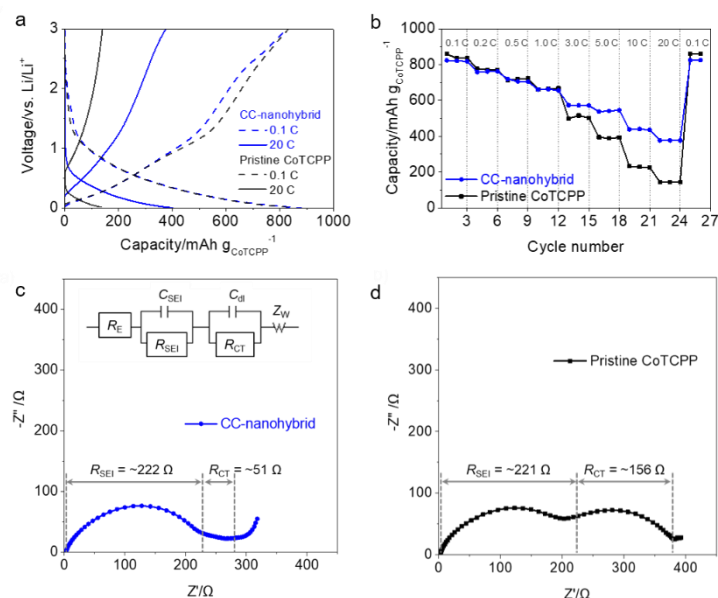


**Figure 2.64** (a) Lithiation/delithiation profiles, in which delithiation current densities varied from 0.1 to 20 C under a constant lithiation current density of 0.1 C. (b) Comparison of delithiation rate capability. EIS spectra of (c) CC-nanohybrid and (d) pristine CoTCPP after the initial lithiation. Inset shows the associated equivalent circuit model.<sup>[ref]</sup>  $R_E$ : electrolyte resistance,  $R_{SEI}$ : solid electrolyte interphase (SEI) resistance,  $R_{CT}$ : charge transfer resistance,  $C_{SEI}$ : SEI capacitance,  $C_{dl}$ : double layer capacitance, and  $Z_W$ : Warburg impedance.

When the delithiation current density was increased, the CC-nanohybrid anode provided a higher delithiation capacity (Figures 2.64b) than the pristine CoTCPP anode. Note that the difference between the two anodes became pronounced at the higher delithiation current densities (e.g., 377 for the CC-nanohybrid anode vs. 144 mA h  $g_{\text{CoTCPP}}^{-1}$  for the pristine CoTCPP anode at a delithiation current density of 20 C). For the pristine CoTCPP powders (their sizes are in the micrometer scale, Figure 2.65), only their surface region may be engaged in the redox reaction at fast current densities, resulting in a poor rate capability. The results of the pristine CoTCPP anode appears similar to those of previously reported organic anode materials,<sup>[14,35-39]</sup> most of which tend to be kinetically sluggish (Table 2.4). The CC-nanohybrids, due to their structural uniqueness (*i.e.*, nanothick CoTCPP layers on the MWCNTs), can facilitate ion diffusion and electron transfer between the CoTCPP and MWCNTs, thereby contributing to the better rate performance. This superior rate kinetics of the CC-nanohybrid was further verified by

conducting electrochemical impedance spectroscopy (EIS) measurements (Figure 2.64c and 2.64d). The analysis of the associated proper equivalent circuit model<sup>[43]</sup> exhibited that the charge transfer resistance ( $R_{CT}$ ) of the CC-nano hybrid anode ( $\sim 51 \Omega$ ) was remarkably lower than that of the pristine CoTCPP anode ( $\sim 156 \Omega$ ), demonstrating the structural benefit of the CC-nano hybrid. Meanwhile, both anodes showed reliable capacity recovery when the delithiation current density returned to 0.1 C after the rate capability tests, indicating the good redox stability of CoTCPP.

Delithiation capacity [mAh g <sub>AM</sub> <sup>-1</sup> ] (Delithiation current density [A g <sub>AM</sub> <sup>-1</sup> ]) <sup>[a]</sup>	Areal mass loading [mg cm <sup>-2</sup> ]	Ref
377 (30.0) <sup>[b]</sup>	1.7	This study
217 (5.0)	1.2	S1
100 (0.5)	–	S2
193 (0.75)	–	S3
203 (9.1)	–	S4
317 <sup>[c]</sup> (11.3)	–	S5
700 (2.5)	–	S6

[a] AM: active material. [b] Corresponding to 20 C. [c] Examined at 50 °C

**Table 2.4** Comparison of delithiation capacities and areal mass loading: CC-nano hybrids vs. previously reported organic anode materials

To highlight the superior performance of the CC-nano hybrid at fast current densities, its capacity retention with cycling (at lithiation/delithiation current densities of 0.1 C/5.0 C) was compared with that of the pristine CoTCPP (Figures 2.66). The CC-nano hybrid anode showed stable capacity retention with cycling, whereas a serious capacity decay (after 150 cycles) was observed at the pristine CoTCPP anode, underscoring the beneficial effect of the CC-nano hybrid on the redox kinetics and sustainability. This unusual redox reaction behavior of the CC-nano hybrids will be further elucidated in our future studies to broaden their application fields.

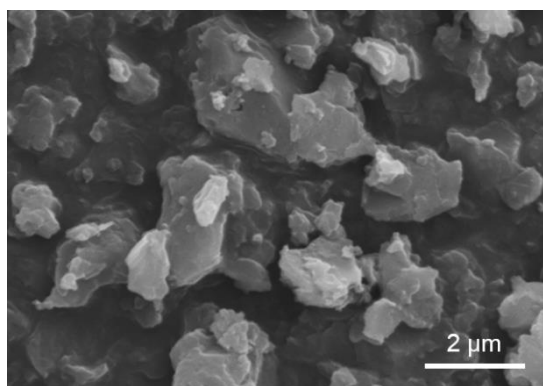


**Figure 2.65** SEM image of CoTCPP powders

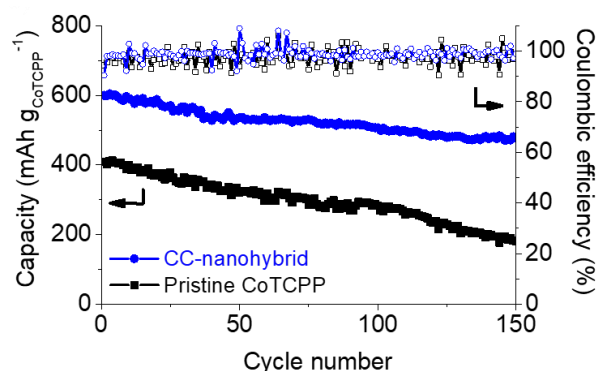


**Figure 2.66** Cycle performance at lithiation/delithiation current densities of 0.1 C/5.0 C.

### 2.3.3.3 Preparation and characterization of all-Fibrous nanomat anode sheets based on CC-nanohybrids

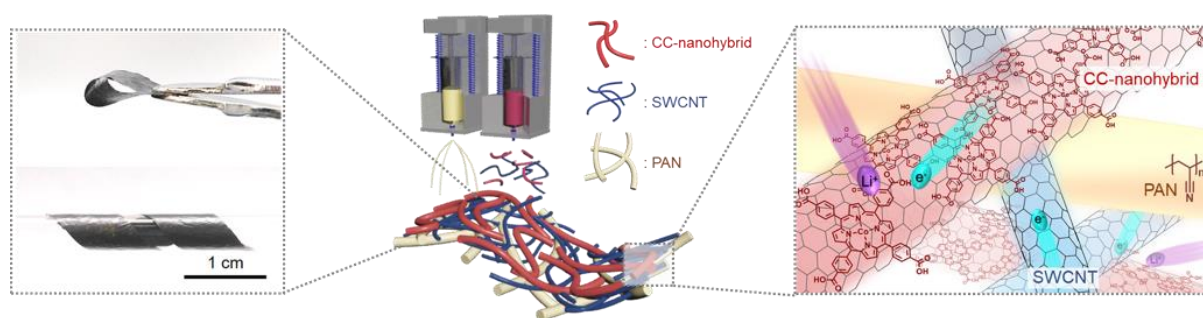
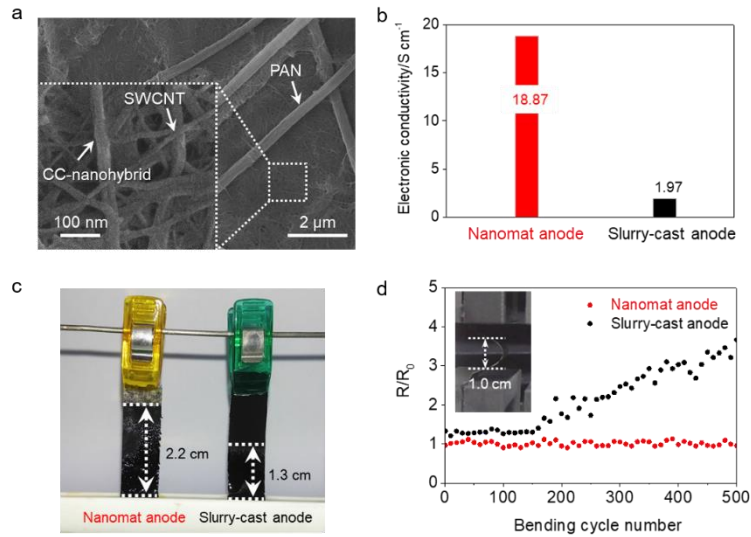


**Figure 2.67** Schematic representation depicting the preparation of the all-fibrous nanomat anode sheet along with its photographs.

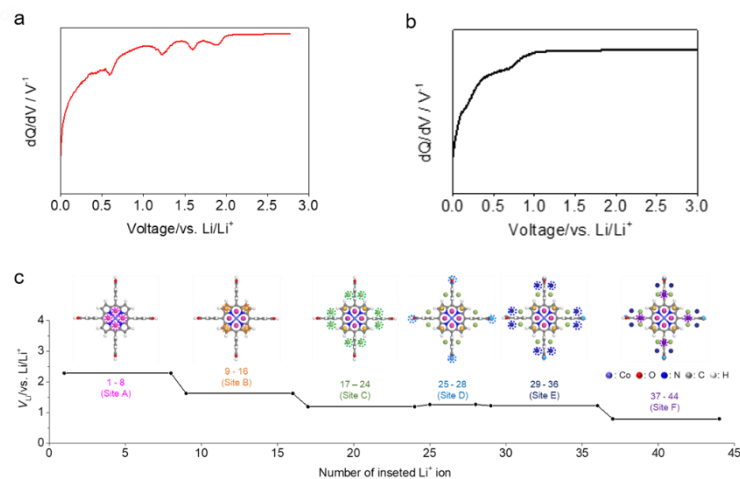
To meet the ever-growing demand for ultrahigh energy/power density, we suggest a new electrode architecture based on the CC-nanohybrids. Intrigued by the 1D structure of the CC-nanohybrids, all-fibrous nanomat anode sheets were fabricated through concurrent electrospinning (for CC-nanohybrids and SWCNTs) and electrospinning (for PAN) processes. The advantageous effects of the nanomat architecture on electrode performance were reported in our previous studies on metal oxide-based cathodes and silicon (Si)-based anodes.<sup>[44,45]</sup> The schematic representation depicting the preparation of the nanomat anode sheet is shown in Figure 2.67, along with its photographs. The SWCNTs and PAN nanofibers in the nanomat anode sheet acted as electron-conduction pathways and a mechanical skeleton, respectively. The amount of the CC-nanohybrid in the nanomat anode sheet was estimated to be 47.6 wt% from the ICP-MS analysis (Table 2.2).

Figure 2.68a shows that the CC-nanohybrids were uniformly intermingled with the highly networked SWCNTs and PAN nanofibers. This all-fibrous morphology of the nanomat anode sheet enabled a

significant improvement in the electronic conductivity and electrolyte accessibility compared to the slurry-cast CC-nanohybrid anode (Figure 2.68b and 2.68c). In addition, the nanomat anode sheet, due to its highly networked fibrous structure, showed the good mechanical flexibility upon the repeated bending deformation (bending radius = 5 mm and deformation rate = 200 mm min<sup>-1</sup>, Figure 2.68d).



**Figure 2.68** (a) SEM image (inset: high-magnification) of the nanomat anode sheet. (b) Electronic conductivity. (c) Photographs showing electrolyte wettability. (d) Change in the electronic resistance of the nanomat (red dots) and slurry-cast (black dots) anode sheets as a function of the longitudinal compression cycle (bending radius = 5 mm, deformation rate = 200 mm min<sup>-1</sup>). Inset shows a photograph of the bent nanomat anode sheet.



**Figure 2.69** dQ/dV plot of the nanomat (a) and slurry-cast (b) anode sheets. (c) Theoretical lithiation voltage ( $V_{Li}$ ) profile and optimized structure (insets) for the stepwise lithiation of CoTCPP, in which newly inserted Li<sup>+</sup> ions at each site are encircled.

The differential capacity ( $dQ/dV$ ) analysis of the nanomat anode sheet exhibited distinct reduction peaks at approximately 1.9, 1.6, 1.2, and 0.6 V (Figure 2.69a), which were not clearly observed at the slurry-cast anode sheet (Figure 2.69b). To better elucidate the intriguing electrochemical behavior of the nanomat anode sheet, the lithium storage behavior of CoTCPP was theoretically investigated.

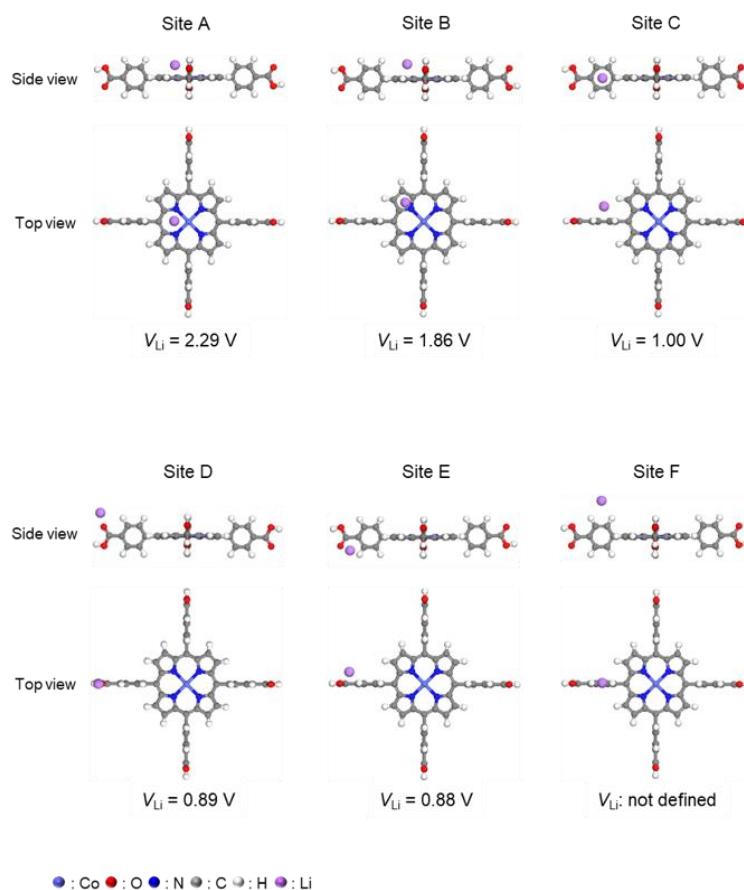


**Figure 2.70** DFT-optimized structures and theoretical lithiation voltages ( $V_{Li}$ ) for investigation of the initial  $Li^+$  ion insertion at various sites of CoTCPP.

First, possible lithiated configurations for the initial  $Li^+$  ion insertion at various sites of CoTCPP (*i.e.*, from sites A to F at the Co porphyrin plane and carboxyphenyl groups) were investigated (Figure 2.70). The theoretical lithiation voltage ( $V_{Li}$ , see Calculation details in the Experimental section) for each configuration was calculated. The  $V_{Li}$  values obtained for the Co porphyrin plane (= 2.29 for site A and 1.86 V for site B) were much higher than those obtained for the carboxyphenyl groups (= 1.00 for site C, 0.89 for site D, and 0.88 V for site E). Note that the  $V_{Li}$  value for site F was not defined because the  $Li^+$  ion migrated to the adjacent and stable site A after the geometry optimization. These results indicate that the electron-rich  $\pi$ -system of the Co porphyrin plane, which is characterized by electrostatic potential fields of CoTCPP (Figure 2.71), exhibits strong cation- $\pi$  interaction with the inserted  $Li^+$  ions.

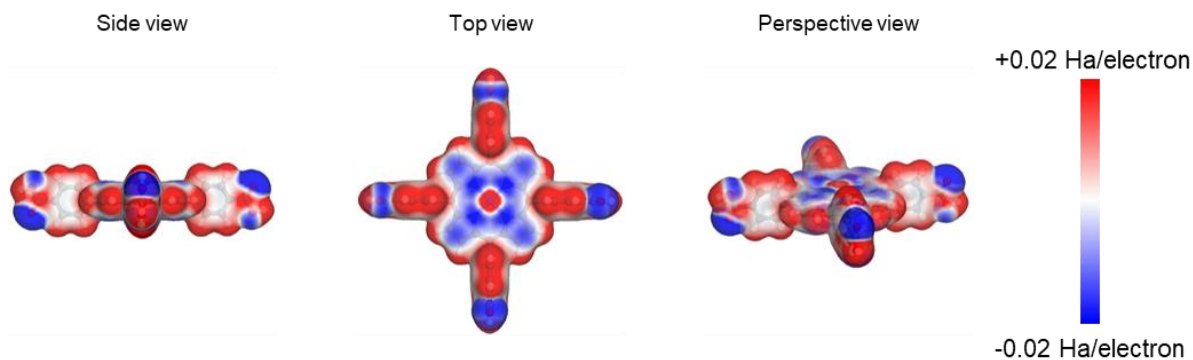


**Figure 2.71** Electrostatic potential fields of CoTCPP. The electron-rich and electron-deficient regions are colored blue and red, respectively.

Meanwhile, the maximum number of  $\text{Li}^+$  ions that can be inserted at each site is expected to follow a multiple of 4 (*i.e.*, 4 or 8) due to the  $D_{4h}$  molecular symmetry of CoTCPP. Accordingly, the optimized structures (Figure 2.69c, insets) for the stepwise lithiation of CoTCPP showed that a total of 44  $\text{Li}^+$  ions (8  $\text{Li}^+$  ions for each site, but 4  $\text{Li}^+$  ions only for site D) can be inserted into a CoTCPP molecule, which starts by lithiation of the Co porphyrin plane (sites A and B), followed by that of the carboxyphenyl groups (sites C, D, E, and F). Note that the whole lithiation process affords a theoretical capacity of  $1612 \text{ mAh g}_{\text{CoTCPP}}^{-1}$ . The  $V_{\text{Li}}$  values of 2.28 (for site A), 1.62 (for site B),  $\sim 1.20$  (for sites C, D, and E), and 0.79 V (for site F) were found for the stepwise lithiation process (Figure 2.69c). The theoretically calculated lithiation voltages appear consistent with the experimental values measured by the dQ/dV analysis (Figure 2.69a and 2.69b). This result demonstrates that the nanomat architecture, which allows bicontinuous electron/ion transport in the anode, can facilitate the redox reaction of CoTCPP and enable its theoretical lithium storage behavior.

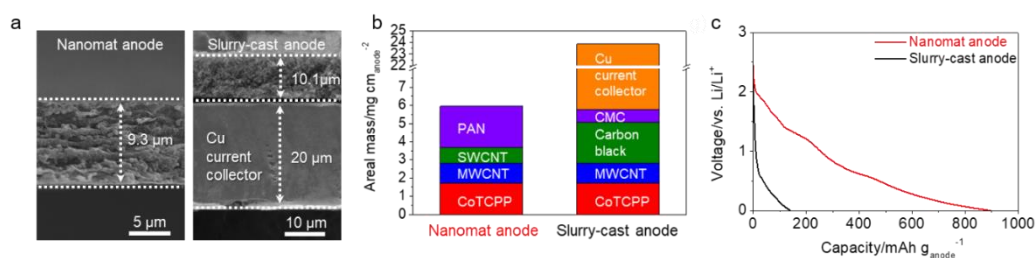


**Figure 2.72** (a) SEM images (cross-sectional) of the nanomat (left) and slurry-cast (right) anode sheets. (b) Comparison of the areal masses [ $\text{mg cm}_{\text{anode}}^{-2}$ ] between the nanomat and slurry-cast anode sheets. (c) Comparison of the lithiation profiles (expressed as capacity per weight of anode sheet ( $\text{mAh g}_{\text{anode}}^{-1}$ )): nanomat (red line) vs. slurry-cast (black line) anode sheets at a current density of 0.05 C.

Another notable feature of the nanomat anode sheet is the removal of the metallic foil (here, Cu foils) current collectors that are essentially used in conventional slurry-cast anode sheets (Figure 2.72a), thereby significantly reducing the areal weight of the nanomat anode sheet (Figure 2.72b). To realize practical application of organic anodes in LIBs, substantial attention should be undoubtedly paid to evaluating *anode sheet weight-based gravimetric capacity* (expressed as  $\text{mAh g}_{\text{anode}}^{-1}$ ) rather than typical gravimetric capacity based on the weight of organic active materials (expressed as  $\text{mAh g}_{\text{AM}}^{-1}$  (AM: active material), herein,  $\text{mAh g}_{\text{CoTCPP}}^{-1}$ ). Note that the nanomat anode sheet presented herein can be suggested as an appealing approach to meet this gravimetric capacity demand, due to its extremely lightweight feature. Figure 2.72c compares the lithiation profiles (measured at a current density of 0.05 C) between the nanomat and the slurry-cast anode sheets, in which the areal mass loadings of CC-nanohybrid were almost identical at both anode sheets. Compared to the slurry-cast anode sheet (black line), a significantly higher gravimetric capacity was observed at the nanomat anode sheet (red line), underscoring the beneficial effect of the metallic foil current collector-free architecture.

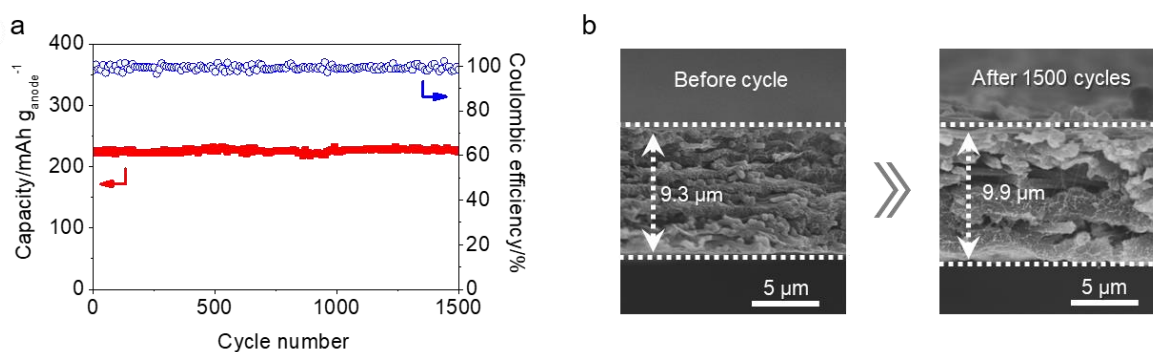


**Figure 2.73** (a) Cycling performance of the nanomat anode sheet at lithiation/delithiation current densities of 5.0 C/5.0 C. (b) Cross-sectional SEM images of nanomat anodes before (left) and after 1500 cycles (right).

The cycling performance of the nanomat anode sheet was examined (Figure 2.73a). Note that the nanomat anode sheet showed highly reversible capacities ( $\sim 226 \text{ mAh g}_{\text{anode}}^{-1}$  (based on the anode sheet weight), corresponding to  $\sim 793 \text{ mAh g}_{\text{CoTCPP}}^{-1}$  (based on the CoTCPP weight)) during 1500 cycles (capacity retention = 99.0%) at considerably fast lithiation/delithiation current densities of 5.0 C/5.0 C. The volume expansion of the nanomat anode sheet after 1500 cycles was approximately 106% (anode thickness = 9.3 (before) and 9.9  $\mu\text{m}$  (after the cycling test), Figure 2.73b), which was remarkably lower than those (in general,  $>300\%$ )<sup>[46-48]</sup> of conventional high-capacity anode sheets such as Si-based ones. The abovementioned electrochemical performance of the nanomat anode sheet was compared with those of previously reported high-capacity LIB anode sheets (Table 2.5). Among the numerous previous studies, metallic current collector-free LIB anode sheets were exclusively chosen to render a fair

comparison with the nanomat anode sheet, including Si/carbon fibrous composites,<sup>[49]</sup> Si/graphene foam-like composites,<sup>[50]</sup> Mn<sub>3</sub>O<sub>4</sub>/graphene composites,<sup>[51]</sup> and Fe<sub>3</sub>O<sub>4</sub>/CNT composites.<sup>[52]</sup> Note that this study showed a substantially higher (anode sheet-based) gravimetric energy density (= 183 Wh kg<sub>anode</sub><sup>-1</sup>) at a higher (anode sheet-based) gravimetric power density (= 3657 W kg<sub>anode</sub><sup>-1</sup>) and exceptional cycling performance, demonstrating that the nanomat anode sheet shown herein holds great promise as an attractive alternative to outperform the previously reported high-capacity LIB anode sheets.

Anode material	Energy density [Wh Kg <sub>anode</sub> <sup>-1</sup> ] (Power density [W Kg <sub>anode</sub> <sup>-1</sup> ])	Cycle number (Current density [A g <sub>AM</sub> <sup>-1</sup> ]) <sup>[a]</sup>	Capacity retention [%]	Ref
Nanomat anode	183 (3657)	1500 (7.5) <sup>[b]</sup>	99.0	This study
Si/carbon fibrous composites	108 (1728)	100 (0.5)	76.4	49
Si/grapheme foam-like composites	104 (1370)	1200 (1.0)	93.0	50
Mn <sub>3</sub> O <sub>4</sub> /graphene composites	157 (1020)	100 (0.1)	87.5	51
Fe <sub>3</sub> O <sub>4</sub> /CNT composites	298 (490)	100 (0.1)	Increased during cycling	52

[a] AM: active material. [b] Corresponding to 5 C.

**Table 2.5** Comparison of electrochemical performances between all-fibrous nanomat anode sheet (this study) and previously reported metallic current collector-free anode sheets

### 2.3.4 Conclusion

In summary, we presented the CC-nanohybrid (*i.e.*, MWCNT-cored CoTCPP) as a new 1D material strategy to develop an advanced LIB anode. Driven by its highly conjugated  $\pi$ -bonds, CoTCPP showed good affinity with MWCNTs via strong noncovalent interactions, resulting in the successful formation of the CC-nanohybrids. The chemical/structural uniqueness of the CC-nanohybrids facilitated electron transfer and electrolyte accessibility, thereby significantly improving the redox kinetics compared to the pristine CoTCPP. Intrigued by the 1D structure of the CC-nanohybrid, the all-fibrous nanomat anode sheets without the metallic current collectors were fabricated using concurrent electrospinning/electrospinning processes. The nanomat anode sheets provided fast lithiation/delithiation kinetics due to the well-developed 3D bicontinuous ion/electron conduction pathways, eventually realizing the well-distinguishable lithiation behavior (elucidated by theoretical calculations) of CoTCPP. More notably, the nanomat anode sheet exhibited exceptional electrochemical performance (183 Wh kg<sub>anode</sub><sup>-1</sup> at 3657 W kg<sub>anode</sub><sup>-1</sup> and >1500 cycles at lithiation/delithiation current densities of 5.0 C/5.0 C) and mechanical flexibility, which far exceeded those attainable with conventional LIB anode technologies (including the currently widespread inorganic (or metal)-based ones). We envision that the CC-nanohybrids and the all-fibrous nanomat anode sheets described herein

offer new insights into the material/architecture design of high-performance organic anodes for next-generation rechargeable power sources beyond current state-of-the-art LIBs.

### 2.3.5 Reference

1. S. Muench, A. Wild, C. Friebe, B. Haupler, T. Janoschka, U. S. Schubert, *Chem. Rev.* **2016**, *116*, 9438.
2. T. B. Schon, B. T. McAllister, P. F. Li, D. S. Seferos, *Chem. Soc. Rev.* **2016**, *45*, 6345.
3. T. Liu, K. C. Kim, B. Lee, Z. Chen, S. Noda, S. S. Jang, S. W. Lee, *Energy Environ. Sci.* **2017**, *10*, 205.
4. A. Jaffe, A. Saldivar Valdes, H. I. Karunadasa, *Chem. Mater.* **2015**, *27*, 3568.
5. M. Lee, J. Hong, H. Kim, H. D. Lim, S. B. Cho, K. Kang, C. B. Park, *Adv. Mater.* **2014**, *26*, 2558.
6. H. Wu, K. Wang, Y. Meng, K. Lu, Z. Wei, *J. Mater. Chem. A* **2013**, *1*, 6366.
7. G. Yang, F. Bu, Y. Huang, Y. Zhang, I. Shakir, Y. Xu, *ChemSusChem* **2017**, *10*, 3419.
8. Y. Lu, Q. Zhao, L. Miao, Z. Tao, Z. Niu, J. Chen, *J. Phys. Chem. C* **2017**, *121*, 14498.
9. H. Wu, Q. Meng, Q. Yang, M. Zhang, K. Lu, Z. Wei, *Adv. Mater.* **2015**, *27*, 6504.
10. W. Guo, Y.-X. Yin, S. Xin, Y.-G. Guo, L.-J. Wan, *Energy Environ. Sci.* **2012**, *5*, 5221.
11. J.-K. Kim, J. Scheers, J.-H. Ahn, P. Johansson, A. Matic, P. Jacobsson, *J. Mater. Chem. A* **2013**, *1*, 2426.
12. Y. Yang, C. Wang, B. Yue, S. Gambhir, C. O. Too, G. G. Wallace, *Adv. Energy Mater.* **2012**, *2*, 266.
13. D.-W. Kim, S. R. Sivakkumar, D. R. MacFarlane, M. Forsyth, Y.-K. Sun, *J. Power Sources* **2008**, *180*, 591.
14. Z. Lei, Q. Yang, Y. Xu, S. Guo, W. Sun, H. Liu, L. P. Lv, Y. Zhang, Y. Wang, *Nat. Commun.* **2018**, *9*, 576.
15. Q. Yu, D. Chen, J. Liang, Y. Chu, Y. Wu, W. Zhang, Y. Li, L. Li, R. Zeng, *RSC Adv.* **2014**, *4*, 59498.
16. P. Gao, Z. Chen, Z. Zhao-Karger, J. E. Mueller, C. Jung, S. Klyatskaya, T. Diemant, O. Fuhr, T. Jacob, R. J. Behm, M. Ruben, M. Fichtner, *Angew. Chem. Int. Ed.* **2017**, *56*, 10341.
17. A. Antoniuk-Pablant, Y. Terazono, B. J. Brennan, B. D. Sherman, J. D. Megiatto, G. W. Brudvig, A. L. Moore, T. A. Moore, D. Gust, *J. Mater. Chem. A* **2016**, *4*, 2976.
18. M. K. Chahal, M. Sankar, *RSC Adv.* **2015**, *5*, 99028.
19. M. Zannotti, R. Giovannetti, C. A. D'Amato, E. Rommozzi, *Spectrosc. Acta Pt. A-Molec. Biomolec. Spectr.* **2016**, *153*, 22.
20. Q. Zhong, V. V. Diev, S. T. Roberts, P. D. Antunez, R. L. Brutchey, S. E. Bradforth, M. E. Thompson, *ACS Nano* **2013**, *7*, 3466.
21. J. K. Sprafke, S. D. Stranks, J. H. Warner, R. J. Nicholas, H. L. Anderson, *Angew. Chem. Int. Ed.* **2011**, *50*, 2313.

22. H. J. Choi, N. A. Kumar, J. B. Baek, *Nanoscale* **2015**, 7, 6991.
23. I. Hijazi, T. Bourgeteau, R. Cornut, A. Morozan, A. Filoramo, J. Leroy, V. Derycke, B. Jousset, S. Campidelli, *J. Am. Chem. Soc.* **2014**, 136, 6348.
24. P. K. Sonkar, K. Prakash, M. Yadav, V. Ganesan, M. Sankar, R. Gupta, D. K. Yadav, *J. Mater. Chem. A* **2017**, 5, 6263.
25. B. Delley, *J. Chem. Phys.* **1990**, 92, 508.
26. B. Delley, *J. Chem. Phys.* **2000**, 113, 7756.
27. J. P. Perdew, K. Burke, M. Ernzerhof, *Phys. Rev. Lett.* **1996**, 77, 3865.
28. A. Tkatchenko, M. Scheffler, *Phys. Rev. Lett.* **2009**, 102, 073005.
29. H. J. Monkhorst, J. D. Pack, *Phys. Rev. B* **1976**, 13, 5188.
30. R. S. Mulliken, *J. Chem. Phys.* **1955**, 23, 1833.
31. M. Aydinol, A. Kohan, G. Ceder, K. Cho, J. Joannopoulos, *Phys. Rev. B* **1997**, 56, 1354.
32. G. Granados-Oliveros, F. M. Ortega, E. Páez-Mozo, C. Ferronato, J.-M. Chovelon, *Open Mater.: Sci. J.* **2010**, 4, 15.
33. R. Giovannetti, in *Macro To Nano Spectroscopy*, InTech, London, United Kingdom **2012**.
34. X. Han, G. Qing, J. Sun, T. Sun, *Angew. Chem. Int. Ed.* **2012**, 51, 5147.
35. S. Renault, V. A. Oltean, C. M. Araujo, A. Grigoriev, K. Edström, D. Brandell, *Chem. Mater.* **2016**, 28, 1920.
36. P. Hu, H. Wang, Y. Yang, J. Yang, J. Lin, L. Guo, *Adv. Mater.* **2016**, 28, 3486.
37. J. Wu, X. Rui, G. Long, W. Chen, Q. Yan, Q. Zhang, *Angew. Chem. Int. Ed.* **2015**, 54, 7354.
38. J. Wu, X. Rui, C. Wang, W.-B. Pei, R. Lau, Q. Yan, Q. Zhang, *Adv. Energy Mater.* **2015**, 5, 1402189.
39. H. H. Lee, Y. Park, S. H. Kim, S.-H. Yeon, S. K. Kwak, K. T. Lee, S. Y. Hong, *Adv. Funct. Mater.* **2015**, 25, 4859.
40. H. H. Lee, Y. Park, K.-H. Shin, K. T. Lee, S. Y. Hong, *ACS Appl. Mater. Interfaces* **2014**, 6, 19118.
41. X. Han, F. Yi, T. Sun, J. Sun, *Electrochem. Commun.* **2012**, 25, 136.
42. S. W. Lee, B. M. Gallant, Y. Lee, N. Yoshida, D. Y. Kim, Y. Yamada, S. Noda, A. Yamada, Y. Shao-Horn, *Energy Environ. Sci.* **2012**, 5, 5437.
43. D. Aurbach, *J. Power Sources* **2000**, 89, 206.
44. J.-M. Kim, J. A. Kim, S.-H. Kim, I. S. Uhm, S. J. Kang, G. Kim, S.-Y. Lee, S.-H. Yeon, S.-Y. Lee, *Adv. Energy Mater.* **2017**, 7, 1701099.
45. J.-M. Kim, C.-H. Park, Q. Wu, S.-Y. Lee, *Adv. Energy Mater.* **2016**, 6, 1501594.
46. X. Zuo, J. Zhu, P. Müller-Buschbaum, Y.-J. Cheng, *Nano Energy* **2017**, 31, 113.
47. X. Su, Q. Wu, J. Li, X. Xiao, A. Lott, W. Lu, B. W. Sheldon, J. Wu, *Adv. Energy Mater.* **2014**, 4, 1300882.
48. L. Ji, Z. Lin, M. Alcoutlabi, X. Zhang, *Energy Environ. Sci.* **2011**, 4, 2682.

49. Y. Xu, Y. Zhu, F. Han, C. Luo, C. Wang, *Adv. Energy Mater.* **2015**, *5*, 1400753.
50. Y. Ma, R. Younesi, R. Pan, C. Liu, J. Zhu, B. Wei, K. Edström, *Adv. Funct. Mater.* **2016**, *26*, 6797.
51. J. G. Wang, D. Jin, R. Zhou, X. Li, X. R. Liu, C. Shen, K. Xie, B. Li, F. Kang, B. Wei, *ACS Nano* **2016**, *10*, 6227.
52. Y. Cheng, Z. Chen, M. Zhu, Y. Lu, *Adv. Energy Mater.* **2015**, *5*, 1401207.

\* Chapter 2.3 has collaborated with Dr. Kihun Jeong, Su Hwan Kim, Gwan Yeong Jung, and prof. Sang Kyu Kwak.

## List of publications

### (First-author)

1. **Ju-Myung Kim**<sup>†</sup>, Jeong A. Kim<sup>†</sup>, Seung-Hyeok Kim, In Sung Uhm, Sung Joong Kang, Guntae Kim, Sun-Young Lee, Sun-Hwa Yeon, and Sang-Young Lee<sup>\*</sup>,

“All-Nanomat Lithium-Ion Batteries: A New Cell Architecture Platform for Ultrahigh Energy Density and Mechanical Flexibility”

*Adv. Energy Mater.* 7, 1701099 (2017)

2. Ye-Ri Jang<sup>†</sup>, **Ju-Myung Kim**<sup>†</sup>, Jung-Han Lee, Sung-Ju Cho, Guntae Kim, Young-Wan Ju, Sun-Hwa Yeon,<sup>\*</sup> JongTae Yoo<sup>\*</sup> and Sang-Young Lee<sup>\*</sup>

“Molecularly designed, dual-doped mesoporous carbon/SWCNT nanoshields for lithium battery electrode materials”

*J. Mater. Chem. A* 4, 14996 (2016)

3. **Ju-Myung Kim**, Chang-Hoon Park, Qinglin Wu, Sang-Young Lee<sup>\*</sup>

“1D Building Blocks-Intermingled Heteronanomats as a Platform Architecture for High-Performance Ultrahigh-Capacity Lithium-Ion Battery Cathodes”

*Adv. Energy Mater.* 6, 1501594 (2016)

4. **Ju-Myung Kim**<sup>†</sup>, Chanhon Kim<sup>†</sup>, Seungmin Yoo, Jeong-Hoon Kim, Jung-Hwan Kim, Jun-Muk Lim, Soojin Park<sup>\*</sup>, and Sang-Young Lee<sup>\*</sup>

“Agarose-biofunctionalized, dual-electrospun heteronanofiber mats: Toward metal-ion chelating battery separator membranes”

*J. Mater. Chem. A* 3, 10687 (2015)

5. **Ju-Myung Kim**<sup>†</sup>, Han-Saem Park<sup>†</sup>, Jang-Hoon Park, Tae-Hee Kim, Hyun-Kon Song,<sup>\*</sup> and Sang-Young Lee<sup>\*</sup>

“Conducting Polymer-Skinned Electroactive Materials of Lithium-Ion Batteries: Ready for Monocomponent Electrodes without Additional Binders and Conductive Agents”

*ACS Appl. Mater. Interfaces.* 6, 12789 (2014)

6. **Ju-Myung Kim**, Jang-Hoon Park, Chang Kee Lee, Sang-Young Lee<sup>\*</sup>

“Multifunctional semi-interpenetrating polymer network-nanoencapsulated cathode materials for high-performance lithium-ion batteries”

*Sci. Rep.* 4, 4602 (2014)

### (Co-author)

1. Donggue Lee, Hyun-Woo Kim, **Ju-Myung Kim**, Ka-Hyun Lee and Sang-Young Lee\*  
 “Flexible/Rechargeable Zn-Air Batteries based on Multifunctional Heteronanomaterial Architecture”  
*ACS Applied Materials & Interfaces* 10, 22210 (2018)
2. JongTae Yoo, Young-Wan Ju, Ye-Ri Jang, Ohhun Gwon, Sodam Park, **Ju-Myung Kim**, Chang Kee Lee, Sun-Young Lee, Sun-Hwa Yeon\*, Guntae Kim\*, Sang-Young Lee\*  
 “One-pot surface engineering of battery electrode materials with metallic SWCNT-enriched, ivy-like conductive nanonets”  
*J. Mater. Chem. A* 5, 12103 (2017)
3. Jung Han Lee<sup>†</sup>, Jeong A Kim<sup>†</sup>, **Ju-Myung Kim**, Sun-Young Lee, Sun-Hwa Yeon\*, Sang-Young Lee\*  
 ”Beyond Slurry-Cast Supercapacitor Electrodes: PAN/MWNT Heteromaterial-Mediated Ultrahigh Capacitance Electrode Sheets”  
*Sci. Rep.* 7, 41708 (2017)
4. Jung Han Lee, **Ju-Myung Kim**, Jung-Hwan Kim, Ye-Ri Jang, Jeong A Kim, Sun-Hwa Yeon\*, Sang-Young Lee\*  
 “Toward Ultrahigh-Capacity V<sub>2</sub>O<sub>5</sub> Lithium-Ion Battery Cathodes via One-Pot Synthetic Route from Precursors to Electrode Sheets”  
*Adv. Mater. Interfaces* 3, 1600173 (2016)
5. Gaeun Hwang, **Ju-Myung Kim**, Dongki Hong, Choon-Ki Kim, Nam-Soon Choi, Sang-Young Lee\* and Soojin Park\*  
 “Multifunctional natural agarose as an alternative material for high-performance rechargeable lithium-ion batteries”  
*Green Chem.* 18, 2710 (2016)
6. Jeong-Hoon Kim, Jung-Hwan Kim, **Ju-Myung Kim**, Young-Gi Lee, Sang-Young Lee\*  
 “Superlattice Crystals-Mimic, Flexible/Functional Ceramic Membranes: Beyond Polymeric Battery Separators”  
*Adv. Energy Mater.* 5, 1500954 (2015)
7. Chanhon Kim, Sinho Choi, Seungmin Yoo, Dohyoung Kwon, Seunghee Ko, **Ju-Myung Kim**, Sang-Young Lee, Il-Doo Kim and Soojin Park\*  
 “A facile route for growth of CNTs on Si@hard carbon for conductive agent incorporating anodes for lithium-ion batteries”  
*Nanoscale* 7, 11286 (2015)
8. 15. Jang-Hoon Park, **Ju-Myung Kim**, Chang Kee Lee, Sang-Young Lee\*  
 “Mixed ion/electron-conductive protective soft nanomaterial-based conformal surface modification of lithium-ion battery cathode materials”  
*J. Power Sources* 263, 209 (2014)

9. Eun-Ho Lee, Ju-Hyun Cho, **Ju-Myung Kim**, Jang-Hoon Park, Sang-Young Lee\*  
“Facile surface modification of high-voltage lithium-ion battery cathode materials with electroconductive zinc antimonate colloidal nanoparticles”  
*RSC Adv.* 4, 15630 (2014)
10. Jang-Hoon Park, **Ju-Myung Kim**, Jong-Su Kim, Eun-Gi Shim, Sang-Young Lee\*  
“Polyimide/carbon black composite nanocoating layers as a facile surface modification strategy for high-voltage lithium ion cathode materials”  
*J. Mater. Chem. A* 1, 12441 (2013)
11. Eun-Ho Lee, Jang-Hoon Park, **Ju-Myung Kim**, Sang-Young Lee\*  
“Direct surface modification of high-voltage LiCoO<sub>2</sub> cathodes by UV-cured nanothickness poly(ethylene glycol diacrylate) gel polymer electrolytes”  
*Electrochimica Acta* 104, 249 (2013)
12. Jang-Hoon Park, Ju-Hyun Cho, Eun-Ho Lee, **Ju-Myung Kim**, Sang-Young Lee\*  
“Thickness-tunable polyimide nanoencapsulating layers and their influence on cell performance/thermal stability of high-voltage LiCoO<sub>2</sub> cathode materials for lithium-ion batteries”  
*J. Power Sources* 15, 442 (2013)